DOE/NASA/0005-1
NASA CR-174920

(NASA-CR-174920) WAKE EFFECTS ON THE AERODYNAMIC PERFORMANCE OF HORIZONTAL AXIS WIND TURBINES (Toledo Univ.) 176 p HC A09/MF A01 CSCL 10A G3/44 N85-29364 Unclas 21575

Wake Effects on the Aerodynamic Performance of Horizontal Axis Wind Turbines

Abdollah A. Afjeh
The University of Toledo

JUL 1985
RECEIVED
NASA STI FACILITY
ACCESS DEPT.

August 1984

Prepared for
NATIONAL AERONAUTICS AND SPACE ADMINISTRATION
Lewis Research Center
Under Grant NCC 3-5

for
U.S. DEPARTMENT OF ENERGY
Conservation and Renewable Energy
Wind Energy Technology Division

DOE/NASA/0005-1
NASA CR-174920

Wake Effects on the Aerodynamic Performance of Horizontal Axis Wind Turbines

Abdollah A. Afjeh
The University of Toledo
Toledo, Ohio

August 1984

Prepared for
NATIONAL AERONAUTICS AND SPACE ADMINISTRATION
Lewis Research Center
Cleveland, Ohio 44135
Under Grant NCC 3-5

for
U.S. DEPARTMENT OF ENERGY
Conservation and Renewable Energy
Wind Energy Technology Division
Washington, D.C. 20545
Under Interagency Agreement DE-AI01-76ET20320

TABLE OF CONTENTS

Page

NOMENCLATURE iii

CHAPTER I: INTRODUCTION 1

CHAPTER II: PREVIOUS INVESTIGATIONS

2.1 Momentum-Blade Element Theories 11

2.2 Vortex Theories 12

2.3 Vortex Wake Roll-Up. 17

CHAPTER III: RIGID WAKE ANALYSIS 19

3.1 General Description of Model 19

3.2 Coordinate System 20

3.3 Induced Velocity Calculations 20

3.4 Governing Equations 27

3.5 Numerical Procedure 30

3.6 Power, Torque and Drag on a Wind Turbine 32

CHAPTER IV: PRESCRIBED WAKE ANALYSIS 34

4.1 General Description of Model 34

4.2 Coordinate System 35

4.3 Induced Velocity 35

4.4 Numerical Procedure 44

PRECEDING PAGE BLANK NOT FILMED

Page

CHAPTER V: FREE WAKE ANALYSES 45

5.1 Fast Free Wake Analysis 46

5.1.1 Vortex Wake Model 46

5.1.2 Formulation of Problem 53

5.1.3 Computation Procedure 58

5.2 Simplified Free Wake Analysis 61

5.2.1 Description of Numerical Model 63

5.2.2 Coordinate System 65

5.2.3 Elementary Flow Field 69

5.2.4 Deformation of the Wake 72

5.2.5 Self-Induced Velocity 74

5.2.6 Numerical Procedure 78

5.2.7 Airfoil Characteristics 79

CHAPTER VI: RESULTS AND DISCUSSIONS 80

6.1 Airfoil Data 86

6.2 Circulation Distribution 93

6.3 Axial Induced Velocity Distribution 94

6.4 Effective Angle of Attack Distribution 95

6.5 Power and Thrust Coefficient Comparisons 96

6.6 Comparisons With Experimental Data 97

6.7 Results of the Prescribed Wake Analysis 98

6.8 Computed Wake Geometry 99

6.9 Computer Time 100

CHAPTER VII: CONCLUSIONS AND RECOMMENDATIONS 159

REFERENCES 164

NOMENCLATURE

a	parameter used in equation (4-19)
a_o	lift curve slope
A_m	Fourier sine series coefficients
b_o	lift coefficient for zero incident
c	blade chord
C_D	drag coefficient
C_L	lift coefficient
C_P	power coefficient
D	drag
D_1, D_2	parameters used in equations (3-18) and (3-19)
E	elliptic function of the second kind
F	axial force or drag on wind turbine
F_{tip}	tip loss factor
h	parameter defined as $h = r\tan\phi$
H_1, H_2	parameters defined by equations (4-12) and (4-13)
$\hat{i}$	unit vector along X axis
I	induction factor
$\hat{j}$	unit vector along Y axis
$\hat{k}$	unit vector along Z axis
k	parameter defined by equation (5-13)
K	elliptic function of the first kind
L	lift
$\vec{L}$	vector $\vec{L}$ defined by equation (3-8)
L_1, L_2, L_3	X, Y and Z coordinates of $\vec{L}$ in equation (5-6)
M	number of terms in truncated Fourier sine series

N	number of blades
N_1, N_2	parameters used in equation (3-18) and (3-19)
P	power
P_G	generated power, kW
P_R	rated power, kW
Q	torque
q_i	self-induced velocity
r, r'	distance along the blade
R	blade radius
s	length of vortex filament
s_1, s_2, s_3	X, Y and Z coordinates of vortex element used in equation (5-6)
t	time
u	radial induced velocity
U	velocity of airflows through rotor
V_o	wind velocity
V_2	downstream velocity
w	induced velocity
w_a	axial induced velocity
$\overline{w}_a$	axial induced velocity defined by $\frac{w_a}{V_o}$
w_n, w_{n1}	normal induced velocity
w_t	tangential induced velocity
w_x, w_{ix}	X-component of induced velocity
w_y, w_{iy}	Y-component of induced velocity
w_z, w_{iz}	Z-component of induced velocity
W	resultant velocity
W', W_u	undisturbed velocity defined by $W_u = (V_o^2 + \Omega^2 r^2)^{1/2}$

ρ	density
σ	blade solidity, $\sigma = \frac{Nc}{\pi R}$
ϕ, ϕ'	flow angle
ψ	azimuthal angle
Ω	rotational speed

Chapter I

INTRODUCTION

New interest has recently emerged in the wind as a clean and renewable source of energy. This interest has stimulated considerable research. Much of this work has been directed toward the development of large, horizontal axis, wind turbines (HWAT). Generally, such machines are capable of producing 100 kW or more at rated speed. Success of this research work is evidenced by the fact that several large horizontal axis wind turbine installations located around the world are producing relatively large amounts of power and many new installations are in the planning stage. Unlike nuclear power plants, wind turbines have readily been accepted by the general public. With the evaluation and acceptance of large horizontal axis wind turbines, a greater need now exists for accurate and efficient prediction of turbine performance.

Methods of performance prediction of wind turbines, have, over the years, been developed by modifying conventional propeller or helicopter theories. However, as DeVries has noted [1], in flight applications, determination of thrust or lift forces are more important than the determination of blade torque. On the other hand, for wind turbines, blade torque is of more fundamental importance than is the force in the wind direction. Furthermore, for a propeller in forward flight, the cruising speed is the primary factor in establishing the wake structure.

Hence, the disturbance or induced velocities, which are small compared to the forward velocity, have a negligible effect on wake geometry. This produces a periodic cylindrical wake which moves like a rigid body. Alternately, for a wind turbine, disturbance velocities are not, in general, small compared to wind speed over the operating range of the turbine. Consequently, the wake structure is not periodic, but is a nonlinear function of the induced velocities. The flow field of an airplane propeller experiences large disturbance velocities in the take-off condition and is somewhat similar to a wind turbine in its operating condition. However, no detailed calculation for this flight condition can be found in the literature.

Fluid mechanical description of a wind turbine and physical description of wind characteristics must be available if the study of HAWT's is to be performed in a rational and objective manner. Both of these needs can be met, at least partially, through use of simulated flow fields. There are two fundamental approaches to simulation: physical modeling and numerical modeling.

Physical modeling of a rotary wing in a wind tunnel has great flexibility for simulation of the flow field. Moreover, the controlled simulation of realistic operating conditions allows different parameters, such as the atmospheric boundary layer and turbulence, and their effects on the flow field to be isolated and investigated. Numerous examples of wind tunnel studies on airplane propellers and helicopter rotors can be found in the literature. The more recent experimental works on helicopter rotors include those of Gray, [2,3], and Landgrebe, [4]. It appears that Gray, [2], was the first to show that the wake of a hovering rotor is far from an ideal one of a rigid wake. His experimental work revealed that the wake of a hovering helicopter consisted of an intense rolled-up tip vortex and a diffused inboard wake. The wake flow was later extensively investigated by Landgrebe, [4]. This sort of experimental data, however, is not available for a wind turbine.

Numerical modeling of a rotary wing, on the other hand, has progressed to the stage where various formulations of the flow field, mostly employing inviscid and steady-state assumptions, can be investigated to determine their ability to predict the flow and the aerodynamic loads. Such models are either semi-empirical or analytical.

The analytical model for the unconstrained wake of a rotor is referred to as a free wake analysis. The works of Landgrebe, [4,5], and Gray, [6], were efforts toward developing such a model for a hovering helicopter. For wind turbines, the work of Gohard, [7], is particularly important. Unfortunately the computational costs of such a free wake analysis are appreciable. Furthermore, it was found that the computed wake configuration of hovering rotors, [8], does not correspond to the physically observed pattern. Hence, for hovering helicopters, the prescribed wake analysis, discussed in the following, has taken precedence over the free wake analysis.

The semi-empirical method includes two fundamental approaches: an analytical method combined with the use of airfoil data to correct for real fluid effects, and the method known as the "prescribed wake analysis". In the prescribed wake analysis, an experimentally determined wake geometry, such as those of Refs. [2,3,4], combined with the Biot-Savart law and blade element theory was used to develop a performance prediction analysis. This is a simple and accurate technique but is limited to rotors with geometries similar to that of the experimental unit. By eliminating the complicated problem of determining the wake geometry, the method allows other pertinent parameters of the problem to be investigated more thoroughly. However, detailed wind tunnel wake measurements of wind turbines are not abundant. Moreover, a qualitative study of the flow field of a full-scale wind turbine is given by Savino, [9]. The study included smoke flow visualization of the wake of a wind turbine at zero and low power generating conditions. In the experiment, four smoke grenades were used: two for tip and root vortices and two for the freestream flow. The grenades in the freestream were located on a cable upstream of the rotor. Photographs of the smoke traces were recorded with two movie cameras as well as a still camera. Two sketches of some observations are provided in Figure 1-1. The results of this study may be summarized as follows.

For a zero-generated-power condition, it was reported that at the start of the smoke release, the smoke streams were moving radially outward and not passing through the rotor directly. As the smoke streams travelled around the edge of the rotor disk, they had a tendency to curl

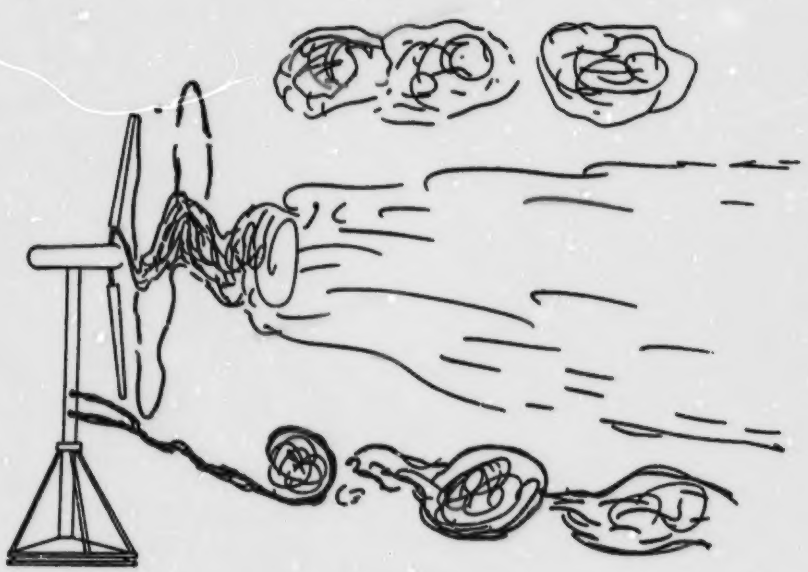

Fig. 1-1(a) Sketch of flow pattern of a full scale wind turbine at zero-generated-power, [9].

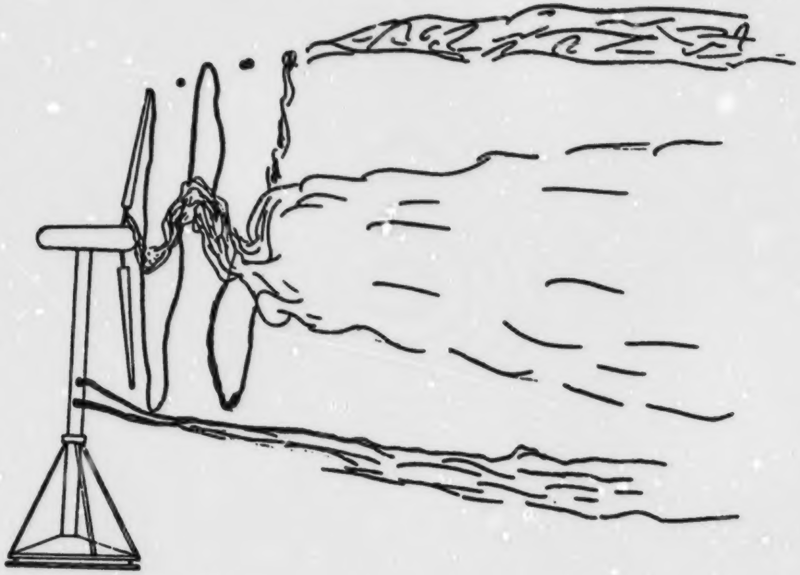

Fig. 1–1(b) Sketch of flow pattern of a full scale wind turbine at low–generated–power,[9].

in behind the rotor and mix into an outer stagnant region behind the rotor disk. It was also observed that the smoke streams diffused quickly in all directions and no significant tip vortices were noticed.

For low-power generating conditions, a significant expansion of the flow downstream of the rotor was reported. The root vortex was found to have transformed into a diffused expanding cylinder. And, the identity of tip and root vortices were almost dissipated after about one and a revolutions of the rotor.

Care should be exercised, however, in the interpretation of the movies and photographs taken for wake modeling purposes. The flow field of a full-scale wind turbine is dependent not only on the fluid-mechanical behavior of a turbine but also on the local wind characteristics. Rigorous analytical investigations of the flow field of a wind turbine, either by simple momentum theory or by simple vortex theory, reveals that the induced velocity far downstream is twice that at rotor disk. Consequently the wake must expand. On the other hand, if the free stream velocity, which is the primary factor in establishing the mass flow rate into the wake, is high, expansion effects are negligible. This velocity also transports the tip vortex away from the disk plane so that it is relatively far removed from the tip vortex of the following blade. Thus, interference effects are minimized.

The analysis of the local wind characteristics is much more complex. Atmospheric motion is basically derived by unequal heating of the earth's surface by solar radiation, the rotation of the earth, and the nonuniform surface temperature and roughness. Nonlinear interaction between the fluid systems of different scales and with the forces resulting from the variety of causes produce wind characteristics which vary in an almost random manner. Usually the motion is turbulent, gusty and swirling, with rapid changes in speed and direction. Furthermore, weak-wind characteristics are much different than those of a strong wind. In a weak-wind condition, which is the case in Ref. [9], thermal stratification over the atmospheric boundary layer strongly affects the turbulent mixing and must be taken into account, [10]. With strong winds, of course, the intense turbulence destroys the temperature layers in the atmosphere.

Existing computer codes for wind turbine performance prediction are either based on the blade element-momentum theory or the vortex theory. The deficiencies of the codes employing the blade element-momentum theory lies in the inherent assumptions of an infinite number of blades and unidirectional flow (no reversed flow). Thus, performance is not accurately predicted at low wind speeds or for wind turbines having a small number of blades. The computer codes utilizing the free vortex theory are less restricted; however, the required computational times are excessive. To remedy this problem, a rigid wake is usually assumed to replace the actual wake. Such wake models are, therefore, limited to relatively low tip speed ratio conditions where expansion effects are negligible.

In light of the preceding discussion, it is seen that a method capable of treating a wind turbine's wake deformation and expansion is desirable. The fluid mechanics of a wind turbine with wind effects included in the analysis, however, greatly exceeds the complexity of classical methods of analysis of a rotary wing. Interactability of most ingredients of the wind and rotor flow causes the investigation of the problem to be much more complicated. Furthermore, because of insufficient knowledge of the structure of the turbulent boundary layer, accurate mathematical modeling of the fluid phenomena, at least for the present time, cannot be accomplished. For these reasons, in the current analysis, the wind effects are restricted to mass and momentum transport, primarily in the direction parallel to the turbine axis, and the turbulence and boundary layer effects are neglected. In addition, to the best knowledge of the author the experimental data for the wake of wind turbines are scarce. Hence, in the present work, for the prescribed wake analysis, an arbitrarily defined wake geometry will be employed.

The primary objective of this research is to develop a new numerical method that can predict wind turbine blade velocities and the circulation distribution without relying on a rigid wake assumption and to accomplish this without utilizing the great amounts of computer time which are generally required in free wake analyses. Thus, this method is to be developed with very few assumptions and with reasonable empiricism while maintaining a computationally viable procedure. The method is to account for wake expansion and deformation while the deformed wake geometry is not prescribed. In developing this model use will be made of the helicopter wake observations of the investigators already mentioned. Other objectives may be listed as follows:

1) To develop a convenient analytical method for performance prediction. This method makes use of a helicopter wake model proposed by Miller, [11, 12].
2) To develop a computer code for performance prediction using a prescribed wake method. The shape of the wake is either a part of the computer program input data or follows from the calculations.
3) To check the accuracy of the method by comparing computed results with those of the MIT full free wake method, [7], and the available experimental data whenever possible.

An overview of previous research on blade performance prediction is presented in chapter 2. A review of rigid vortex wake analysis of wind turbines is given in chapter 3, and chapter 4 contains a brief study of the prescribed wake analysis. In chapter 5 formulation of a "fast" free wake model is presented. The details of the simplified free wake method along with the numerical solution of the problem is also included in chapter 5. Finally, the results of the application of the methods of analysis are presented in chapter 6.

Chapter II

PREVIOUS INVESTIGATIONS

2.1 Momentum-Blade Element Theories

Past research dealing with performance and load prediction of propellers and rotors indicates that the predicted performance is only as accurate as the inflow calculations at the rotor disc. It appears that the Rankine-Froude momentum theory, [13,14], was the first attempt to predict inflow velocities at the rotor. The theory assumes that the rotor can be replaced by an actuator disc. The actuator disc is uniformally loaded and therefore develops a uniform axial induced velocity. The theory gives average performance values and does not provide detailed information on the blade loading and induced velocity distribution. Considerable improvement in performance prediction is obtained with a combined momentum-blade element theory, [15]. This theory has its roots in Prandtl's hypothesis which states that a section of a finite length wing behaves just as though it were a section of an infinite length wing set at an angle equal to the effective angle of attack. The momentum-blade element theory attempts to remove the uniform inflow assumption of Rankine-Froude theory by balancing the blade thrust against wake momentum in radial annuli. However, the inherent assumption that the rotor has an infinite number of blades makes the results of this theory and similar analyses, in general, suspect. Wilson and Walker, [16], developed a numerical method employing the combined momentum-blade element theory for horizontal-axis wind turbines. A number of fictitious correction factors, called tip-loss factors, have been used in this model to account for the different flow regimes experienced by a rotor with a finite number of blades. Nevertheless, the estimated power coefficient has at times been found to exceed Betz's theoretical limit as indicated by Wentz, [17]. It should be mentioned that this excessive power coefficient occurs at high tip-speed ratios where wake distortion is significant. More accurate methods of analysis are those of vortex wake models. The use of complex wake analyses, however, has been made possible with the advent of high-speed computational equipment.

2.2 Vortex Theories

A vortex is defined as a region containing a concentrated amount of vorticity. A line in the fluid whose tangent is everywhere parallel to the local vorticity vector is called a vortex line. A vortex tube is a surface formed by all vortex lines contained in a given closed curve. A vortex tube has a strength equal to the circulation around the vortex area. If a vortex tube of a given strength is allowed to shrink to a vortex tube of infinitesimal cross-section but with the same strength, a mathematical idealization of a vortex tube results which is termed a filament of vorticity or a vortex filament. A surface concentration of vorticity is called a vortex surface. This surface may be thought of as a collection of a number of strips each enclosed by a vortex tube.

The Helmholtz theorem of vortex continuity, [18], states that an irrotational motion of an inviscid fluid started from rest remains irrotational. Evidently, a vortex filament cannot end abruptly and must extend either to infinity or to a solid boundary. This implies that vorticity can only be produced at boundaries. The distribution of vorticity, once generated, throughout the interior of fluid can be determined from the equation of motion for vorticity or the "vorticity equation", [19]. A mechanism for generation of vorticity exists at solid boundaries. Hence solid surfaces may be regarded as sources of vorticity. This leads to the classical treatment of replacing solid surfaces in contact with a fluid by a distribution of vorticity.

The prediction of wind turbine aerodynamic performance requires determination of the inflow velocities at the blades. This inflow velocity is determined by the free stream speed, the blade bound vortex induced velocities and the wake induced velocities. Of these, however, the wake induced flow can be obtained only if the vortex wake geometry is known.

Classical vortex methods used to predict performance are mainly the well-known theories of Glauert, Prandtl and Goldstein, [20,21,22]. Glauert vortex theory assumes the wake to be a semi-infinite cylindrical sheet of vorticity shed from the edge of an actuator disk. This theory, like the combined momentum-blade element theory, implies that the rotor has an infinite number of blades and is uniformly loaded. Prandtl's vortex theory shapes the radial inflow distribution by assuming the flow in the ultimate wake to be very nearly like the flow exterior to an infinite number of semi-infinite strips. The results are expressed in terms of a tip-loss factor dependent on the number of blades, the radial position and the wake helix angle at the tip. The vortex theory of Goldstein defines the inflow by assuming the ultimate wake to include a set of semi-infinite, equidistant, co-axial, helicoidal surfaces of constant pitch representing the vortex sheet shed from the trailing edge of each blade. This wake model, however, represents the case of a lightly loaded optimum design rotor, [23]. Goldstein's results are expressed in a semi-infinite series of modified Bessel functions and cannot be easily handled for the general case without the aid of a high-speed computer. Prandtl's theory is easier to use since it is expressible in a closed form and has been employed successfully in the design of propellers (see for example, [24]).

Since the entire blade is seldom in an optimum design condition, Lock, [25], developed a scheme to analyze non-optimum rotors by applying Goldstein's theory at each spanwise section. In spite of the limitation of an unrealistic constant diameter wake, the Goldstein-Lock model represented more or less the standard classic analysis of rotors until recently.

A correlation of conventional methods for hovering rotor performance prediction shows a tendency to underpredict power, [26]. It is also shown that empirical correction factors which correlate experimental results with theory, developed for one configuration, cannot be confidently generalized to other designs.

Attempts at predicting rotor inflow have followed two particular paths: semi-empirical and analytical. The complex flow field of the steady state propeller has been visually observed and reported in [2,3,4,27]. This has led to an experimental determination of wake positions as a function of rotor design parameters. Gray, [2,3], showed that the wake behind a rotor is composed of a strong tip vortex and a weak, diffused inboard wake. The observed geometry is a contracting helix that approaches a constant diameter and a constant pitch as it moves downstream of the rotor. Landgrebe [4], developed a prescribed wake analysis that uses the observed wake geometry. The entire wake consists of a number of filaments shed at the trailing edge of the blade. A certain number of outer filaments are immediately rolled-up into a tip vortex. The strength of the filaments and the tip vortex are not known at the outset but are calculated in an implicit procedure by relating the filament strength and the induced velocity to the discretized blade circulation distribution. The procedure also yields the blade loading which is integrated in order to compute total thrust. Such an aerodynamic analysis of a rotor using an experimentally determined wake geometry represents the present state-of-the-art. In addition, Landgrebe performed a considerable number of flow visualization experiments in order to obtain a range of tip vortex and sheet geometry data.

Analytical approaches to inflow prediction for propellers, in general, utilize lifting line theory and some iterative technique to determine a realistic wake. The first of these methods was that of Crimi, [28], who replaced the wake by a single tip vortex. The circulation was prescribed, but as the blade moved, the tip vortex was allowed to move under the induced velocity field. Several other simplified methods have been used to model the wake geometry such as those in which the wake is approximated by vortex rings or vortex tubes (e.g., [29] and [30]). Additionally, Theodorson, [31], extended his early propeller theory to include wake contraction in the calculation of performance with optimum loading.

Of the more recent methods characterized by the representation of the wake from each blade by segmented vortex filaments, which are allowed to distort freely, the work of Landgrebe, [4], should be mentioned. Here, the blade is represented by a single bound vortex. The trailing vortex filaments represent the wake. The wake vortex filaments are allowed to move under the influence of the induced flow field. However, the effect of local-induced or self-induced singular part is neglected. Lastly, the work of Sadler, [32], is cited. Rather than starting the interaction with an assumed wake geometry and an assumed circulation distribution and then iterating to a consistent wake geometry-circulation model, Sadler developed a model which permitted the rotor to start from rest, impulsively. As the blade begins to rotate, an array of distorted, discrete trailing and shed vortices is generated. The wake is then allowed to move under its own induced velocity field as time progresses. The wake geometry and the circulation distribution are thus compatible at each instant of time. Calculations are repeated until the steady state solution is obtained. For wind turbines, the pioneering work of Gohard [7] is noted. In this investigation, calculations were initiated from an assumed wake geometry based on momentum theory. The vortex segments were then allowed to distort freely until they converged to a final geometry. The motion of the wake elements was computed using the Biot-Savart law. The computer time for such calculations was found to be large. The vortex geometry at the end of such a procedure, however, does not agree with the experimentally observed geometry, [8].

2.3 Vortex Wake Roll-Up

The vortex wake roll-up problem was studied initially for wings of finite length. The wake system behind a lifting wing in steady flow is composed of two regions: an intermediate field where the rolling-up process principally occurs and a far field where roll-up is essentially complete. In this latter region the details of the roll-up are not required, and two models are presently available, [33 and 34]. Both models assume axisymmetric two-dimensional flow in the far wake. The Spreiter and Sacks' model has been applied by many investigators but only recently the Betz vortex model has been recognized as the more accurate model for this problem, [35,36].

For the intermediate region, the rolling-up process was studied analytically by Kaden, [37]. Later, a numerical calculation was performed by Westwater, [38], and by Rosenhead, [39]. These research studies considered the roll-up in steady flow to be two-dimensional in the cross flow plane. The wake was modeled by discrete point vortices. Takami, [40], showed, however, that modeling with discrete point vortices could not be used to obtain a quantitative picture of the rolling-up process. The calculations were found to deteriorate with time. The model, on the other hand, provides a qualitative picture of vortex roll-up and a concentration of vortices toward the rolled-up center is clearly shown. Further, Jordan, [41], notes the failure of standard analyses to predict the correct roll-up rate; typically these rates are much slower than the experimentally observed rates. As a consequence he has presented an analysis which contains a logarithmic singularity just inside the tip at the trailing edge and has claimed this singularity will drive the roll-up at a much faster rate. Unfortunately, no hypothesis as to what this logarithmic singularity might correspond to physically is presented.

In summary, it must be concluded that relatively little is presently known about the mechanism of vortex wake roll-up. A rather complete bibliography of wake roll-up considerations can be found in the survey report by El-Ramly, [42].

Chapter III

RIGID WAKE ANALYSIS

This chapter contains a brief study of the rigid wake analysis for horizontal axis wind turbines. The wake model is based on Moriya's theory [43] originally developed for propellers. A detailed analysis of this theory can be found in Ref. [44].

3.1 General Description of Model

The rigid wake model assumes that the wake behind a horizontal axis wind turbine consists of helical sheets of vorticity of constant pitch and diameter, trailing from the blades and extending to infinity. It is further assumed that the wake moves downstream of the rotor plane with a constant velocity of the free stream. This implies that the effects of disturbance velocity on wake convection are neglected. Basic assumptions used in formulation of this theory are as follows:

1. that the fluid is inviscid and incompressible;
2. that section characteristics can be calculated according to Prandtl's hypothesis; and
3. that the hub has no effect on rotor flow.

3.2 Coordinate System

A blade-fixed cylindrical coordinate system as well as a blade-fixed Cartesian coordinate system are used in formulation of the problem. The Cartesian coordinate axes X and Y form a plane of rotation and the Z axis is directed along the axis of rotation. In the cylindrical coordinate system the r-axis is coincident with the blade span, the θ-axis measures the azimuthal angle from the blade and the Z-axis is again the axis of rotation. Both coordinate systems are shown in Fig. 3-1.

3.3 Induced Velocity Calculation

The disturbance velocity at the rotor plane is that due to a helical vortex sheet trailing from the blade and extending infinitely far downstream. This velocity field can be calculated from the Biot-Sarvart Law [45] as

$$d\vec{w}_i = \frac{d\Gamma}{4\pi} \frac{(\vec{s}-\vec{r}') \times d\vec{\eta}}{(\vec{s}-\vec{r}')^3} \tag{3-1}$$

where $d\vec{w}_i$ is the differential velocity induced at a point r on the blade due to a vortex filament, $d\vec{\eta}$, which had originated at a point r on the blade. The differential change in circulation between spanwise locations r and r + dr is $d\Gamma$. This differential circulation is, of course, equal to the strength of the vortex trailing from the element of blade dr. Position vectors $\vec{s}$ and $\vec{r}$ are shown in Fig. 3-1. From this figure one readily obtains

$$\vec{r}' = r'\,\hat{i} \tag{3-2}$$

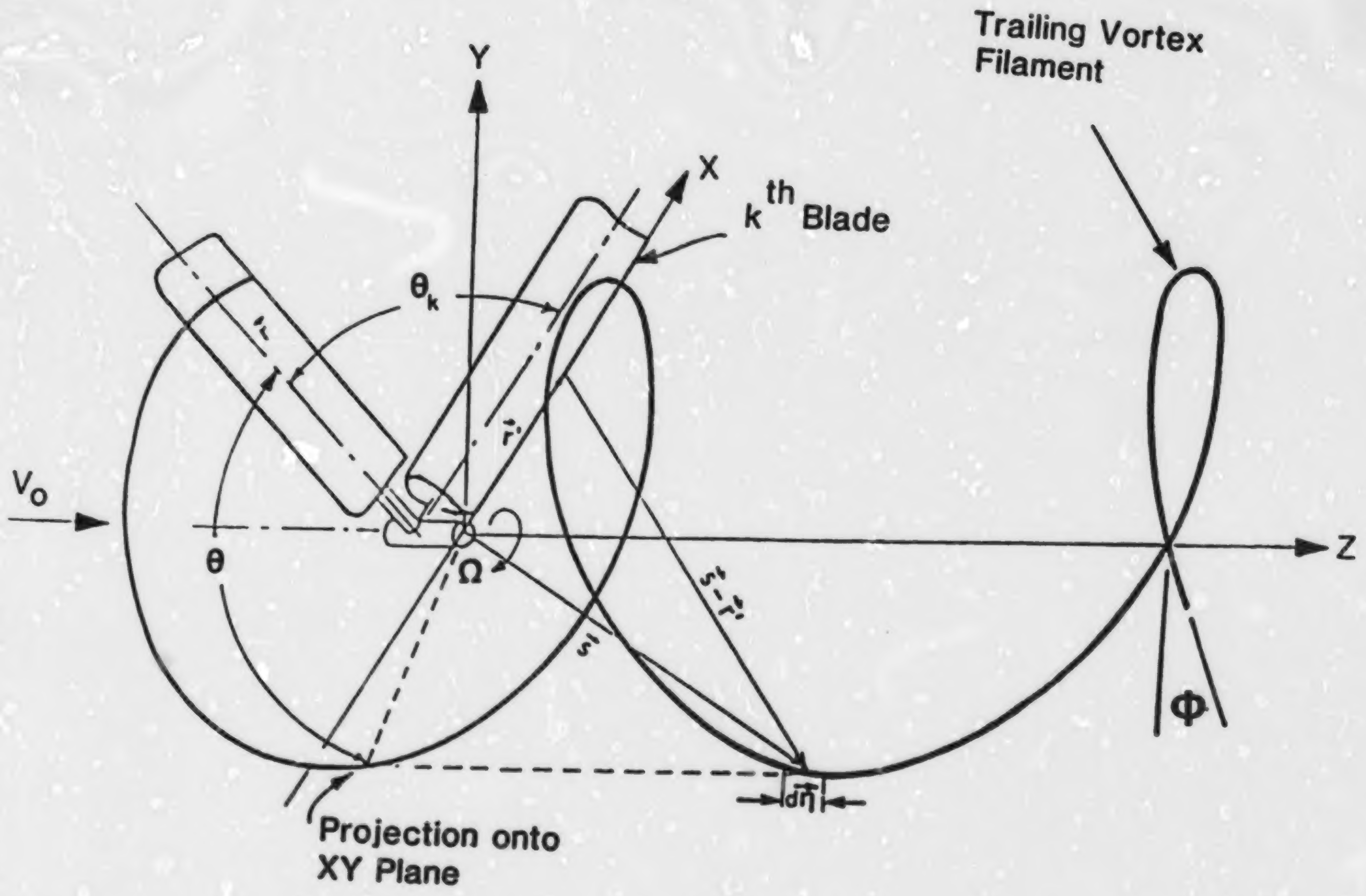
Trailing Vortex
Filament
Y
X
k^{th} Blade
θ_k
$\vec{r}$
$\vec{r}'$
V_o
θ
Ω
Z
$\vec{s}-\vec{r}'$
$\vec{s}$
Φ
$d\vec{\eta}$
Projection onto
XY Plane

Fig. 3-1 Vortex geometry and coordinate system

$$\vec{s} = r\cos(\bar{\theta}_k)\hat{i} + r\sin\bar{\theta}_k\hat{j} + r\theta\tan\phi\;\hat{k} \tag{3-3}$$

$$d\vec{\eta} = r\,d\theta\{-\sin\bar{\theta}_k\hat{i} + \cos\bar{\theta}_k\vec{j} + \tan\phi\;\hat{k}\} \tag{3-4}$$

In these equations θ is the azimuthal angular variable of the helix and ϕ is the pitch of the helix. Substituting $\vec{s}$, $\vec{r}'$ and $d\vec{\eta}$ from these equations into equation (3-1) will result in, after some manipulations (see Ref.44 for details),

$$dw_x = \frac{\frac{d\Gamma}{dr}dr}{4\pi L^3}\;hr[\sin\bar{\theta}_k - \bar{\theta}\cos\theta_k]d\theta \tag{3-5}$$

$$dw_y = \frac{\frac{d\Gamma}{dr}dr}{4\pi L^3}\;h[r' - r\cos\bar{\theta}_k - r\theta\sin\bar{\theta}_k]d\theta \tag{3-6}$$

$$dw_z = \frac{\frac{d\Gamma}{dr}dr}{4\pi L^3}\;[r^2 - rr'\cos\bar{\theta}_k]d\theta \tag{3-7}$$

where

$$L = [r^2 + r'^2 - 2rr'\cos\bar{\theta}_k + h^2\theta^2]^{1/2} \tag{3-8}$$

$$\theta_k = \frac{2\pi(N-k)}{N} \text{ and } \bar{\theta}_k = \theta + \theta_k \tag{3-9}$$

The components of induced velocity at r' due to a single helical vortex filament shed from a section located at r along the span can be obtained by integrating equations (3-5), (3-6) and (3-7) with respect to θ from 0 to infinity. This yields

$$dw_x = \frac{\frac{d\Gamma}{dr}dr}{4\pi} \sum_{k=1}^{N} \int_0^\infty \frac{hr[\sin\theta k - \theta\cos\theta_k]}{L^3}\, d\theta \qquad (3\text{-}10)$$

$$dw_y = \frac{\frac{d\Gamma}{dr}dr}{4\pi} \sum_{k=1}^{N} \int_0^\infty \frac{h[r' - r\cos\theta_k - r\theta\sin\theta_k]}{L^3}\, d\theta \qquad (3\text{-}11)$$

$$dw_z = \frac{\frac{d\Gamma}{dr}dr}{4\pi} \sum_{k=1}^{N} \int_0^\infty \frac{r^2 - rr'\cos\theta_k}{L^3}\, d\theta \qquad (3\text{-}12)$$

For a constant diameter helical vortex wake, however, $dw_x = 0$ [43]. The components of induced velocity in directions normal and parallel to the undistrubed velocity, W', of the blade element are obtained, from Fig. 3-2, as

$$dw_n = dw_z\cos\phi' - dw_y\sin\phi' \qquad (3\text{-}13)$$

$$dw_t = dw_z\sin\phi' + dw_y\cos\phi' \qquad (3\text{-}14)$$

where

$$\cos\phi' = \frac{\mu'}{(\mu'^2 + 1)^{1/2}} \qquad (3\text{-}15)$$

$$\sin\phi' = \frac{1}{(\mu'^2 + 1)^{1/2}} \qquad (3\text{-}16)$$

and

$$\mu' = \frac{r'\Omega}{V_0} \qquad (3\text{-}17)$$

ORIGINAL PAGE IS
OF POOR QUALITY

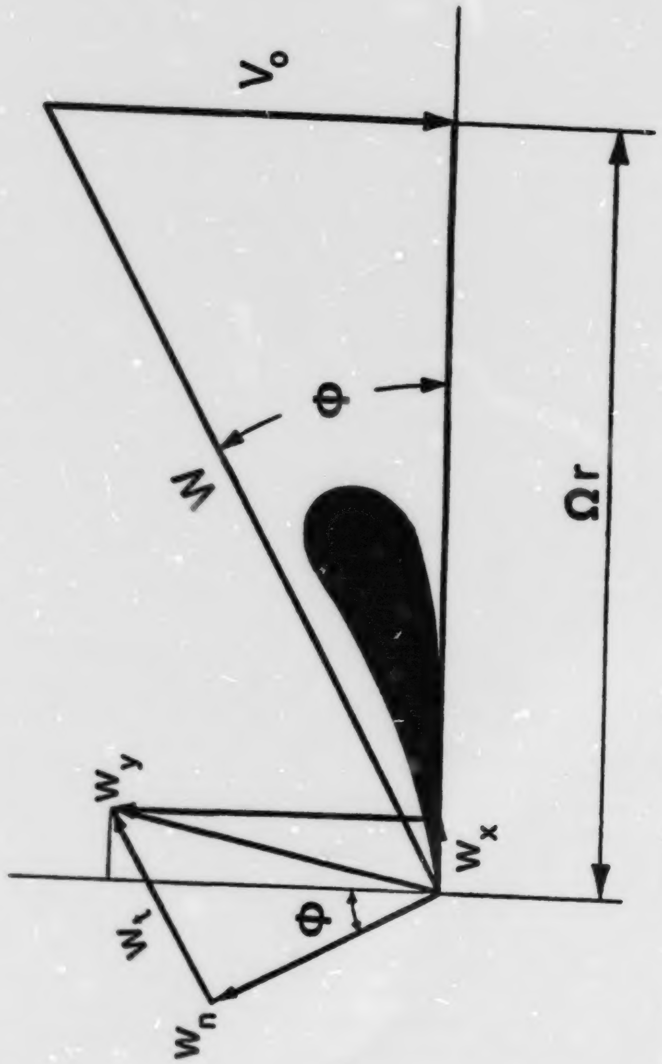
V_o
W
Φ
Ωr
W_y
W_x
W_t
W_n
Φ

Fig. 3-2 Velocity diagram showing induced velocity and its components

Using these expressions and employing non-dimensional distance parameters, ξ and ξ', the elements of induced velocity components, normal and tangential, are obtained as

$$dw_n = \frac{\frac{d\Gamma}{d\xi}d\xi}{4\pi R} \sum_{k=1}^{N} \int_0^{\infty} \frac{N_1\xi' + N_2\lambda_o}{D_1^{3/2}\, D_2^{1/2}}\, d\theta \tag{3-18}$$

$$dw_t = \frac{\frac{d\Gamma}{d\xi}d\xi}{4\pi R} \sum_{k=1}^{N} \int_0^{\infty} \frac{N_1\lambda_o - N_2\xi'}{D_1^{3/2}\, D_2^{1/2}} \tag{3-19}$$

where

$$\xi = \frac{r}{R} \tag{3-20}$$

$$\xi' = \frac{r'}{R} \tag{3-21}$$

and

$$N_1 = [\xi'^2 - \xi\xi'\cos\bar{\theta}_k]$$

$$N_2 = [\xi(\theta\sin\bar{\theta}_k + \cos\bar{\theta}_k) - \xi']\frac{h}{R}$$

$$D_1 = [\xi^2 + \xi'^2 - 2\xi\xi'\cos\bar{\theta}_k + \frac{h^2}{R^2}\theta^2$$

$$D_2 = \lambda_o^2 + \xi'^2$$

$$h = \frac{V_o - w_n\cos\phi'}{\Omega + \frac{w_n\sin\phi'}{r}}$$

The total component of normal induced velocity can be obtained by integrating equation (3-18) from the non-dimensional hub radius, ξ_{hub}, to the non-dimensional tip radius, $\xi = 1$. Thus,

$$w_n(\xi') = \int_{\xi_{hub}}^{1} \frac{\frac{d\Gamma}{d\xi}d\xi}{4\pi R} \sum_{k=1}^{N} \int_{o}^{\infty} \frac{N_1\xi' + N_2\lambda o}{D_1^{3/2}\,D_2^{1/2}}\,d\theta \qquad (3\text{-}22)$$

It can be seen that the integral in equation (3-22) becomes infinitely large at the point $r = r'$ when $\theta = \theta_k = 0$. This presents a problem since accurate determination of the integral in the neighborhood of this singularity is desired. This problem may be resolved by applying Moriya's theory [37]. According to this approach, an induction factor is defined as

$$I = \frac{dw_n}{dw_{n1}} \qquad (3\text{-}23)$$

where dw_n and dw_{n1} are velocities induced by helical and straight vortex filaments, respectively. This factor is considered to be a continuous function. Introducing this factor in the analysis will result in

$$w_n(\xi') = \int_{\xi_{hub}}^{1} \frac{\frac{d\Gamma}{d\xi}}{4\pi R}\,\frac{I}{\xi - \xi'}\,d\xi \qquad (3\text{-}24)$$

The disturbance velocity can be computed from this equation if the circulation distribution is known. This will be accomplished using a Fourier sine series representation as discussed in the following section.

3.4 Governing Equations

The local velocity at a blade section is obtained by the superposition of the free stream velocity, V_0, the velocity due to rotation, r_Ω, and the distrubance velocity, w_n. Reference to Fig. 3-3 reveals that the blade setting relative to the resultant velocity W, α_e, is equal to its setting relative to the undisturbed velocity, W', diminished by the induced angle, α_i. Thus this equation may be written as

$$\alpha_g = \alpha_e - \alpha_i \tag{3-25}$$

The minus sign in the above equation accounts for the fact that the induced angle of attack is itself a negative number. Moreover, the induced angle of attack can be obtained from Fig. 3-3 as

$$\alpha_i = \tan^{-1} \frac{w_n}{W'} \tag{3-26}$$

$$= \frac{w_n}{W'} - \frac{(w_n/W')^3}{3} +$$

$$\cong \frac{w_n}{R\Omega(\lambda_0{}^2+\xi'^2)^{1/2}} \tag{3-27}$$

The approximation is known as the small angle assumption. The magnitude of undisturbed velocity is obtained from Fig. 3-3. The section is positioned at an angle, termed the geometric angle of attack, relative to the resultant velocity W given by

$$\alpha_g = \tan^{-1} (\frac{\lambda_0}{\xi'}) - \beta \tag{3-28}$$

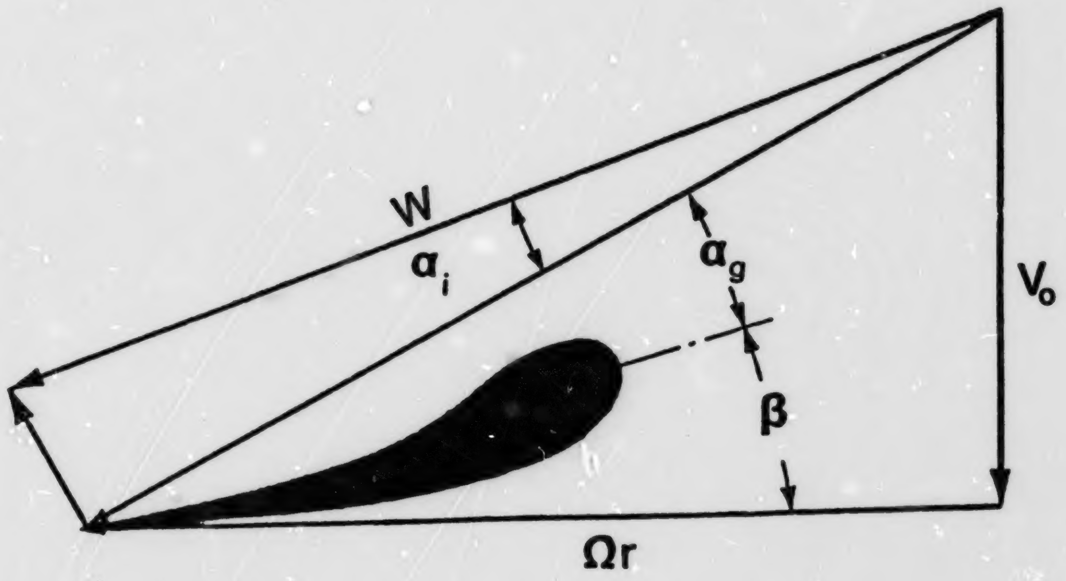
W
α_i
α_g
V_o
β
Ωr

Fig. 3-3 Velocity diagram showing the effect of induced velocity.

Substituting w_n from equation (3-24) into equation (3-26) yields

$$\alpha_i = \int_{\xi_{hub}}^{1} \frac{\frac{d\Gamma}{d\xi}}{4\pi R^2 \Omega (\lambda_o{}^2 + \xi'^2)^{1/2}} \; \frac{I}{\xi - \xi'} \, d\xi \qquad (3\text{-}29)$$

The circulation distribution must satisfy the following boundary conditions

$$\Gamma(\xi_{hub}) = \Gamma(1) = 0 \qquad (3\text{-}30)$$

These conditions can be satisfied by using a suitably written Fourier sine series:

$$\Gamma(\xi) = \sum_{m=1}^{\infty} A_m \sin \; (mn) \left(\frac{\xi - \xi_{hub}}{1 - \xi_{hub}}\right) \qquad (3\text{-}31)$$

However, for practical purposes the series is truncated at M terms. Now by making use of the truncated Fourier series representation of the circulation distribution, equation (3-29) can be rewritten as

$$\alpha_i = \frac{\sum_{m=1}^{M} mA_m \; {}_{\xi_{hub}} \; \cos \; (m\pi)\left(\frac{\xi - \xi_{hub}}{1 - \xi_{hub}}\right) \frac{I}{\xi - \xi'} \, d\xi}{4R^2 \Omega (\lambda_o{}^2 + \xi'^2)^{1/2} \; (1 - \xi_{hub})} \qquad (3\text{-}32)$$

The relation between circulation and lift coefficient at each section is given by the Kutta-Joukowski theorem [18] as

$$\rho W \Gamma = C_L (1/2 \; \rho W^2) c$$

or $\qquad\qquad$ (3-33)

$$\Gamma = 1/2 \; cWC_L$$

where c is the chord of the blade section.

The section lift coefficient can be obtained from two-dimensional wind tunnel data, i.e.,

$$C_L = C_L(\alpha_e) \tag{3-34}$$

Combining equations (3-33) and (3-34) yields

$$C_L(\alpha_e) = \frac{2}{cW'} \sum_{m=1}^{M} A_m \sin (m\pi) \frac{\xi'-\xi_{hub}}{1-\xi_{hub}} \tag{3-35}$$

This equation provides a means of relating α_e and the unknown circulation coefficients A_m. Thus, by substituting this equation into equation (3-25) for α_e, and making use of equation (3-32) for α_i, a single expression is obtained which may be solved for the unknown coefficients A_m. In general, the solution must be obtained numerically since it is not always possible to write an explicit equation for the section lift coefficient. The method to determine the unknown coefficients A_m will be explained in the next section.

3.5 Numerical Procedure

The numerical procedure for computing the inflow distribution and loading on the blades is presented in this section. In general the method utilizes an iterative technique to determine blade section characteristics using realistic two dimensional airfoil data. To start the iteration process, a first approximation of section lift coefficient may be made by assuming a linear relation between this coefficient and the section effective angle of attack i.e.,

$$C_L = a_0\alpha_e + b_0 \tag{3-26}$$

Combining equations (3-25), (3-28), (3-32) and (3-33) results in the following equation

$$2\sum_{m=1}^{M} A_m \, \mathrm{Sin}(m\pi)\left(\frac{\xi'-\xi_{hub}}{1-\xi_{hub}}\right) -$$

$$\frac{1}{4R^2\Omega(\lambda_o{}^2+\xi'^2)^{1/2}\,(1-\xi_{hub})}\sum_{m=1}^{M} mA_m \int_{\xi_{hub}}^{1} \cos(m\pi)\left(\frac{\xi'-\xi_{hub}}{1-\xi_{hub}}\right)\frac{I}{1-\xi_{hub}}\,d\xi =$$

$$\tan^{-1}\left(\frac{\lambda_o}{\xi'}\right) - \beta + \frac{b_o}{a_o} \qquad (3\text{-}27)$$

This equation is applied at M locations along the blade. Thus, a system of M linear equations is obtained which can be solved for the coefficients A_m. Having determined the A_m, the section effective angle of attack and the section induced angle of attack are obtained by application of equations (3-36) and (3-32), respectively.

The iteration process for the case of two-dimensional airfoil data is as follows:

1) Use α_e for each spanwise location to obtain C_L;
2) Calculate the local circulation distribution;
3) Set up a linear system of equations utilizing the truncated Fourier series and values of circulation at M spanwise locations, then solve for A_m;

4) Compute the local induced angle of attack;
5) Calculate the new local effective angle of attack;
6) Obtain C_L from two-dimensional airfoil data using the value of α_e calculated in the preceding step; and
7) Compare the most recently calculated C_L to the previous value of C_L, if they are equal, stop; otherwise go to step 2.

3.6 Power, Torque and Drag on a Wind Turbine

Once the iteration is converged and the angle of attack distribution along the blade span is determined, rotor forces and torque and power can be calculated by applying the following equations:

$$\frac{dF}{dr} = \frac{1}{2}\rho N c W^2 (C_L \cos_\phi + C_D \sin_\phi) \tag{3-38}$$

$$\frac{dQ}{dr} = \frac{1}{2}\rho N c W^2 (C_L \sin\phi - C_D \cos\phi) r \tag{3-39}$$

$$\frac{dP}{dr} = \frac{1}{2}\rho c W^2 (C_L \sin\phi - C_D \cos\phi) r\Omega \tag{3-40}$$

The above equations are easily obtained from the geometry of Fig. 3-4 and the definition of lift and drag coefficients, i.e.,

$$C_L = \frac{dL}{\frac{1}{2}\rho W^2 c\,dr}$$

$$C_D = \frac{dD}{\frac{1}{2}\rho W^2 c\,dr}$$

ORIGINAL PAGE IS
OF POOR QUALITY

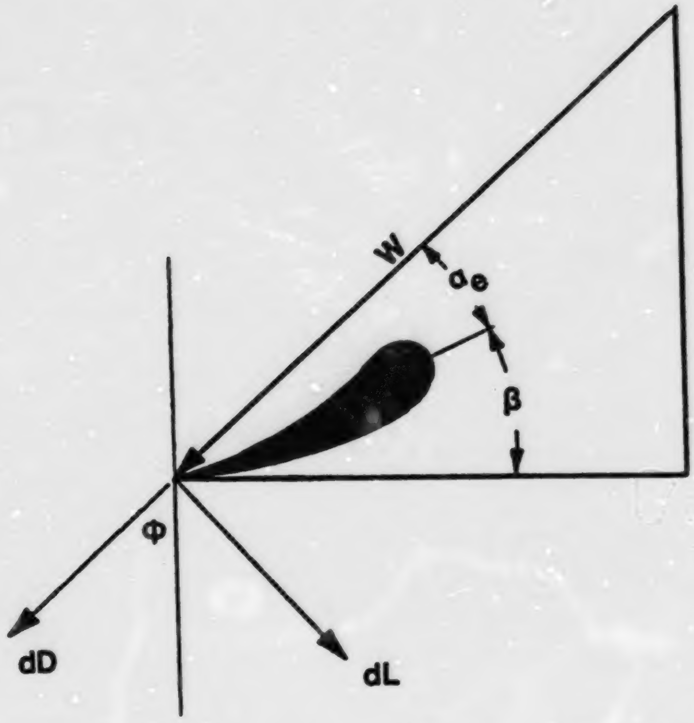
W
α_e
β
Φ
dD
dL

Fig. 3-4 Force components on a blade element

Chapter IV

PRESCRIBED WAKE ANALYSIS

In this chapter the prescribed wake analysis of horizontal axis wind turbines is discussed. As mentioned earlier, the problem of predicting blade performance is one of predicting the inflow distribution for a rotor blade. This inflow, however, is critically dependent on the vortex wake geometry which is, in turn, a function of the inflow distribution. Consequently, methods of predicting wind turbine performance are, in general, complex depending upon the operating conditions and the desired computational accuracy. A great simplification to this complicated problem results if the location of wake vortices are known a priori. The prescribed wake analysis takes advantage of such simplification by using an experimentally determined wake geometry as a part of the input data to the problem. The method can incorporate either a vortex line theory or a vortex surface theory. The wake consists of a number of trailing filaments (or sheets). The trajectories and positions of these filaments (or sheets) are prescribed through internal equations or input coordinates.

4.1 General Description of Model

In the present analysis it is assumed that each blade of the rotor is represented by a segmented bound vortex lifting line located along the quarter chordline of the rotor blade. It is further assumed that the bound vortex has spanwise varying concentrated vortex strength proportional to the local blade lift. The vortex wake is modeled by a system of segmented trailing vortices emanating from the junction of points of the bound vortex segment. The circulation of these trailing vortices is a function of spanwise bound circulation gradients. The trailing vortex segmentation is defined by a specified aximuthal step size. The infinite wake is approximated by a finite wake having a sufficient number of spirals.

4.2 Coordinate Systems

A blade-fixed cylindrical coordinate system as well as a blade-fixed Cartesian coordinate system are used in the formulation of the problem. The Cartesian coordinate axes X and Y form a plane of rotation and the Z axis is directed along the axis of rotation. In the cylindrical coordinate system the r-axis is coincident with the blade span, the θ-axis measures the azimuthal angle from the blade and the Z-axis is again the axis of rotation. Both coordinate systems are shown in Fig. 3-1.

4.3 Induced Velocity

Since detailed experimental data are sparse for the wake geometry of a wind turbine, an arbitrarily defined wake configuration is assumed for the purposes of the present work. The classical cylindrical wake geometry is assumed when expansion effects are not present. Two-dimensional momentum theory with Prandtl's tip-loss correction is used to define the position of wake filaments. The necessary equations are presented as follows for completeness.

The differential axial force on a wind turbine following momentum theory, Fig. 4-1, is given by, [45],

$$dF = \rho(2\pi r dr)V(V_o - V_2) = \rho(2\pi r dr)(V_o - w_a)(2w_a) \qquad (4\text{-}1)$$

where V_o is the freestream velocity, U is the wind velocity at the rotor disc, w_a is the axial component of the induced velocity, and V_2 is the wind velocity far downstream of the rotor. In addition, using blade element theory, [44],

$$dF = \frac{N}{2} \rho W^2 \; (C_L \cos\phi + C_D \sin\phi) \; c r dr \qquad (4\text{-}2)$$

where N is the number of blades, ϕ is the flow angle, W is the relative velocity at the blade element, C_L is the lift coefficient, C_D is the drag coefficient of the blade section, and c is the local blade chord. If the drag contribution to the axial force is neglected, equation (4-2) can be reduced to

$$dF = \frac{N}{2} \rho W^2 C_L \cos\phi \, c r dr \qquad (4\text{-}3)$$

The lift coefficient can be obtained from airfoil data. A straight line approximation of the airfoil data is

$$C_L = C_L(\alpha_e) \cong a_o \, \alpha_e \qquad (4\text{-}4)$$

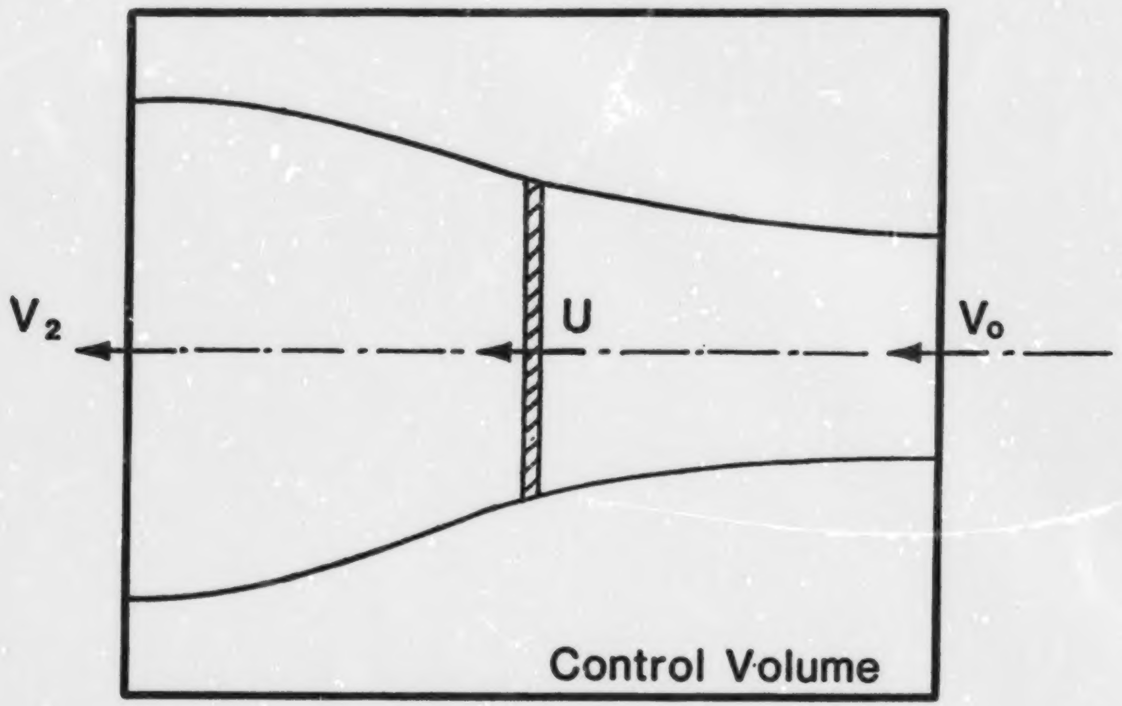
V_2
U
V_o
Control Volume

Fig. 4-1 The flow field and control volume for momentum theory

Reference to Fig. 4-2 reveals that the effective angle of attack is

$$\alpha_e = \phi - \beta - \alpha_i = \tan^{-1} \frac{V_0}{r\Omega} - \beta - \alpha_i \qquad (4\text{-}5)$$

The induced angle of attack, Fig. 4-2, is

$$\alpha_i = \tan^{-1} \frac{w_i}{W_u} \cong \frac{w_i}{\Omega R(\lambda_0^2 + \xi^2)^{1/2}} \qquad (4\text{-}6)$$

where $\lambda_0 = \frac{V_0}{\Omega R}$ and $\xi = \frac{r}{R}$. In obtaining the above equation, the small angle assumption is made and the magnitude of the undisturbed velocity is replaced by $W_u = \Omega R(\lambda_0^2 + \xi^2)^{1/2}$. In addition, the axial component of the velocity induced at a point r in the rotor plane is

$$w_a = w_i \cos\phi = \alpha_i W_u \cos\phi \qquad (4\text{-}7)$$

where

$$\phi = \tan^{-1} \frac{V_0}{\Omega r} = \tan^{-1} \frac{\lambda_0}{\xi} \qquad (4\text{-}8)$$

Substituting w_a from equation (4-7) into equation (4-1) yields

$$dF = \rho(2\pi r dr)(V - \alpha_i W_u \cos\phi)(2\alpha_i W_u \cos\phi) \qquad (4\text{-}9)$$

Combining equations (4-3), (4-8) and (4-9) yields

$$\alpha_i^2 - \left(\frac{\lambda}{\xi} + \frac{\sigma a_0}{\xi^2}\right)(\lambda_0^2 + \xi^2)^{1/2} + \frac{\sigma a_0}{8\xi^2} (\lambda_0^2 + \xi^2)^{1/2} (\phi - \beta) = 0$$

where

$$\sigma = \frac{Nc}{\pi R} \qquad (4\text{-}10)$$

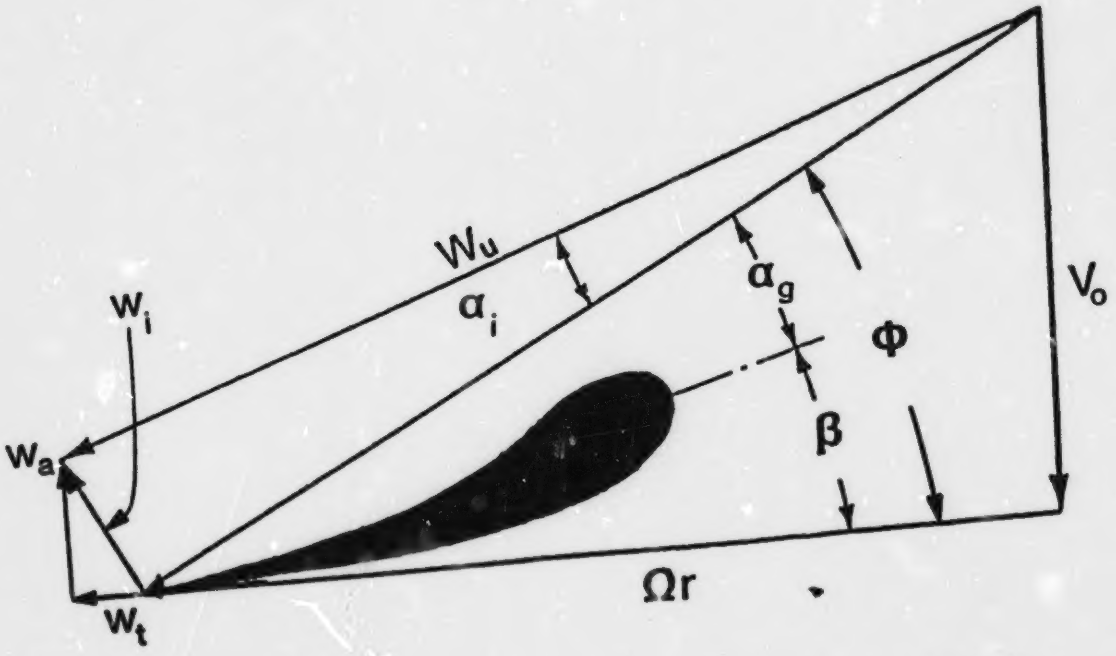
W_u
W_i
W_a
W_t
α_i
α_g
Φ
β
V_o
Ωr

Fig. 4-2 Velocity diagram showing the effect of induced velocity.

This quadratic equation can be readily solved to yield

$$\alpha_i = \frac{1}{2} [H_1^2 - (H_1^2 - 4H_2)^{1/2} \qquad (4\text{-}11)$$

where

$$H_1 = (\frac{\lambda}{\xi} + \frac{\sigma a_0}{8\xi^2})(\lambda_o^2 + \xi^2)^{1/2} \qquad (4\text{-}12)$$

and

$$H_2 = \frac{\sigma a_0}{8\xi^2} (\lambda^2_o + \xi^2)^{1/2} (\phi - \beta) \qquad (4\text{-}13)$$

From equations (4-11) and (4-6) one obtains

$$w_i = \frac{W_u}{2} [H_1 - (H_1^2 - 4H_2)^{1/2} \qquad (4\text{-}14)$$

Prandtl's tip-loss factor is defined as, [21],

$$F_{tip} = \frac{2}{\pi} \cos^{-1}\{\exp[- \frac{N(1+\lambda_0^2)}{2\lambda_o} (1-\xi)]\} \qquad (4\text{-}15)$$

This factor relates the circulation distribution of a rotor with a finite number of blades to its induced velocity by, [45],

$$\Gamma = \frac{4\pi r}{B} w_t(r) F_{tip} \qquad (4\text{-}16)$$

Referring to Fig 4-2 it can be seen that

$$w_t(r) = w_i(r) \sin \phi \qquad (4\text{-}17)$$

Equations (4-14), (4-15), (4-16) and (4-17) can be solved by an iterative procedure. Using the values of induced velocity, the wake geometry is constructed in the following manner,

$$x(r,\psi,z) = r\cos\psi$$

$$y(r,\psi,z) = r\sin\psi$$

$$z(r,\psi,z) = (V_o - w_a)\Delta\psi$$

where ψ is the azimuthal position of vortex filaments and varies by a finite step size between two consecutive points. Wake expansion can be estimated using two-dimensional momentum theory. The expansion, the ratio of radius of the wake far behind the rotor plane to the radius at the rotor disc, can be obtained from a mass balance equation. The mass flow through the rotor plane is $\pi R^2(V_o - w_a)$ and the mass flow far downstream of the rotor is $\pi R_2^2(V_o - 2w_a)$; thus

$$\frac{R_2^2}{R^2} = \frac{V_o - w_a}{V_o - 2w_a} = \frac{1-\bar{w}_a}{1-2\bar{w}_a} \qquad (4\text{-}18)$$

where $\bar{w}_a = \frac{w_a}{V_o}$. The radius of the wake at any axial position is approximated with an exponential form

$$R(z) = R_2 - (R_2 - R)\exp(-az) \qquad (4\text{-}19)$$

$$\text{where } a = -\frac{\left.\frac{dR}{dz}\right|_{z=0}}{R_2 - R}$$

The expansion in the above equation can be calculated at the tip from

$$\frac{dR}{dz} = \frac{w_r}{V_0 - w_z} \qquad (4\text{-}20)$$

where w_r and w_z are the radial and axial components of the velocity induced at the blade tip, and V_0 is the freestream velocity. However, the radial component of the induced velocity cannot be obtained from two-dimensional momentum theory. Instead an arbitrary point is used to define the exponential representation of the wake expansion.

Once the positions of wake points are prescribed, a set of equations is generated utilizing the Biot-Savart law, [14], the Kutta-Joukowski relationship, [19], and the airfoil section characteristics, [46, 47].

The disturbance velocity at the rotor plane due to a vortex sheet trailing from the blade can be calculated from the Biot-Savart law as

$$d\vec{w}_i = \frac{d\Gamma}{4\pi} \frac{d\vec{s} \times \vec{r}}{r^3} \qquad (4\text{-}21)$$

where $d\vec{w}_i$ is the differential velocity induced at a point A^* on the blade due to a vortex filament, $d\vec{s}$, and $\vec{r}$ is the position vector from point A on the blade to the element ds. The differential change in circulation between spanwise locations r and r+dr, is $d\Gamma$. This differential circulation is, of course, equal to the strength of the vortex trailing from the element of blade dr. Vectors $d\vec{s}$ and $\vec{r}$ are shown in Fig. 4-1. The components of this velocity in a Cartesian coordinate system are given as, (see section 5-2 for details),

$$w_x(A) = \frac{\Gamma(r_1+r_2)}{2\pi r_1 r_2[(r_1+r_2)^2-L^2]}[(y_A-y_C)(z_C-z_B)-(z_A-z_C)(y_C-y_B)] \quad (4\text{-}22)$$

$$w_y(A) = \frac{\Gamma(r_1+r_2)}{2\pi r_1 r_2[(r_1+r_2)^2-L^2]}[(z_A-z_C)(x_C-x_B)-(x_A-x_C)(z_C-z_B) \quad (4\text{-}23)$$

$$w_z(A) = \frac{\Gamma(r_1+r_2)}{2\pi r_1 r_2[(r_1+r_2)^2-L^2]}[(x_A-x_C)(y_C-y_B)-(y_A-y_C)(x_C-x_B)] \quad (4\text{-}24)$$

where

$$r_1 = [(x_A-x_B)^2 + (y_A-y_B)^2 + (z_A-z_B)^2]^{1/2} \quad (4\text{-}25)$$

The quantities r_2 and L can be found similarly.

The Kutta-Joukowski equation for two-dimensional flow is

$$L = \rho W\Gamma \quad (4\text{-}26)$$

Here L is the lift per unit span normal to W, the relative velocity , which is produced by the circulation Γ. The section lift coefficient of the airfoil is defined as

$$C_L = \frac{L}{1/2\ \rho W^2 c} \quad (4\text{-}27)$$

and can be obtained from suitable two-dimensional wind tunned data i.e.,

$$C_L = C_L\ (\alpha_e) \quad (4\text{-}28)$$

Combining equations (4-26), (4-27) and (4-28) yields

$$\Gamma = 1/2\ WcC_L$$

This set of equations can be solved to obtain the blade circulation distribution and then the angle of attack distribution. In general, the solution must be obtained numerically using an iterative technique since it is not always possible to have an explicit equation for the section lift coefficient. The blade loadings and performance are then calculated using equations (3-28) to (3-32) with the aid of two-dimensional airfoil data.

4.4 Numerical Procedure

The numerical procedure for computing the inflow distribution and loading on the blades is presented in this section. In general the method utilizes an iterative technique to determine blade section characteristics using realistic two-dimensional airfoil data. To start the iteration process, a first approximation of the inflow distribution may be made by two-dimensional momentum theory results, i.e., equation (4-14). The iteration process is as follows:

1) Use an inflow velocity for each spanwise location to obtain the induced angle of attack;
2) Calculate the local angle of attack distribution;
3) Compute the circulation distribution;
4) Compute the local induced velocity components;
5) Calculate the new local inflow distribution; and
6) Compare the most recently calculated inflow velocity to the previous value, if they are equal, stop; otherwise go to step 2.

Chapter V

FREE WAKE ANALYSIS

In this chapter a free wake analysis of a horizontal axis wind turbine is performed. Two separate analytical approaches are used. One develops a model that is a logical extension of the work done by Miller, [12], for hovering helicopters. This analysis is referred to as the fast free wake analysis. The other, termed a simplified free wake analysis, is a new attempt to analyze the complex wake of wind turbines without constraining it from moving and deforming freely under the influence of free vortices and self-induced effects.

The problem will be treated in classical fashion by replacing the rotor blade and wake by distributed vorticity and treating the fluid motion as a potential flow. The disturbance velocities may then be obtained by application of the Biot-Savart law. The free stream is assumed to be steady, uniform and parallel to the axis of rotation. This simplifies the problem somewhat in that azimuthal symmetry for a multi-blade configuration exists. This in turn permits the problem to be solved on one reference blade with identical conditions existing on the other blades. The velocity and circulation distributions, therefore, need only be computed for one blade.

Once the wake geometry and inflow distribution are established using the potential flow models, the final results are calculated by correcting for real fluid effects using existing two-dimensional airfoil data at each blade section.

The mathematical models, the equations that govern the flow field and important mathematical relationships, are presented in the following.

5.1 Fast Free Wake Analysis

In this analysis the wake of a wind turbine is modeled after the earlier analysis of Miller, [12]. In that work it was shown that blade loads for a helicopter in forward flight can be accurately predicted by replacing the vortex system close to the blade with straight vortex lines. This vortex wake model, modified for a wind turbine, is given in the next section.

5.1.1 Vortex Wake Model

The wake is composed of three parts: a near wake, an intermediate wake and a far wake.

The near wake consists of a number of straight semi-infinite vortex lines, as shown in Fig. 5-1. The effect of replacing the actual curved wake with a system of straight semi-infinite vortices is discussed in Ref. [12]. The differences were shown to be negligible. The near wake forms that portion of the wake immediately behind the rotor.

The intermediate wake model is depicted in Fig. 5-2. This wake is made up of a series of vortex rings. A first rolled-up vortex ring is assumed to form from the trailing vortex lines emanating from the blade tip to a point of maximum circulation. A second roll up occurs from this point to a point where circulation changes abruptly again. A third vortex ring forms from this point to the rotor hub. For a two-blade rotor configuration, each of these vortex rings is assumed to form in the following fashion. The wake between $\psi=\pi/2$ and $3\pi/2$ from the first blade joins that of the second blade between $\psi=3\pi/2$ and $\psi=5\pi/2$ to form a vortex ring. Additional vortex rings are formed in a similar manner. The number of vortex rings in the intermediate wake is arbitrarily assigned. However, a minimum of four vortex rings has been found necessary for consistent results. The vortex rings for a rotor with more than two blades are formed analogously. The vortex system representing the approximate wake should be inclined at an angle since the vortex system generated by the motion of blades follows a helical path. The inclination angle is the angle whose tangent is given by the ratio of the local axial velocity over the local tangential velocity of air with respect to the rotor. This effect, however, has been found to be negligible, [12].

A semi-infinite vortex cylinder forms the far wake. It originates one wake spacing from the last vortex ring of the intermediate wake. This wake model is shown in Fig. 5-3.

The radii and spacings of vortex rings are obtained from the velocities in the wake. These velocities are composed of the freestream

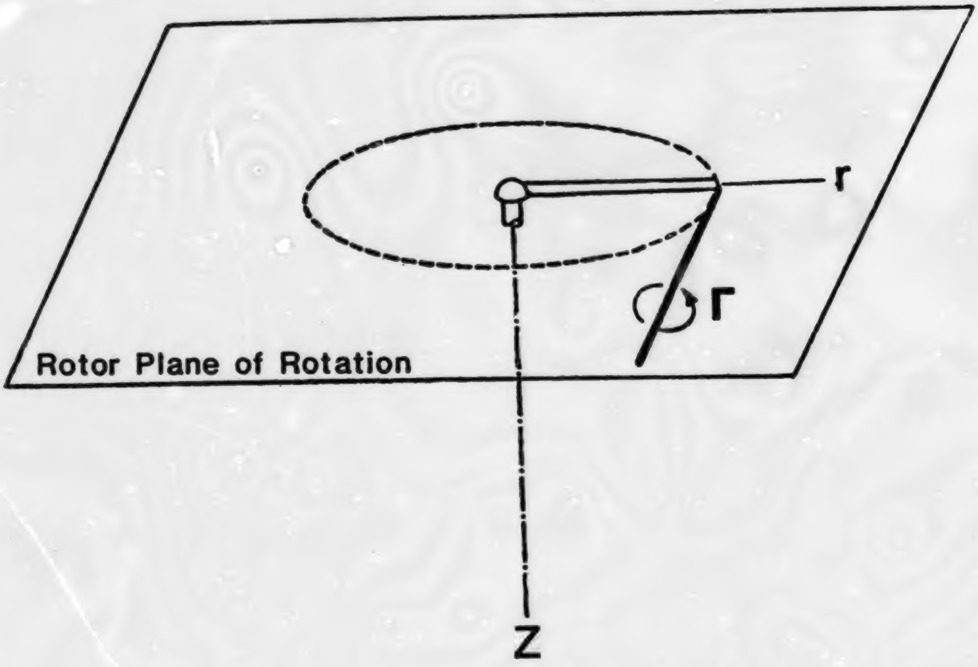
r
Γ
Rotor Plane of Rotation
Z

Fig. 5-1(a) Near wake vortex model. Tip vortex only.

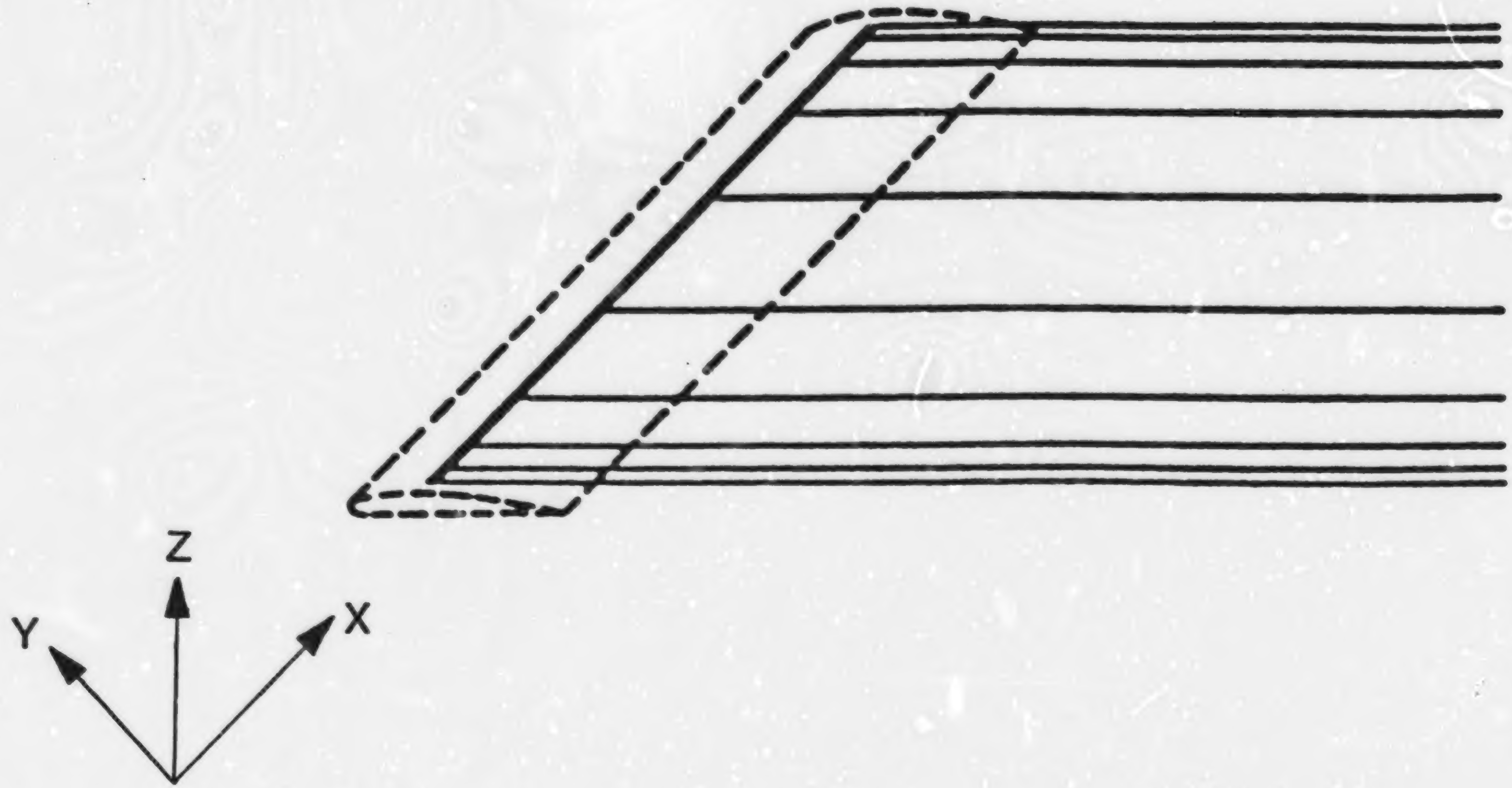

Fig. 5-1(b) Near wake vortex system

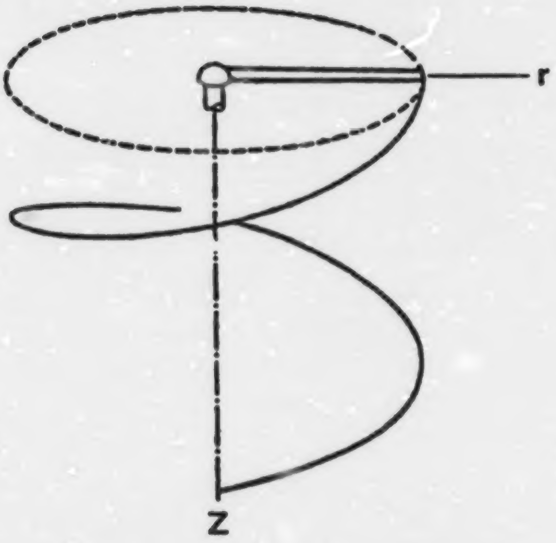

Fig. 5-2(a) Actual vortex wake. Only tip vortex shown.

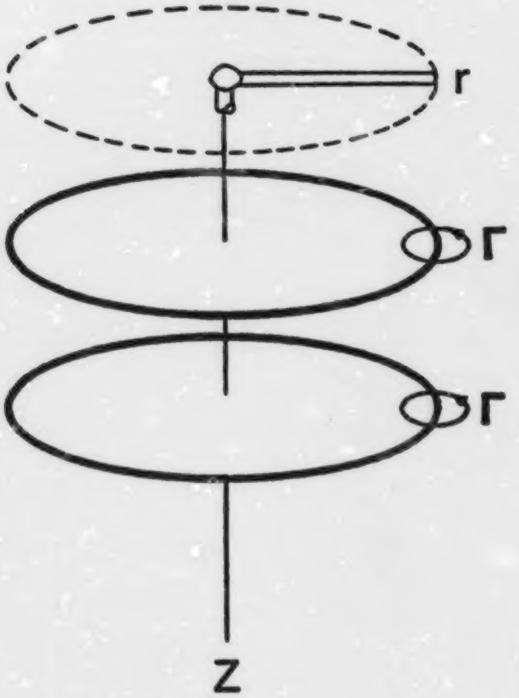

Fig. 5-2(b) Vortex ring model. Only tip vortex shown.

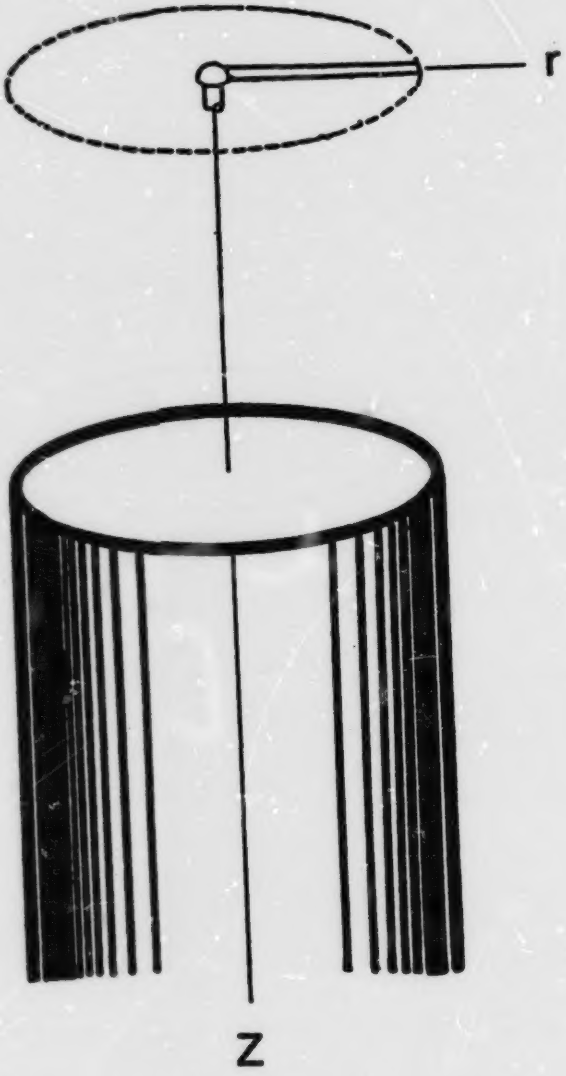

Fig. 5-3 Far vortex wake model.

velocity and the induced velocities. The procedure for determing the induced flow is given in the following section.

5.1.2 Formulation of Problem

The induced velocity at a point P located at a distance r' from the axis of rotation and at an azimuthal position relative to an element of vorticity of strength Γ located a distance r from the axis of rotation is given by the Biot-Savart law [18], i.e., equation (3-1). The components of velocity induced at ξ by semi-infinite vortex lines located at ξ and $-\xi$, Fig. 5-4, are

$$w = \frac{\Gamma}{2\pi R}\left[\frac{\xi-\xi'}{(\xi-\xi')^2+\zeta^2} + \frac{\xi+\xi'}{(\xi+\xi')^2+\zeta^2}\right] \tag{5-1}$$

and

$$u = \frac{\Gamma}{2\pi R}\left[\frac{\zeta}{(\xi-\xi')^2+\zeta^2} + \frac{\zeta}{(\xi+\xi')^2+\zeta^2}\right] \tag{5-2}$$

where

$$\xi = \frac{r}{R} \tag{5-3}$$

$$\xi' = \frac{r'}{R} \tag{5-4}$$

$$\zeta = \frac{z}{R} \tag{5-5}$$

are dimensionless coordinates.

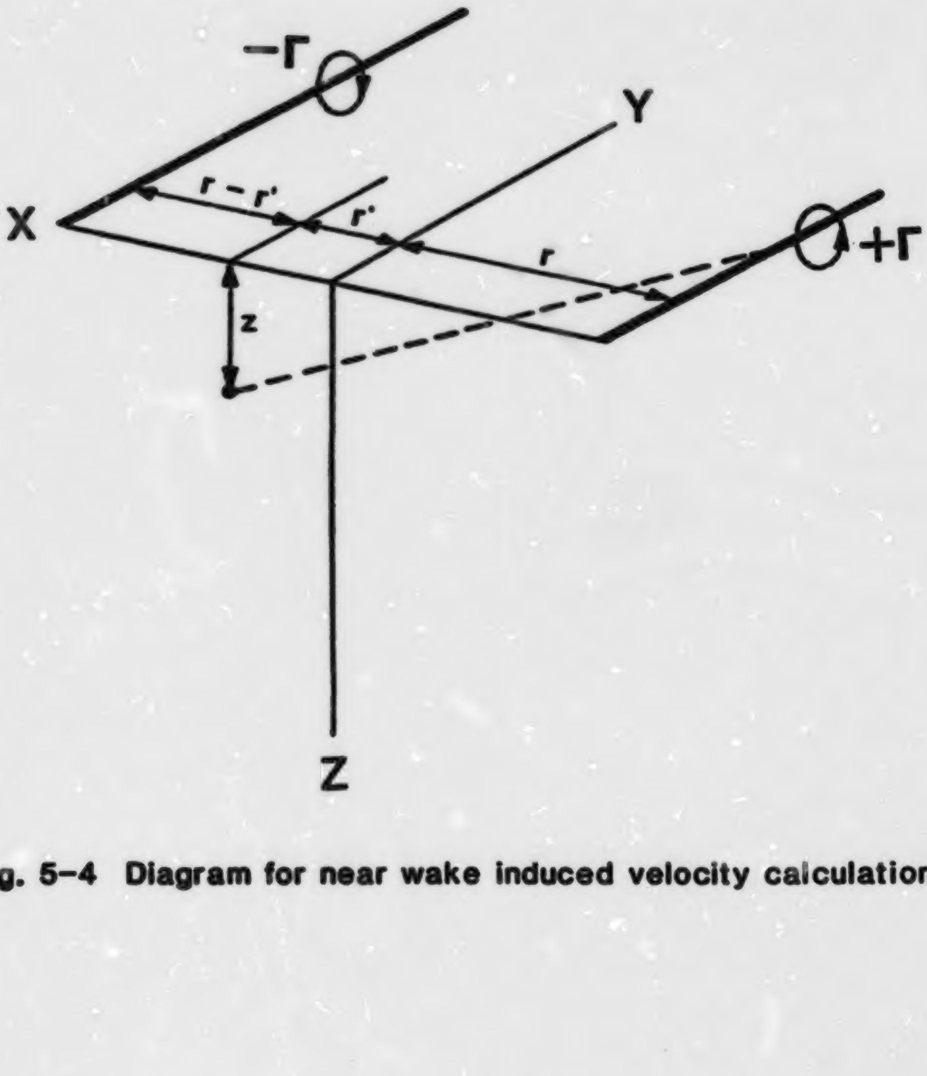
−Γ
Y
X
r − r'
r'
r
+Γ
z
Z

Fig. 5-4 Diagram for near wake induced velocity calculations.

For an element of a vortex ring, the Biot-Savart law gives

$$d\vec{w}_i = \frac{\Gamma}{4\pi}\,\frac{d\vec{s} \times \vec{L}}{L^3} \tag{5-6}$$

where

$$\vec{L} = L_1\hat{i} + L_2\hat{j} + L_3\hat{k}$$

$$L_1 = r - r'\cos\psi = R(\xi - \xi'\cos\psi)$$

$$L_2 = r'\sin\psi = R\xi'\sin\psi$$

$$L_3 = z = R\zeta$$

$$L = (L_1{}^2 + L_2{}^2 + L_3{}^2)^{1/2}$$

$$ds_1 = 0$$

$$ds_2 = rd\psi = R\xi d\psi$$

$$ds_3 = (rd\psi)\tan\phi = R\xi\tan\phi d\psi$$

and ϕ is the wake spiral angle. Assuming that the element ds is parallel to the plane of rotation of the blade, that is, the vortex spiral is replaced by a horizontal vortex ring, $ds_3 = 0$. The incremental Z-component of induced velocity is, then, given by

$$dw = \frac{\Gamma}{4\pi}\,\frac{L_1 ds}{L^3} = \frac{\Gamma}{4\pi R}\,\frac{(\xi - \xi'\cos\psi)\xi d\psi}{(\xi'^2 + \xi^2 - 2\xi\xi'\cos\psi + \zeta^2)^{3/2}}$$

and the incremental radial component by

$$du = \frac{\Gamma}{4\pi}\,\frac{L_3 ds\cos\psi}{L^3} = \frac{\Gamma}{4\pi R}\,\frac{\xi\zeta'\cos\psi d\psi}{(\xi^2+\xi'^2-2\xi\xi'\cos\psi+\zeta^2)^{3/2}} \qquad (5\text{-}8)$$

For a vortex ring the above equations are integrated from 0 to 2π

$$w = \frac{\Gamma}{4\pi R}\int_0^{2\pi}\frac{\xi(\xi-\xi'\cos\psi)d\psi}{(\xi^2+\xi'^2-2\xi\xi'\cos\psi+\zeta^2)^{3/2}} \qquad (5\text{-}9)$$

$$u = \frac{\Gamma}{4\pi R}\int_0^{2\pi}\frac{\zeta'\xi\cos\psi d\psi}{(\xi^2+\xi'^2-2\xi\xi'\cos\psi+\zeta^2)^{3/2}} \qquad (5\text{-}10)$$

These equations can be integrated using a change of variable, $\theta = \pi - 2\psi$, to give

$$w = \frac{\Gamma}{4\pi R}\left(\frac{k^2}{\xi\xi'}\right)^{1/2}\frac{K-E\,[1-1/2k^2(1+\xi/\xi')]}{1-k^2} \qquad (5\text{-}11)$$

$$u = \frac{\Gamma}{4\pi R}\,\frac{\zeta}{2\zeta'}\left(\frac{k^2}{\xi\xi'}\right)^{1/2}\left[\frac{E(2-k^2)}{1-k^2} - 2k\right] \qquad (5\text{-}12)$$

where

$$k^2 = \frac{4\xi'\xi}{\xi^2+\xi'^2+\zeta^2}$$

and

$$K = \int_0^{\pi/2} \frac{d\theta}{(1-k^2\sin^2\theta)^{1/2}}$$

$$E = \int_0^{\pi/2} (1-k^2\sin^2\theta)^{1/2}\, d\theta$$

The quantities K and E are elliptic integrals of the first and second kind respectively.

The horizontal and vertical values of induced velocities due to semi-infinite vortex cylinders representing the far wake are obtained from

$$w = \frac{1}{4\pi R}\frac{d\Gamma}{d\zeta} \int_0^{2\pi} \frac{\xi(\xi-\xi'\cos\psi)}{(\xi^2+\xi'^2-2\xi\xi'\cos\psi)^{1/2}} \left[1 - \frac{\zeta}{(\xi^2+\xi'^2-2\xi\xi'\cos\psi+\zeta^2)^{1/2}}\right] d\psi \qquad (5\text{-}13)$$

$$u = \frac{1}{4\pi R}\frac{d\Gamma}{d\zeta} \int_0^{2\pi} \frac{\xi\cos\psi}{(\xi^2+\xi'^2+\zeta^2-2\xi\xi'\cos\psi)^{1/2}}\, d\psi \qquad (5\text{-}14)$$

In order to determine wind turbine performance parameters, blade loading, power, etc., the effective angle of attack for the particular blade airfoil section is needed. In turn, this angle is related to the airfoil lift and drag characteristics. The section effective angle of attack is obtained as

$$\alpha_e = \alpha_g - \alpha_i \tag{5-15}$$

The section airfoil characteristics then can be found from appropriate experimental data

$$C_L(\alpha_e) = f(\alpha_e) \tag{5-16}$$

$$C_D(\alpha_e) = g(\alpha_e) \tag{5-17}$$

The local values of axial force and torque, blade loads and performance are, then, calculated analogous to that of section 3-6.

5.1.3 Computation Procedure

An iterative approach is used for the solution. Figure 5-6 is a flow diagram of the computational procedure. The calculation begins with an assumed wake spacing and circulation distribution. The induced velocities are then computed everywhere in the wake. A new wake geometry is calculated using existing velocities in the wake. This new geometry is then used in the computation of blade induced velocities and the circulation distribution. The calculations continue until the induced flow takes on a value consistent with the final wake.

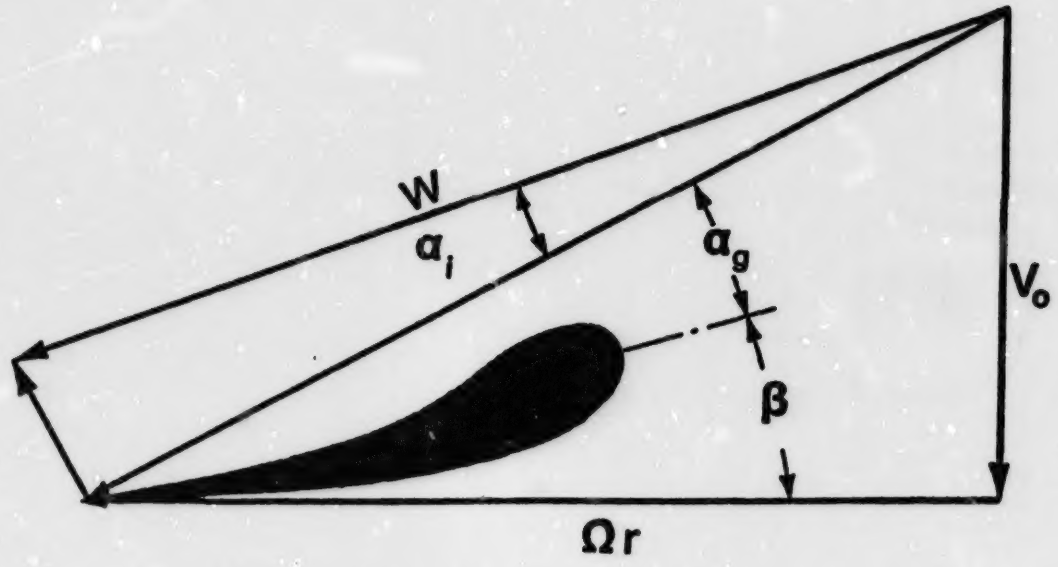
W
α_i
α_g
β
V_o
Ωr

Fig. 5-5 Velocity diagram showing the effect of induced velocity.

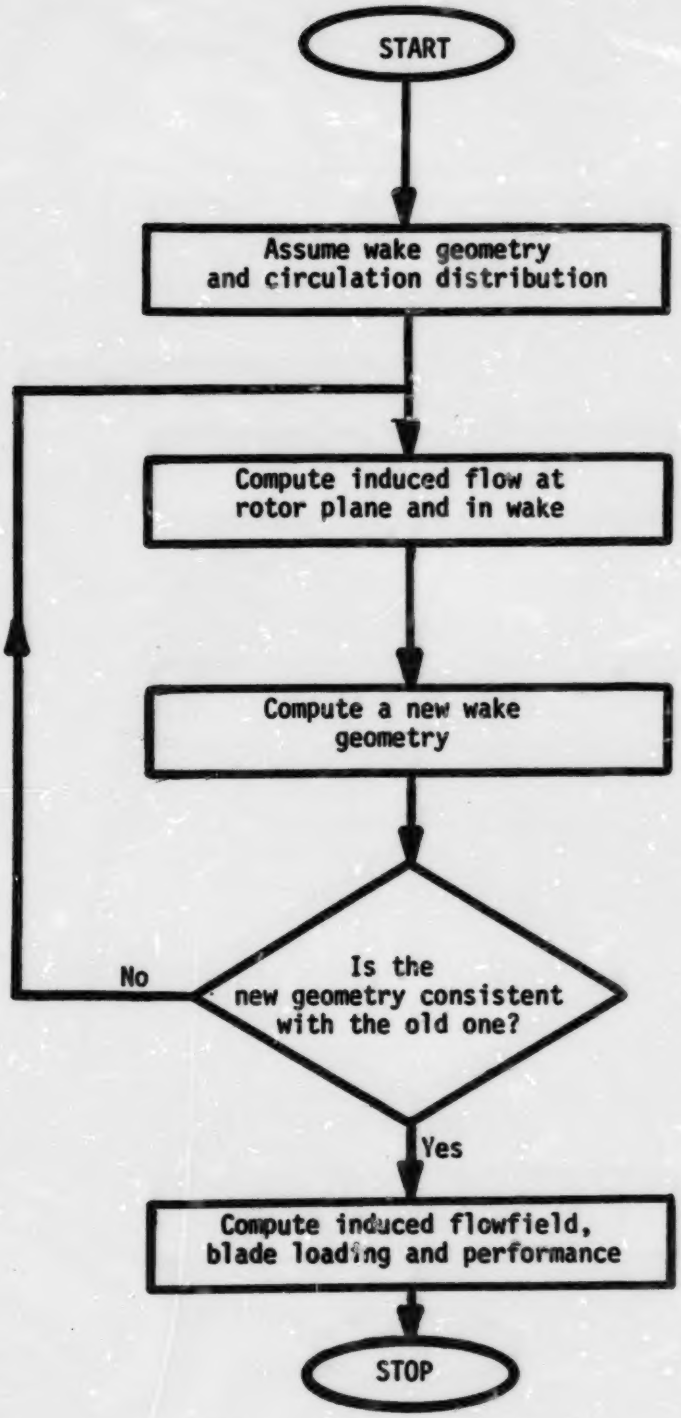
START
Assume wake geometry and circulation distribution
Compute induced flow at rotor plane and in wake
Compute a new wake geometry
Is the new geometry consistent with the old one?
No
Yes
Compute induced flowfield, blade loading and performance
STOP

Fig 5–6 Flow diagram of fast free wake computation procedure

5.2 Simplified Free Wake Analysis

In developing this new vortex wake model, use has been made of the experimental results of Gray, [2], and Landgrebe, [4]. Gray demonstrated that the wake of a rotary wing consists of a concentrated tip vortex and a weak inboard wake. This vortex arrangement will be used in the formulation of the proposed model.

The local velocity at the rotor plane consists of the free stream velocity, the blade motion and the wake induced velocities. In order to predict the inflow at the blades, it is necessary to describe the blade surfaces and the wake. The blades are simply lifting surfaces of finite span. The wake consists of trailing streamwise vorticity which accounts for spanwise variation in loading. These trailing vortex filaments travel in a generally helical path due to the rotor rotation, and distort under their own self-induced effects as well as the influence of other filaments. The resulting wake is assumed to consist of an intense tip vortex and a weak, diffused inboard wake. The vortex filaments shed from the radial locations outboard of the maximum blade bound vortex strength are assumed to join together to form a strong tip vortex. The inboard wake will, then, consist of vortices shed from the inboard sections of the blade's trailing edge. This wake arrangement is shown in Fig. 5-7.

The complexity of flow field precludes any hope of a closed form solution; hence a numerical method employing a vortex lattice technique is used.

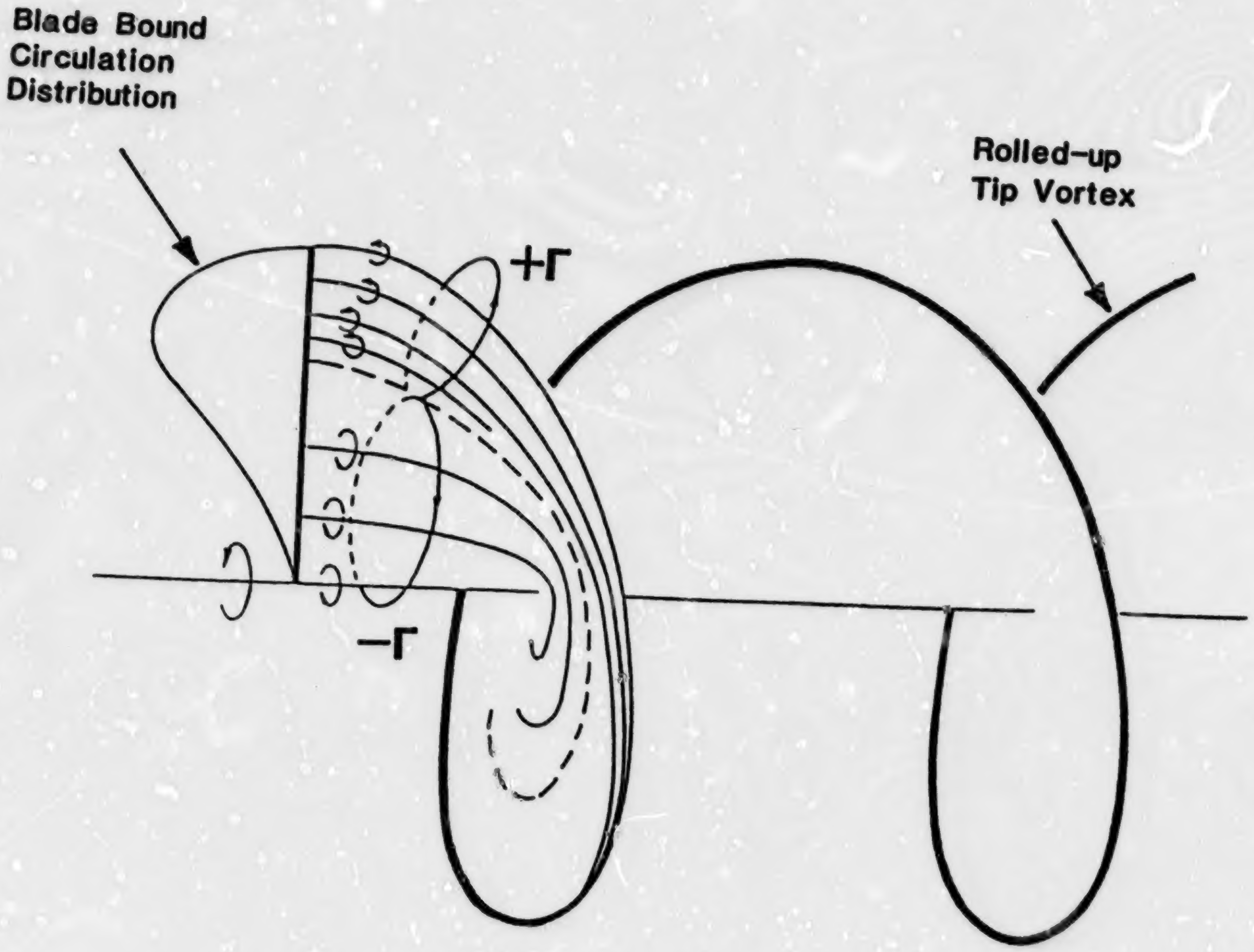
Blade Bound
Circulation
Distribution
Rolled-up
Tip Vortex
+Γ
−Γ

Fig. 5-7 Physical model of the flow field.

5.2.1 Description of Numerical Model

The numerical model for the blade consists of radially distributed vortex lattices, or panels, each of which is considered as having a constant vortex strength. Each resulting panel contains a control point located on the local chord at $x+\Delta x/2$ for the segment between x and $x+\Delta x$. The arrangements of panels and control points are depicted in Fig. 5-8. The panel is spanned by a straight-line vortex segment located 1/4 chord back from the leading edge. Segments may have sweep reflecting a variable chord. One requirement of this straight-line representation is that the spanwise segments be small enough that the chord variation is adequately represented by straight line segments between x and $x+\Delta x$. Typical wind turbine rotors will fulfill this requirement adequately except perhaps at the blade tips.

The wake consists of a system of trailing vortices the strength of which accounts for any spanwise variation in loading. The strength of each vortex is that of the vortex as it leaves the blade. The wake contains a finite number of points whose motion describes the deformation. These points are taken to be connected by straight line vortex segments which represent the disturbance. Also, no deformation of the straight line vortex is permitted. The induced velocity is computed at the end points by application of the Biot-Savart law.

In this simplified free vortex analysis the wake is divided into two parts: a near wake and a far wake. The near wake consists of the first π radians of azimuthal displacement. No deformation of this wake vortex

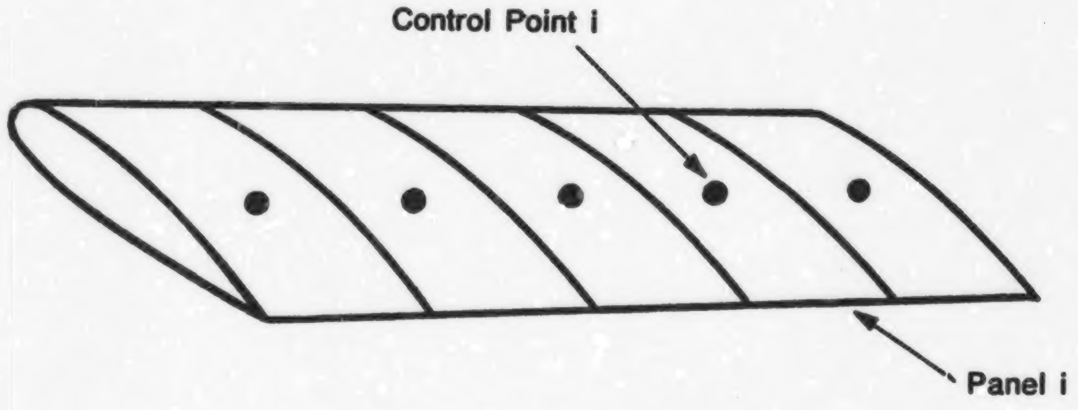
Control Point i
Panel i

Fig. 5-8 Blade panel and control point arrangements

is allowed. The trailing vortices shed from outboard blade sections from the point of maximum circulation are assumed to join together to form a strong tip vortex. Although there is clear experimental evidence of the existence of an intense rolled-up tip vortex [2,3,4], relatively little is presently known regarding the mechanism of vortex wake roll-up as well as the numerical modeling of the phenomenon. Hence, for the present analysis, it is assumed that this roll-up occurs almost immediately. Consequently, the far wake will consist of an inboard wake in which trailing vortex filaments follow a helical path and a rolled-up strong tip vortex which is permitted to deform. The inboard wake vortices are assumed to move with local velocities at the rotor plane. The vortex wake is truncated after a few revolutions. A sketch of the flow model of the wake used in the computations is provided in Fig. 5-9.

5.2.2 Coordinate Systems

The problem is investigated in two coordinate systems. A blade fixed Cartesian coordinate system is used to study the wake deformation as well as the blade force determination. The origin of this coordinate system is fixed at the axis of rotation, X directed along the span, Y laid in the rotor plane and Z along the axis of rotation. Hence X and Y, lying in the disc plane, rotate with the blade as shown in Fig. 5-10.

A rotor disk-plane fixed coordinate system is also used to study wake deformation. This system allows a wake visualization as might be seen in a wind tunnel or real environment. X and Y are orthogonal but

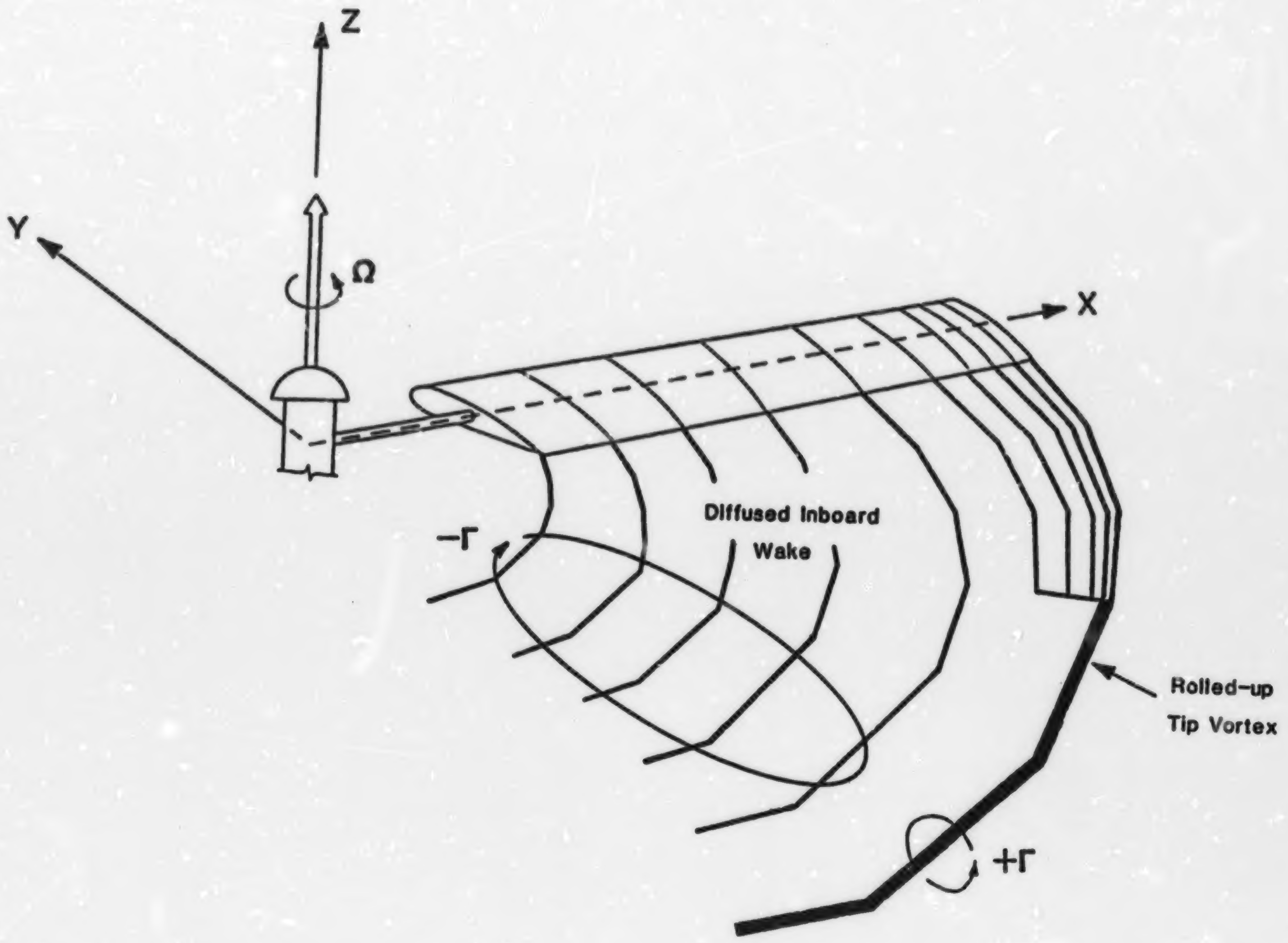
Z
Y
Ω
X
Diffused Inboard
Wake
−Γ
Rolled-up
Tip Vortex
+Γ

Fig. 5-9 Numerical model of the wake.

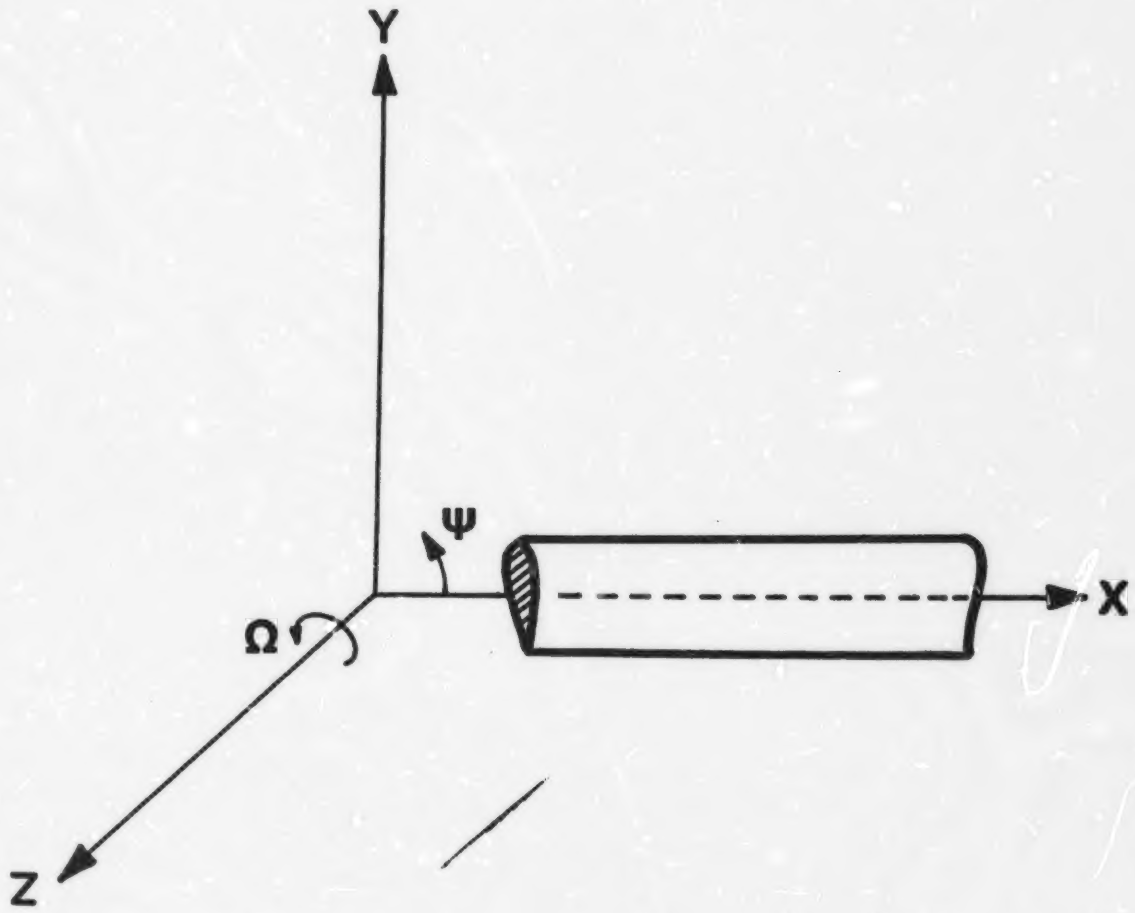

Fig. 5–10 Rotor–blade fixed coordinate system

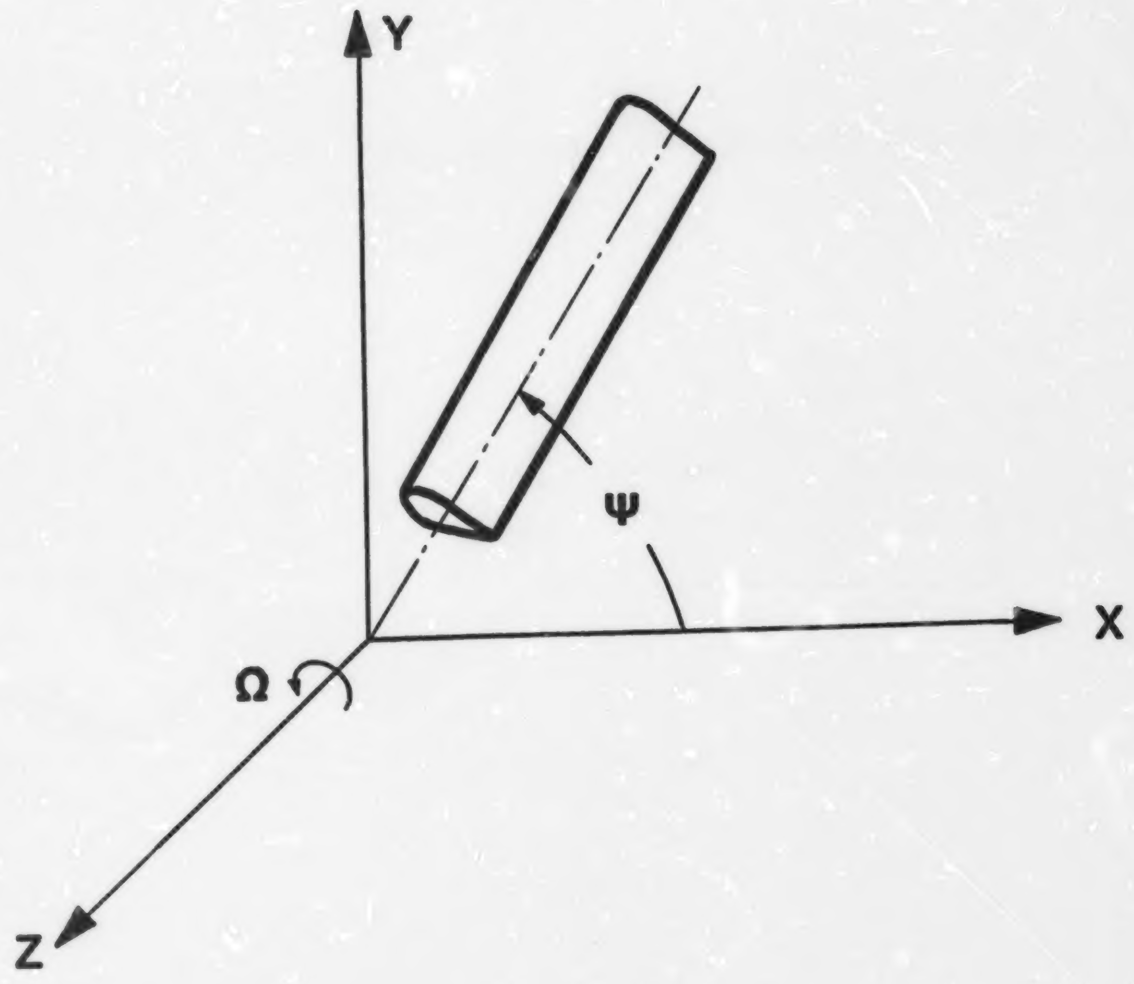

Fig. 5-11 Rotor-disc fixed coordinate system.

fixed in a direction so that the blades rotate relative to them. Z is also perpendicular to the disk plane, Fig. 5-11.

5.2.3 Elementary Flow Field

As previously described, the blade surfaces are replaced by a number of spanwise vortex lattices (panels), each spanning a straight line vortex of constant strength. The trailing vortices are laid down in a finite number of straight line segments which describe the wake motion. Hence at a point in space and time, the disturbance flow field is that due to a number of straight line vortex segments.

The increment of induced velocity at a point A of Fig. 5-12 due to a differential vortex ds according to the Biot-Savart law is

$$d\vec{w}_i = \frac{\Gamma}{4\pi} \frac{d\vec{s} \times \vec{r}}{r^3} \qquad (5\text{-}18)$$

where $d\vec{s}$ is an element of vortex strength Γ and $\vec{r}$ is the position vector from point A to the element $d\vec{s}$. Hence the induced velocity due to a straight vortex line with end points at B and C, see Fig. 5-12, is obtained by integrating equation (5-18) over the vortex line length. Noting that

$$d\vec{s} = \frac{h}{\sin^2\theta}\, d\theta\, \vec{e}_1$$

and

$$\vec{r} = \frac{h}{\sin\theta}\, \vec{e}_2$$

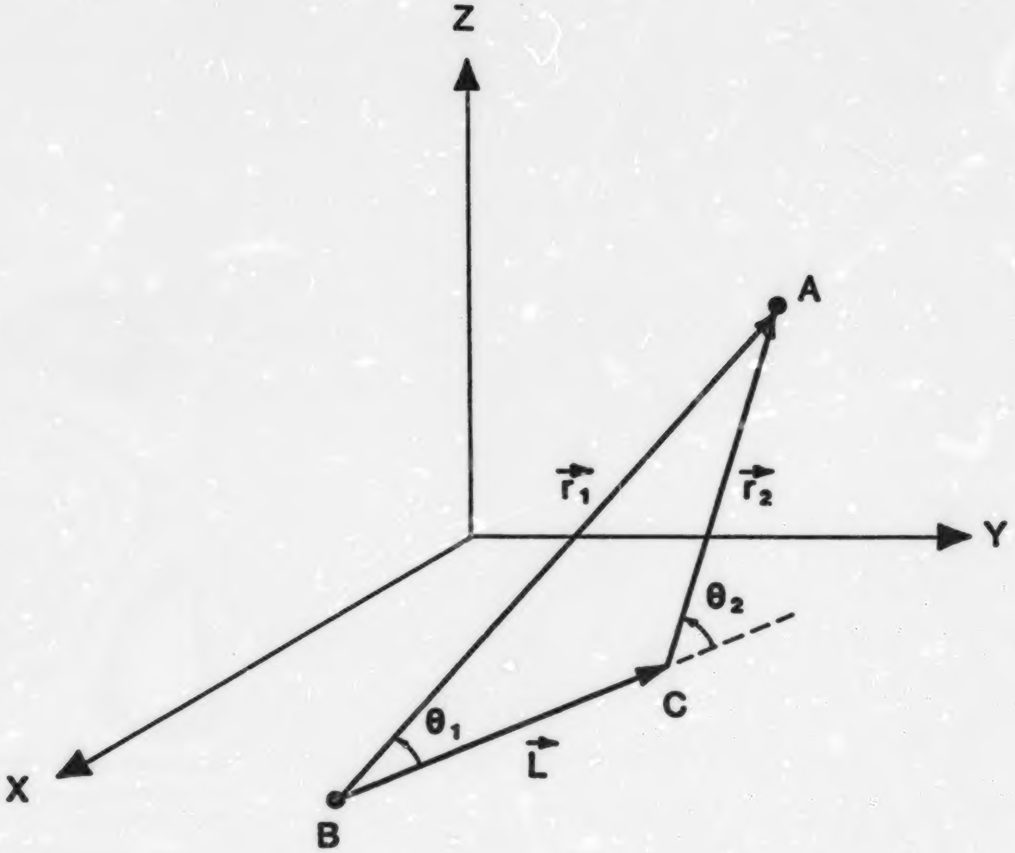
Z
A
$\vec{r}_1$
$\vec{r}_2$
Y
θ_2
C
θ_1
$\vec{L}$
X
B

Fig. 5-12 Induced velocity calculation by straight vortex filaments

where $\vec{e}_1$ and $\vec{e}_2$ are unit vectors in the direction of $d\vec{s}$ and $\vec{r}$, respectively, integration yields

$$\vec{w}_i(A) = \frac{\Gamma}{h}\,\frac{\cos\theta_1-\cos\theta_2}{4\pi}\,\vec{n} \tag{5-19}$$

where

$\vec{n}$ = unit normal vector to plane containing A, B and C

$$= \frac{\vec{L} \times \vec{r}_2}{\left|\vec{L} \times \vec{r}_2\right|}$$

and $h = r_2 \sin\theta_2$.

In addition, using $\left|\vec{L}\times\vec{r}_2\right| = \left|\vec{L}\right|\left|\vec{r}_2\right|\sin\theta_2$, equation (5-19) can be written as

$$\vec{w}_i(A) = \frac{\Gamma L}{4\pi}\,\frac{\vec{L} \times \vec{r}_2}{\left|\vec{L} \times \vec{r}_2\right|^2}\,(\cos\theta_1 - \cos\theta_2) \tag{5-20}$$

$$w_{ix}(A) = \frac{\Gamma(r_1+r_2)}{2\pi r_1 r_2[(r_1+r_2)^2-L^2]}\,[(y_A-y_C)(z_C-z_B)-(z_A-z_C)(y_C-y_B)] \tag{5-21}$$

$$w_{iy}(A) = \frac{\Gamma(r_1+r_2)}{2\pi r_1 r_2[(r_1+r_2)^2-L^2]}\,[(z_A-z_C)(x_C-x_B)-(x_A-x_C)(z_C-z_B)] \tag{5-22}$$

$$w_{iz}(A) = \frac{\Gamma(r_1+r_2)}{2\pi r_1 r_2[(r_1+r_2)^2-L^2]}\,[(x_A-x_C)(y_C-y_B)-(y_A-y_C)(x_C-x_B)] \tag{5-23}$$

where

$$r_1 = [(x_A-x_B)^2 + (y_A-y_B)^2 + (z_A-z_B)^2]^{1/2}$$

The quantities r_2 and L can be found in a similar fashion.

Superposition of the results of equations (5-21), (5-22) and (5-23) for all the elements of the vortex representing the blade and wake give the components of disturbance velocity at any point in the field.

5.2.4 Deformation of the Wake

As a consequence of circulation variation, a vortex sheet (wake) is shed from the trailing edge of a blade. Wake models for rotors are modifications of those of a finite wing. The thickness of the wake of a finite wing is equal to the wing boundary thickness at the trailing edge, and,as is well known [48], the separated boundary layer of the sheet gradually rolls up into a discrete concentration of vorticity.

Batchelor [49] has shown that in the rolling up of a wake, two distinct processes occur simultaneously: the deformation of the wake sheet and the concentration of vorticity by convection. This combined event presents an extremely complicated problem, and is generally avoided when calculating airloads by assuming the existence of a wake model. This model, which originated from ideas of Prandtl, assumes that the wake is an infinitely thin flat sheet. For rotors, the analogous wake model is that formulated by Goldstein which assumes a thin, fixed pitch, helical sheet of vorticity. Moreover, no wake roll-up is permitted.

Although the existence of wake roll-up is well documented [2,3,4], as mentioned earlier, the mechanism of vortex wake roll-up is not well understood. Nor for that matter is the numerical modeling of the phenomenon. For this reason, for the purposes of the present analysis it is assumed that the wake behind a rotor in steady flow is composed of two regions: a near field where no roll-up or deformation of the wake is considered, and a far field where roll-up is essentially complete.

Wake convection and deformation occur due to freestream velocity, V_0, rotational speed, Ω, and the disturbance velocity, w_i. The components of freestream velocity at a point P which is located at a distance r from the axis of rotation and at an azimuthal angle ψ from the blade with respect to the blade-fixed coordinate system is

$$V_x^* = -r\Omega\sin\psi$$
$$V_y^* = r\Omega\cos\psi$$
$$V_z^* = -Vo$$

where Ω is the angular velocity of the rotor and V_0 is the wind velocity, or, in terms of dimensionless parameters,

$$V_x = -\xi\sin\psi$$
$$V_y = \xi\cos\psi$$
$$V_z = -Vo$$

Therefore the velocity components at a point P are

$$V_x = -\xi\sin\psi + w_{ix}$$
$$V_y = \xi\cos\psi + w_{iy}$$
$$V_z = -\mu_0 + w_{iz}$$

where w_{ix}, w_{iy} and w_{iz} are the components of velocity induced at P. In the time increment Δt, the rotor has turned through an angle $\Delta\psi = \Omega\Delta t$, and the point P has moved to a new position given by

$$x(t+\Delta t) \equiv x(t) + V_x \, \Delta\psi$$

$$y(t+\Delta t) \equiv y(t) + V_y \, \Delta\psi$$

$$z(t+\Delta t) \equiv z(t) + V_z \, \Delta\psi$$

All parameters in these equations are dimensionless.

For the case of a rotor disk-plane fixed coordinate system, the wake convection can be obtained in a similar fashion. Let x(t), y(t) and z(t) be the coordinates of a point P at time t. The position of this point at a time $t+\Delta t$ is obtained as

$$x(t+\Delta t) \equiv x(t) + w_{xi} \, \Delta\psi$$

$$y(t+\Delta t) \equiv y(t) + w_{yi} \, \Delta\psi$$

$$z(t+\Delta t) \equiv z(t) + (V_0 - w_{zi}) \, \Delta\psi$$

5.2.5 Self-Induced Velocity

The localized induction contribution to the induced velocity has been determined to be [50, 51, 52]

$$\vec{q}_i = \frac{\dfrac{\partial \vec{r}}{\partial s} \; \dfrac{\partial^2 \vec{r}}{\partial s^2}}{\left| \dfrac{\partial \vec{r}}{\partial s} \right|^3} \ln\left(\frac{1}{\varepsilon}\right) \frac{\Gamma}{4\pi} \qquad (5\text{-}24)$$

where

$\vec{r}$ = the position vector of a point on the vortex filament s, and

ε = effective core radius

For a continuous filament, both $\frac{\partial \vec{r}}{\partial s}$ and $\frac{\partial^2 \vec{r}}{\partial s^2}$ can be determined immediately. For the numerical problem with the vortex filaments being approximated by a finite number of points, it is possible to express the derivatives at a field point in terms of the location of the field point and the locations of adjacent points on either side. If $\vec{r}$ is the position vector of the vortex filament with $\vec{r}_A$, $\vec{r}_B$, $\vec{r}_C$ the locations of three adjacent points in the positive direction of the filament, $d\vec{s}$, then using a Taylor series expansion about B yields

$$\vec{r}_C = \vec{r}_B + \left.\frac{\partial \vec{r}}{\partial s}\right|_{\vec{r}_B} \Delta s_2 + \left.\frac{\partial^2 \vec{r}}{\partial s^2}\right|_{\vec{r}_B} \frac{(\Delta s_2)^2}{2} \tag{5-25}$$

likewise

$$\vec{r}_A = \vec{r}_B + \left.\frac{\partial \vec{r}}{\partial s}\right|_{\vec{r}_B} \Delta s_1 + \left.\frac{\partial^2 \vec{r}}{\partial s^2}\right|_{\vec{r}_B} \frac{(\Delta s_1)^2}{2} \tag{5-26}$$

where

$$\Delta s_1 = \vec{r}_A - \vec{r}_B$$

$$\Delta s_2 = \vec{r}_B - \vec{r}_C$$

The necessary derivatives at x can now be calculated from equations (5-25) and (5-26) as

$$\left.\frac{\partial \vec{r}}{\partial s}\right|_{\vec{r}_B} = \frac{\Delta s_1}{\Delta s_2}\,\frac{\vec{r}_C-\vec{r}_B}{\Delta s_1+\Delta s_2} - \frac{\Delta s_2}{\Delta s_1}\,\frac{\vec{r}_A-\vec{r}_B}{\Delta s_1+\Delta s_2} \tag{5-27}$$

and

$$\left.\frac{\partial^2 \vec{r}}{\partial s^2}\right|_{\vec{r}_B} = \frac{1}{\frac{(\Delta s_1+\Delta s_2)}{2}}\,\frac{\vec{r}_C-\vec{r}_B}{\Delta s_2} + \frac{\vec{r}_A-\vec{r}_B}{\Delta s_1} \tag{5-28}$$

For numerical computations, equations (5-27) and (5-28) are rewritten in terms of Cartesian coordinates of the three point element as

$$\frac{\partial \vec{r}}{\partial s} = \frac{1}{\Delta s_1+\Delta s_2}\left[\frac{\Delta s_1}{\Delta s_2}(x_C-x_B) - \frac{\Delta s_2}{\Delta s_1}(x_A-x_B)\right]\hat{i} +$$

$$\left[\frac{\Delta s_1}{\Delta s2}(y_C-y_B) - \frac{\Delta s_2}{\Delta s_2}(y_A-y_B)\right]\hat{j} +$$

$$\left[\frac{\Delta s_1}{\Delta s_2}(z_C-z_B) - \frac{\Delta s_2}{\Delta s_1}(z_A-z_B)\right]\hat{k} \tag{5-29}$$

and

$$\frac{\partial^2 \vec{r}}{\partial s^2} = \frac{1}{\frac{\Delta s_1+\Delta s_2}{2}} \left[\frac{x_C-x_B}{\Delta s_2} + \frac{x_A-x_B}{\Delta s_1}\right]\hat{i} +$$

$$\left[\frac{y_C-y_B}{\Delta s_2} + \frac{y_A-y_B}{\Delta s_1}\right]\hat{i} +$$

$$\left[\frac{z_C-z_B}{\Delta s_2} + \frac{z_A-z_B}{\Delta s_1}\right]\hat{k} \tag{5-30}$$

These results can now be employed in equation (5-24) to obtain the self induced velocity at point B as

$$q_{ix} = \frac{\Gamma}{2\pi\Delta s_1\Delta s_2} \frac{1}{\left|\frac{\partial \vec{r}}{\partial s}\right|^3} [(y_C-y_B)(z_A-z_B)-(y_A-y_B)(z_C-z_B)$$

where

(5-31)

$$\left|\frac{\partial \vec{r}}{\partial s}\right|^3 = \{\frac{1}{(\Delta s_1+\Delta s_2)} (\Delta s_1)^2+(\Delta s_2)^2-2[(X_C-X_B)(X_A-X_B)$$

$$+ (y_C-y_B)(y_A-y_B)+(z_C-z_B)(z_A-z_B)]\}$$

Similar equations can be obtained for q_{iy} and q_{iz}.

5.2.6 Numerical Procedure

The numerical procedure begins with an assumed wake geometry and circulation distribution. A first "guess" is generated using spanwise momentum theory [45]. A second "guess" is obtained using a non-expanding wake analysis. The wake is assumed to consist of helical vortices trailing from the blade. The helical path of a trailing vortex filament is approximated by a series of points connected by straight lines. The pitch of the helix and the convective velocity of the wake are assumed to be the local values of corresponding parameters at the trailing edge. The radial flow is neglected, however, the distribution of axial component of disturbance velocity is found using an iterative method. Results of this analysis form the initial values of parameters for the loop on wake deformation and distortion.

A deformed wake geometry is computed employing an iterative method. The initial values of wake displacement are calculated using the non-rigid wake induced flow field. A new wake geometry and its corresponding induced flow field are then calculated. The wake geometry is updated and calculations are repeated until a consistent wake geometry-induced flow is established.

The last phase of computations consists of calculations of the blade forces and performance. This procedure is similar to that of section 3.6.

5.2.7 Airfoil Characteristics

The inviscid flow assumption greatly reduces the complexity of fluid flow. Principles and theorems of the inviscid flow theory can be used to obtain lift of an airfoil in a flow field. Although this theory yields results that are, in many cases, compatible with experimental data, it fails to provide accurate information about the flow field close to the solid boundaries. Nevertheless, this deficiency does not reduce the importance of inviscid flow condiderations.

To account for the real fluid effects such as drag and boundary layer separation, the airfoil characteristics data is used in conjunction with the inviscid flow theory. In this fashion, the analysis benefits from the great simplifications in the equations of motion and at the same time corrects for the real fluid effects using a relatively simple model. Airfoil data is well documented in Ref. [46] for a wide range of airfoils and for angles of attack up to the stall angle. The experimental data beyond this angle is scarce and uncertain. This presents a major impediment to accurate prediction of wind turbine performance since a considerable portion of a blade operates in this region during normal operation. In the present analysis the turbulent airfoil data obtained for symmetric airfoils, [47], has been used.

Chapter VI

RESULTS AND DISCUSSIONS

Before preceeding to the numerical results for the various wind turbines studied, a few comments are in order regarding verification of the methods of analysis. Numerical modeling of a physical phenomenon should be properly verified before its application can be justified. This verification, in general, can be accomplished by comparison to limiting cases or to analytical solutions. If such solutions are not available, which is the case for wind turbines, the numerical results are compared to pertinent experimental data. However, such experimental data for a wind turbine are scarce and what is available mainly concerns generator power versus wind speed. This implies that only the integrated performance may be compared and, regrettably, many important details of the computational method cannot be verified. In addition, the generated power reported in the literature has considerable scatter because of local wind characteristics. Consequently it was decided to follow two courses for verification purposes: one is to compare numerical results of the present analysis to that of other numerical techniques, and the other is to compare the integrated performance to the available experimental data. This is undesirable, however, because in either case the comparisons are not quite conclusive. For the numerical comparison, for example, in cases of disagreement it is not always clear which method is correct. For the case of correlations with the experimental data, presence of experimental data scatter makes any definite conclusion very difficult, if not impossible. Nonetheless, due to the lack of other means of verification, this approach is taken in this thesis for evaluation and verification of the proposed numerical models.

Performance parameters calculated herein will be compared with values obtained via three other methods of analysis: the blade element-momentum analysis used in the PROP code, [16], the rigid helical vortex wake analysis, [44], and the free-wake analysis used in the MIT vortex code, [7]. The PROP code is probably the simplest whereas the MIT code is the most complex in the literature on wind turbines. In the MIT code the unconstrained wake is permitted to move freely with the local velocities existing in the wake. Because of this, the MIT model may be considered the most complete and accurate model available.

Comparison of results of the present analysis with existing experimental data will be done for three rotor configurations. The experimental data pertaining to these wind turbines are contained in [52].

The computational procedures described in chapter 5 were performed for a number of two bladed rotors. Tables 6-1 to 6-4 present operating conditions and geometric data for the rotors considered. The conditions are numbered for convenient reference in the text. The numerical results for the non-dimensional circulation distribution, the dimensionless axial induced velocity distribution, and the effective angle of attack distribution along the blade span are compared to the data provided in

Table 6-1 Blade Geometry and Opearting Conditions for Numerical Comparisons

Case	Solidity $\frac{Nc}{\pi R}$	Speed Ratio $\frac{R\Omega}{V_0}$	Pitch Angle Degree	Chord Distribution
1	.106	9.524	2	constant
2	.106	6.500	0	constant
3	.106	6.50	2	constant
4	.106	6.500	4	constant

Table 6-2 Blade geometry and Opearting Condition of MOD-0A for Experimental Comparisons (Case 5)

Blade radius = 19.05 m

RPM = 40

% Blade radius	twist (degree)	chord (m)	thickness to chord ratio
6.4	31.7	1.372	.335
18.1	20.16	1.372	.306
29.8	11.3	1.311	.278
41.5	7.1	1.164	.248
53.2	3.49	1.02	.220
64.9	1.62	.881	.191
76.6	.13	.74	.162
88.3	-1.06	.619	.133
100.	-2.0	.460	.105

Table 6-3 Blade geometry and Opearting Condition of MOD-OA for Experimental Comparisons (Case 6)

Blade radius = 19.05 m

RPM = 40

% Blade radius	twist (degree)	chord (m)	thickness to chord ratio
22.4	4.2	1.58	.295
32.	3.43	1.44	.269
41.8	2.65	1.345	.243
51.5	1.87	1.228	.218
61.2	1.10	1.11	.192
70.9	.33	.994	.166
80.6	-.45	.875	.140
90.3	-1.23	.759	.115
100.	-2.0	.64	.090

Table 6-4 Blade geometry and Opearting Condition of MOD-OA for Experimental Comparisons (Case 7)

Blade radius = 19.05 m

RPM = 40

% Blade radius	twist (degree)	chord (m)	thickness to chord ratio
31.6	0	1.52	.28
37.3	0	1.52	.275
83.	0	1.42	.233
88.6	0	1.27	.227
94.3	0	1.22	.22
100.	0	1.17	.217

Reference [7]. Finally, the calculated power is compared with the experimental data of [52].

6.1 Airfoil Data

The aerodynamic performance parameters predicted in any analysis exploying Prandtl's hypothesis (blade element theory) depends to a large extent on the airfoil data supplied. This data is required to provide a known relationship between the effective angle of attack, at a given section, and the lift coefficient being developed by the section. This data is generally obtained from wind tunnel tests on two-dimensional scale models of the airfoil which are used to represent the actual or real nature of the flow field. To be sure, high accuracy data obtained under conditions that closely approximate the real flow conditions is necessary for reliable computational results. Solutions to the governing equations developed in Chapter 5 are simply not possible without this data. The airfoil characteristics used in the computations for numerical comparisons are presented in Figs. 6-1 and 6-2. This particular airfoil data was employed because it is consistent with that used in Reference [7]. For other cases, where comparisons are made to experimental data, realistic wind tunnel data is employed. Prior research on wind turbine performance [44] has shown that wind turbines occasionally operate at angles of attack far beyond the stall angle. Therefore, the airfoil data over a wide range of angles of attack is required. Pre-stall airfoil characteristics are well established. The data provided in Reference [50], which contains such data for a variety of airfoils, were used. The

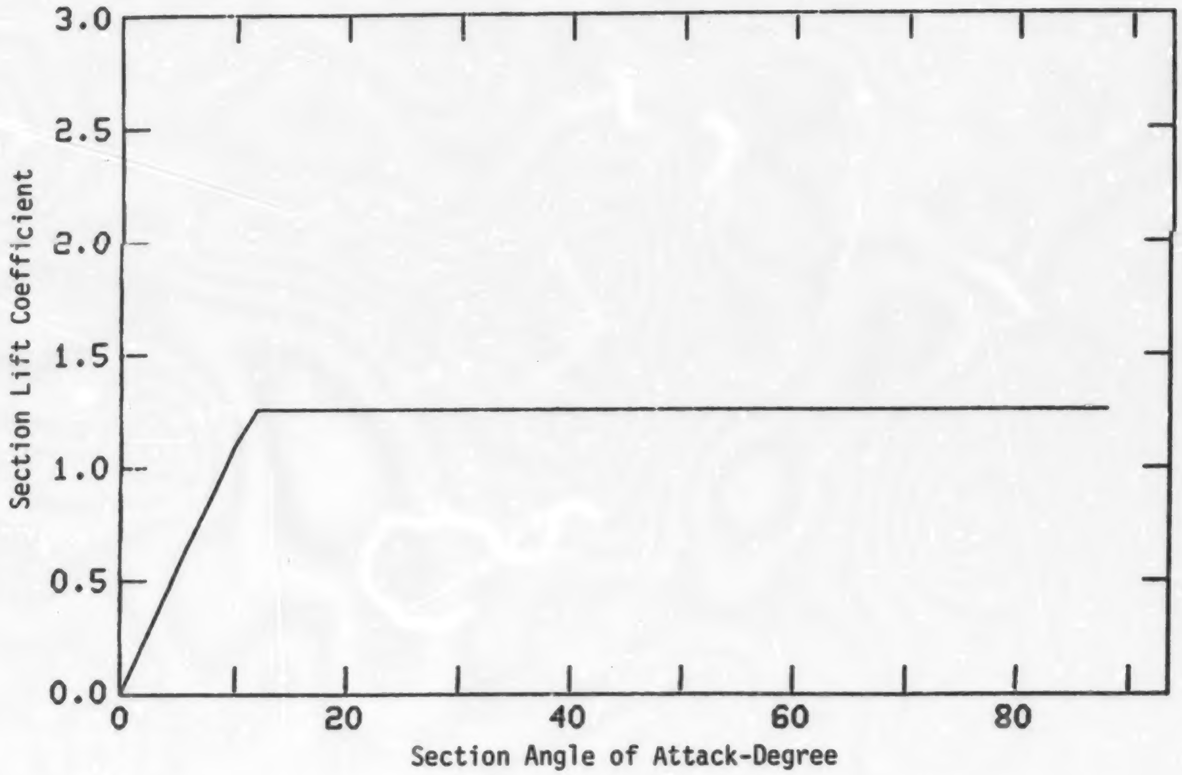

Fig. 6-1 Idealized section lift coefficient vs. section angle of attack (cases 1 to 4).

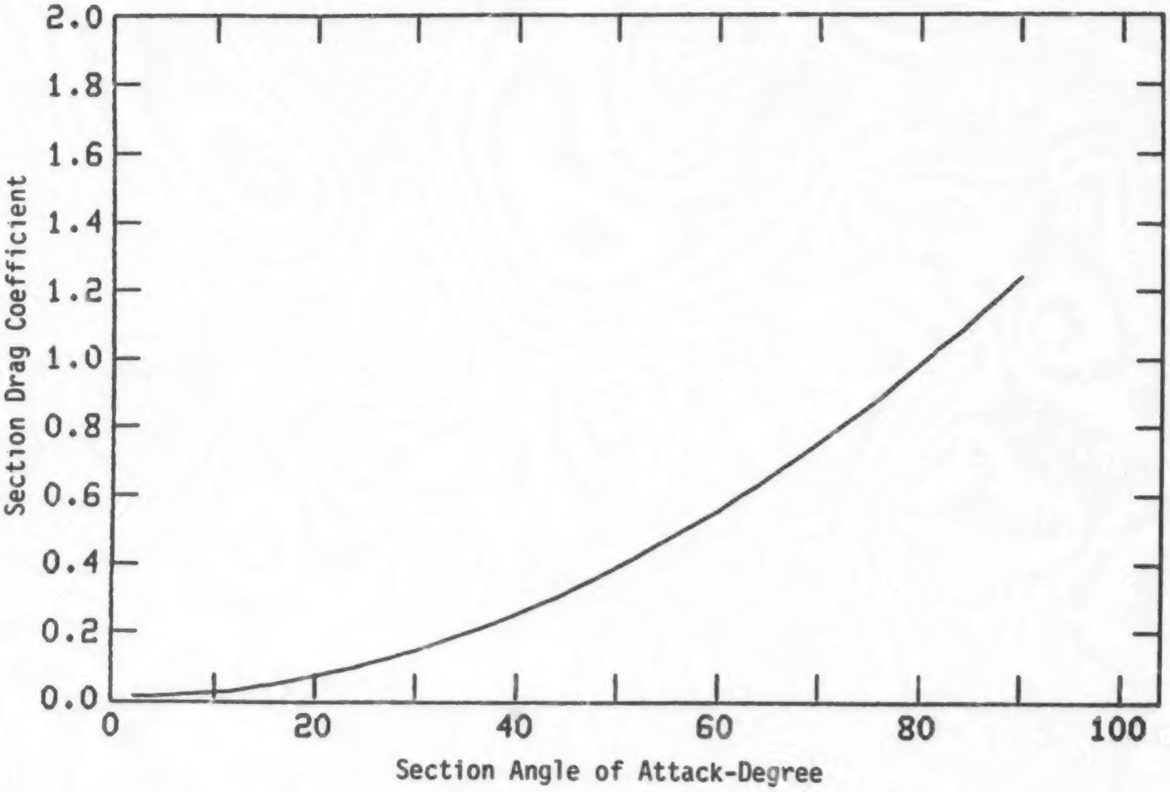

Fig. 6-2 Idealized section drag coefficient vs. section angle of attack (cases 1 to 4).

post-stall data, on the other hand, is not abundant. The airfoil data for several symmetric airfoil sections over a wide range of angles of attack are gathered in [47]. Sample airfoil data used in this report is shown graphically in Figs. 6-3 and 6-4.

When utilizing two-dimensional airfoil data, it should be noted that there are second order effects that strongly influence airfoil performance. The most important of these effects are: the thickness to chord ratio, and the section Reynolds number. This influence, however, is primarily limited to the pre-stall region. In that region, the lift coefficient is proportional to the section Reynolds number and inversely proportional to the thickness to chord ratio. The airfoil data is corrected for the section thickness to chord ratio by interpolating (or extrapolating) the experimentally obtained airfoil characteristics of two airfoil sections with different thickness to chord ratios. A sample of such data is provided in Table 6-5. No Reynolds number correction for viscous effects were included. However, such corrections can be easily incorporated by suitably modifiying the supplied airfoil data. One final remark on use of proper airfoil data is offered. It is important to realize that the surface roughness plays an important role in the boundary layer development of any airfoil. Therefore, degradation of the airfoil surface can cause a corresponding degradation in airfoil performance. This effect is difficult to quantify as it is unpredictable. Hence, when utilizing laminar airfoil sections, use of experimentally obtained data for smooth airfoil surfaces could lead to very optimistic predicted performance.

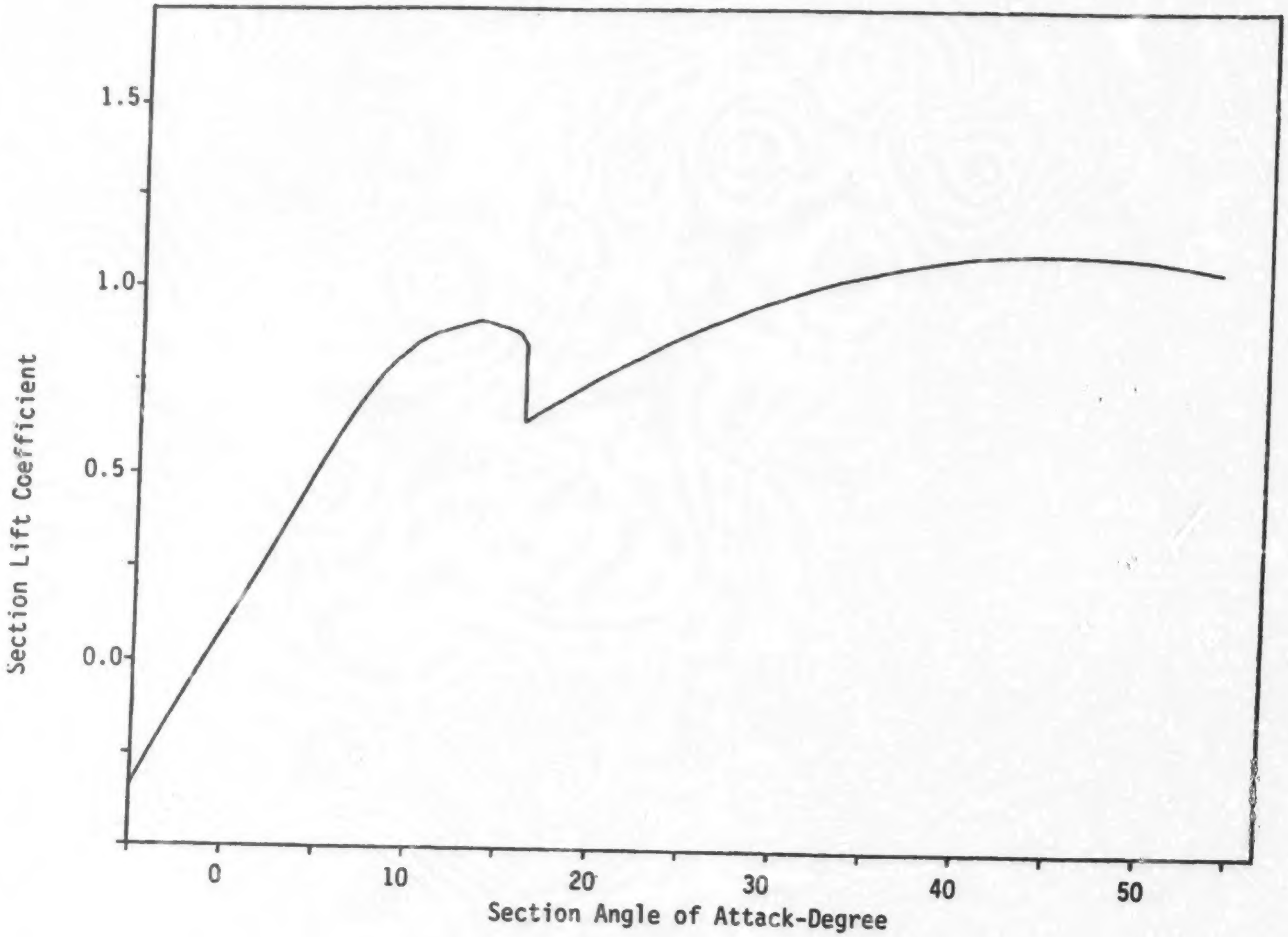

Fig. 6-3 Section lift coefficient vs. section angle of attack for NACA 23024 airfoil

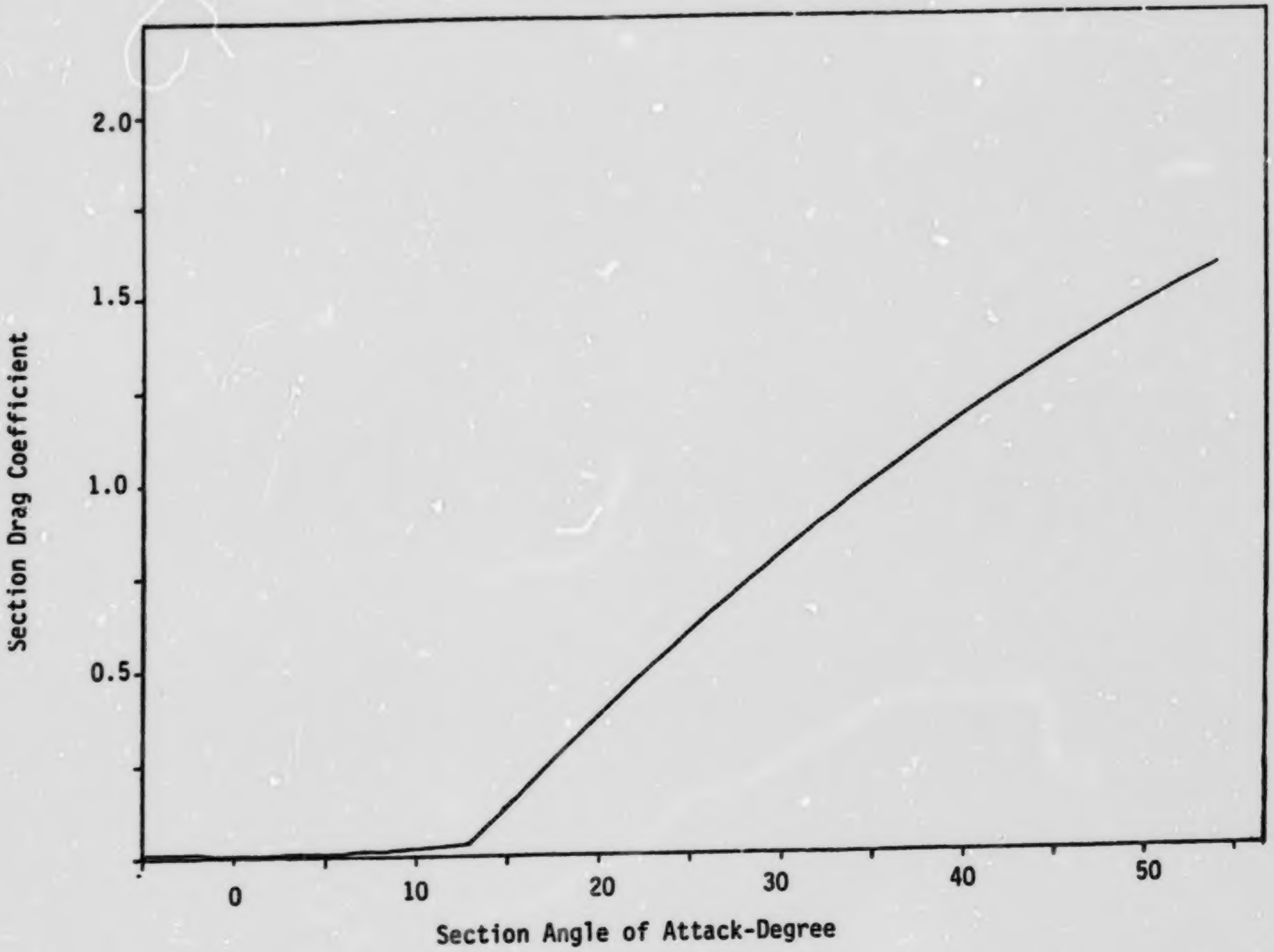

Fig. 6-4 Section drag coefficient vs. section angle of attack for NACA 23024 airfoil

Table 6-5 Lift and Drag coefficient Data for Selected NACA 23000 Airfoil Series at Re = 3,000,000

NACA AIrfoil Number	23024		23018	
Effective Angle of Attack (Degrees)	C_L	C_D	C_L	C_D
-10	-0.772	0.013	-0.882	0.012
- 5	-0.341	0.009	-0.391	0.008
0	0.108	0.008	0.124	0.007
5	0.557	0.011	0.638	0.009
10	0.977	0.016	1.118	0.014
15	1.167	0.034	1.401	0.021
20	1.000	0.123	1.000	0.109
25	1.074	0.230	1.074	0.223
30	1.128	0.490	1.128	0.457
35	1.160	0.731	1.160	0.704
40	1.167	0.952	1.167	0.929
45	1.148	1.151	1.148	1.132
50	1.102	1.329	1.102	1.314
55	1.029	1.486	1.029	1.475
60	0.932	1.623	0.932	1.615
65	0.812	1.738	0.812	1.732
70	0.672	1.832	0.672	1.829
75	0.517	1.906	0.517	1.904
80	0.350	1.953	0.350	1.957
85	0.176	1.990	0.176	1.989
90	0.001	2.000	0.001	2.000

6.2 Circulation Distribution

The non-dimensional circulation distribution ($\frac{\Gamma}{\Omega R^2}$) along the blade for four operating conditions (cases 1 to 4) are compared to those of [7]. Figures 6-5 to 6-8 show the results for the fast free wake analysis (FFW). At the root section of the blade in the inboard region, the vortex strengths are found to be slightly smaller than those predicted in Reference [7]. By contrast, in the outboard region the values of circulation become slightly larger but they drop at a faster rate to zero at the blade tip. The results for the simplified free wake analysis (SFW) are presented in Figs. 6-9 to 6-12. It is seen that the computed results are in better agreement with those of [7] than are the FFW results. Further, it is noted that the SFW results show a similar trend in the inboard region but as the blade tip is approached the decrease in the vortex strength is not sharp and the values of circulation remain slightly higher over the entire outboard region. The differences are attributed to the different modeling of the outboard trailing sheet. In the SFW model the outboard trailing vortex sheet is assumed to roll-up into an intense tip vortex. Moreover, only a low number of trailing vortex filaments were considered since the wake geometry calculations take an appreciably long time. It should be remembered that the continous vorticity of the sheet is approximated by sheet filaments that have concentrated vorticity. If the number of the filaments is increased the intensity and the location of the peaks may be altered. This is believed to improved the results of the SFW model in the blade tip region. Furthermore, since the disgreement is very small, and since the MIT model may not represent the real flow field, no further study of this discrepancy was attempted. It is remarked, however, that since circulation peaks in these studies were found to be small, they do not affect the wake geometry calculations appreciably. Consequently, the discrepancies in the predicted performance due to a low number of vortex filaments in the outboard trailing vortex sheet should be insignificant. A rotor with a large number of blades is likely to show larger peaks in circulation distribution, [53]. Hence more nodes should be used to obtain satisfactory results for such rotors.

The analogous results of the strip theory of [54] are included in Figs. 6-17 to 6-20. The computed values were obtained using a method similar to that developed in [16]. The computation procedure of [54] is usually referred to as the WIND II code in the literature. It is shown that the circulation distribution is appreciably smaller than those of the MIT code for all cases considered. This appears to be due to the inherent assumptions of an infinite number of blades and unidirectional flow employed in blade element-momentum theories. In general both axial and radial components of the induced velocity are considerably underpredicted and this, in turn, leads to the discrepancey in the calculated loading and performance. It may be concluded that the use of the strip theory of [54] and similar theories could lead to underprediction of the loading on the blade.

6.3 Axial Induced Velocity Distribution

The spanwise axial induced velocity distributions for cases 1 to 4 are plotted against the nondimensional radius in Figs. 6-21 through

6-36. For the FFW model a particular trend is noted. The predicted induced velocities in the tip region agree well with those of MIT model. However, the agreement becomes progressively worse as the root section is approached. The corresponding values of the SFW model are illustrated in Figs. 6-25 to 6-28. It is seen that the SFW results are slightly lower than those of MIT model. In addition, it is noted that the FFW model shows better agreement than does the SFW model. This is consistent with the results obtained for the circulation distribution. The FFW model predicts higher circulation peaks than the SFW model. The influence of outboard vortex filaments is thus larger for the FFW model and consequently a larger induced flow is developed. The outboard trailing wake geometry could also be in part responsible for the discrepancy. The SFW model assumes that the trailing vortex sheet has a negligible effect on the very near wake. By contrast, for the conditions studied, the free-stream velocity may not be strong enough to carry the tip vortex quickly downstream of the rotor; thus the effect of tip vortex on the very near wake may be significant. The axial induced velocity distribution for the strip theory of [54] are depicted in Figs. 6-33 to 6-36. These results show no regular trend and no conclusion about the accuracy of the method can be made.

6.4 Effective Angle of Attack Distribution

Plots of the effective angle of attack distribution for different operating conditions are provided in Figs. 6-37 to 6-52. It should be recalled that the effective angle of attack distribution along the blade is closely related to the circulation distribution. The degree of dissimilarity between the distribution of the effective angle of attack, α_e, and the distribution of circulation, Γ, is due, of course, to the variation of the lift coefficient against the effective angle of attack (since there is no variation of chord along the span). The drastic changes in the plot of the α_e distribution along the blade are due to the discontinuity of the slope of the lift curve at the stall angle, Fig. 6-1.

In order to present the relative differences in results of the methods of wind turbine performance prediction presented in Figs. 6-5 to 6-52, a sample plot is provided. This plot, shown in Fig. 6-53, contains the computed circulation distribution along the blade span for the blade span for the blade and operating condition of case 4.

6.5 Power and Thrust Coefficient Comparisons

The total integrated power and thrust coefficients calculated by different methods of analysis are contained in Table 6-6. It is shown that the results of the simplified free wake analysis agree well with those of the MIT Code except for Case 1. This is attributed to the possible improper determination of the location of maximum circulation distribution. For this case the wind velocity is low, hence, wake vortices remain in the vicinity of the rotor plane thereby greatly influencing the rotor induced flow. Consequently a larger number of computation nodes on the blade (therefore trailing vortices) is required to represent the wake sheet more accurately. This is believed to improve the results of the simplified free wake model for this case. The fast free wake results, on the other hand, show the best agreement at high tip speed ratios indicating that the wake model represents such flow conditions more closely. The results of the rigid wake theory becomes progressively worse for high tip speed ratios as expected. The momentum-blade element theory shows a significant underprediction of both power and axial force (thrust) coefficients.

6.6 Comparisons With Experimental Data

The total integrated performance of three rotor configurations with varying twist distribution and chord distribution (cases 5 to 7) were investigated to verify the application of the present methods to more complicated planform geometries. Primarily, however, calculations for these rotors served as a general check on the accuracy of the flow models developed in this thesis. The experimental work was performed on a 200 kW wind turbine at the Plum Brook station in Sandusky, Ohio. All pertinent calculations in this report were performed for rotor geometries and operating conditions of the experimental data. As illustrated in Figs. 6-54 to 6-59, the computed performance for both models indicates that the total integrated generated power is predicted very closely to the midpoint of the experimental data. As expected, however, the agreement is not as good for low wind velocities. This is due to the fact that under these conditions the tip vortex of the preceding blade remains close to the rotor plane thereby effecting the elements in the blade tip region appreciably. The lifing line assumption is no longer valid for the sections close to the blade tip under these operating conditions since large variations occur in the chordwise pressure distribution. Too, the blade element theory loses its validity in the tip region since interference effects are significant. Once more, however, it is remarked that no definite conclusion about the relative accuracy of either methods can be made due to the considerable scatter in the experimental data. The curve for experimental data flattens out at the rated power as a result of the automatic tip control system employed. This is done by suitably changing the section pitch angle via a computer assisted control system. The power output of the alternator is monitored by this computer and the pitch is decreased so as to maintain the alternator power constant at the rated value.

6.7 Results of the Prescribed Wake Analysis

As mentioned earlier, due to lack of detailed experimental data on the wake of wind turbines, the prescribed wake analysis in this report has a qualitative value. However, the computer code developed based on the method of chapter four is readily applicable to the analysis of wind turbine airload parameters and performance once the necessary information on the wake geometry is supplied.

A set of parametric runs were made in order to study the performance of a wind turbine for different expansion rates. The wake expansion rates were defined arbitrarily by prescribing the location of the "half expansion" of the wake behind the rotor plane. This information was used to completely define the exponential representation of the wake discussed in chapter four. For half expansion

$$R(z) = \frac{R_2 + R}{2}$$

$$= R_2 - (R_2 - R) \exp [- \frac{az}{R_2 - R}]$$

or

$$\exp [- \frac{az}{R_2 - R}] = \frac{1}{2}$$

thus

$$a = \frac{(R_2 - R) \ln(1/2)}{z}$$

For a given z a value of "a" is calculated from the above equation. The exponential slipstream expansion is then used to calculate the wake geometry and performance. Figure 6-60 illustrates the results. It can be seen that the power coefficient, the ratio of absorbed power to the available power in the wind, increase as the expansion rates are increased. However, due to the arbitrary nature of the expansion rates assigned, unrealistic powers are calculated. Nevertheless, the possibility of generating more power than predicted by rigid wake analyses are clearly noted. This excess power is, of course, generated when wake expansion is significant, that is, at low wind velocity conditions.

6.8 Computed Wake Geometry

In principle, the computed wake geometry can be presented graphically by means of computer graphics techniques. Details of the geometry can be best seen by obtaining the projections of the geometry on three planes in a Cartesian coordinate system. This task, however, was not accomplished in this thesis and is recommended as an extension to the present work. As a sample graph, however, a trace of the computed geometry of one tip vortex for the data of Case 4 is presented in Fig. 6-61.

6.9 Computer Time

All calculations reported in this thesis were done on a NAS 6650 computer system. The computer time for a typical two-bladed wind turbine ranged from about 27 seconds for the prescribed wake method to 2.5 minutes for the SFW model. The FFW model required about 30 seconds for each run. For the SFW model, about 70 to 80 percent of the required CPU time is used in the vortex sheet geometry calculations. Some reduction in the computer time could have been achieved by eliminating the inboard far wake calculations. It is anticipated that the CPU time will increase proportionally to the number of blades for a rotor with more than two blades.

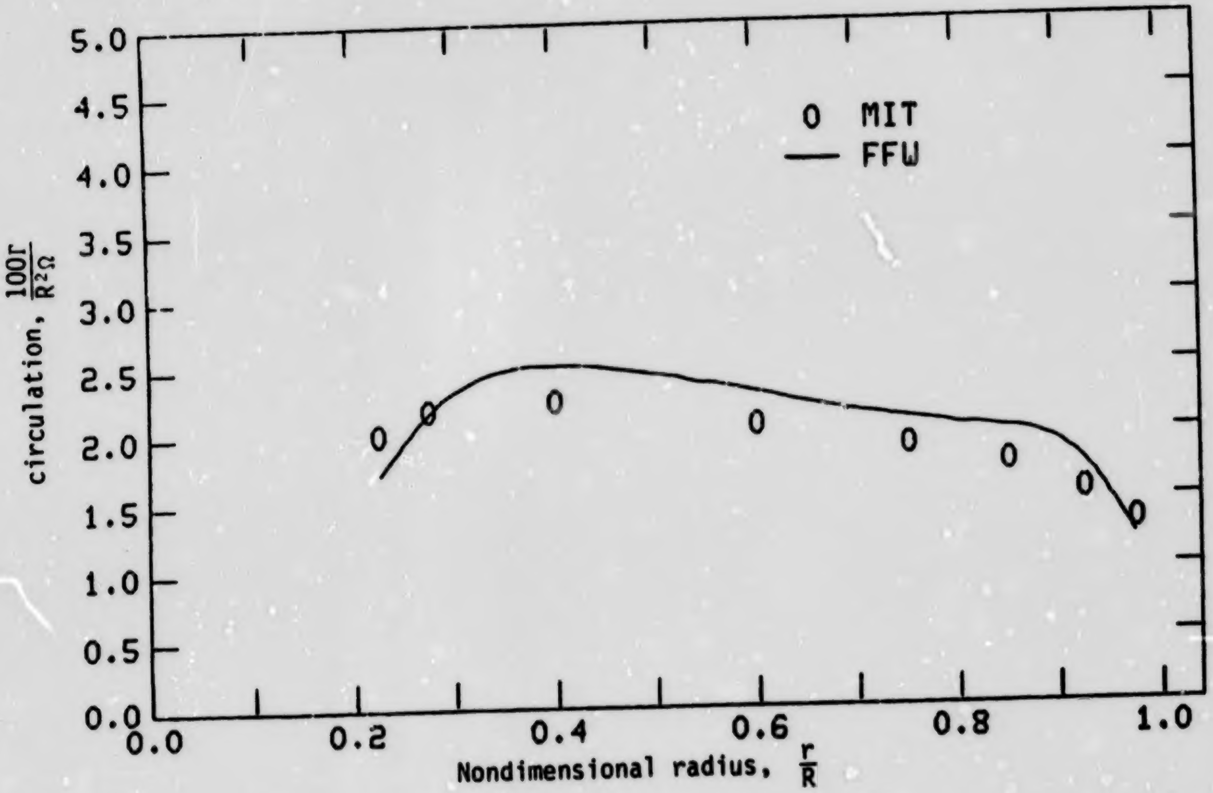

Fig. 6-5 Comparison of fast free wake (FFW) dimensionless circulation along the blade with existing MIT [7] data (case 1).

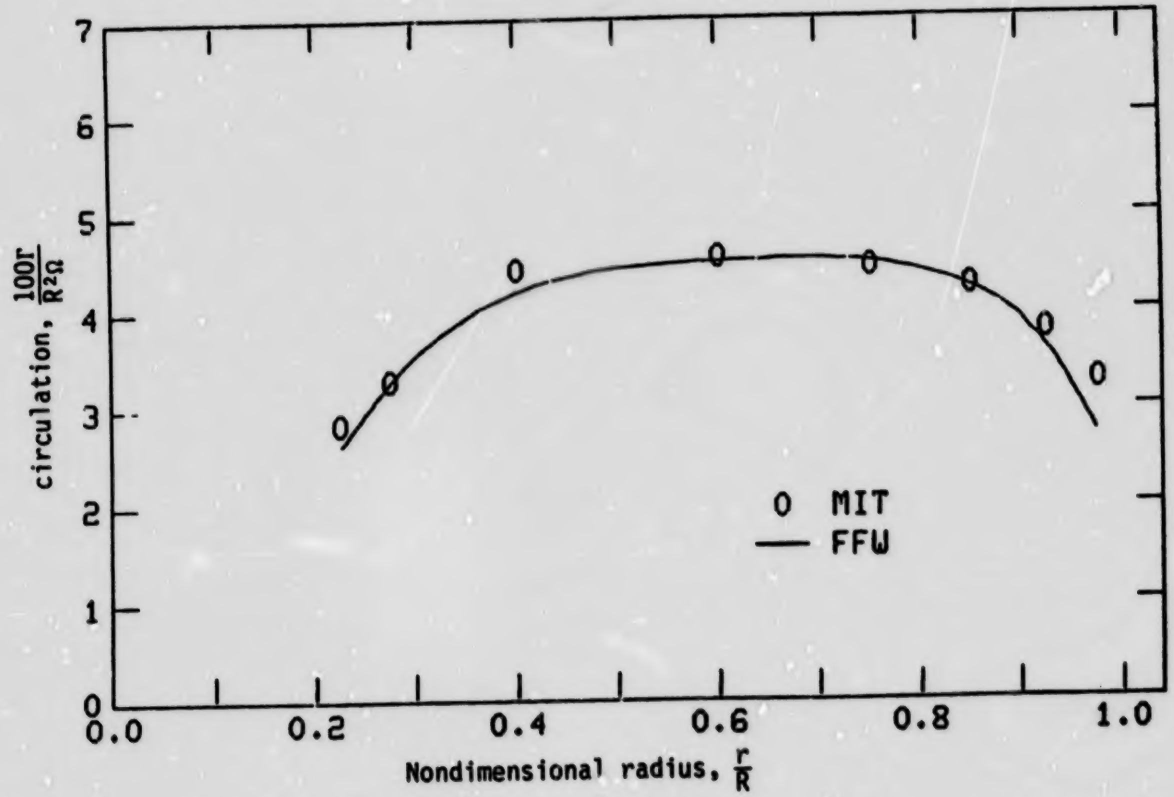

Fig. 6-6 Comparison of fast free wake (FFW) dimensionless circulation along the blade with existing MIT [7] data (case 2).

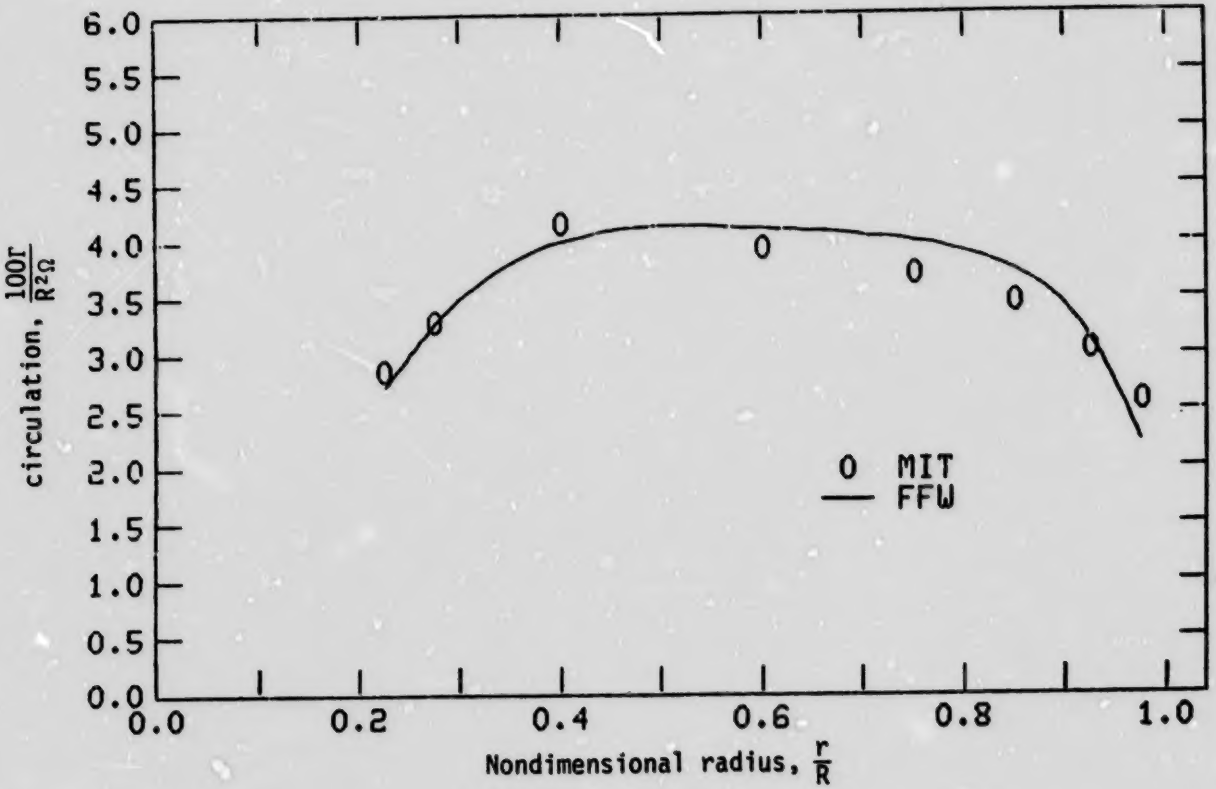

Fig. 6-7 Comparison of fast free wake (FFW) dimensionless circulation along the blade with existing MIT [7] date (case 3).

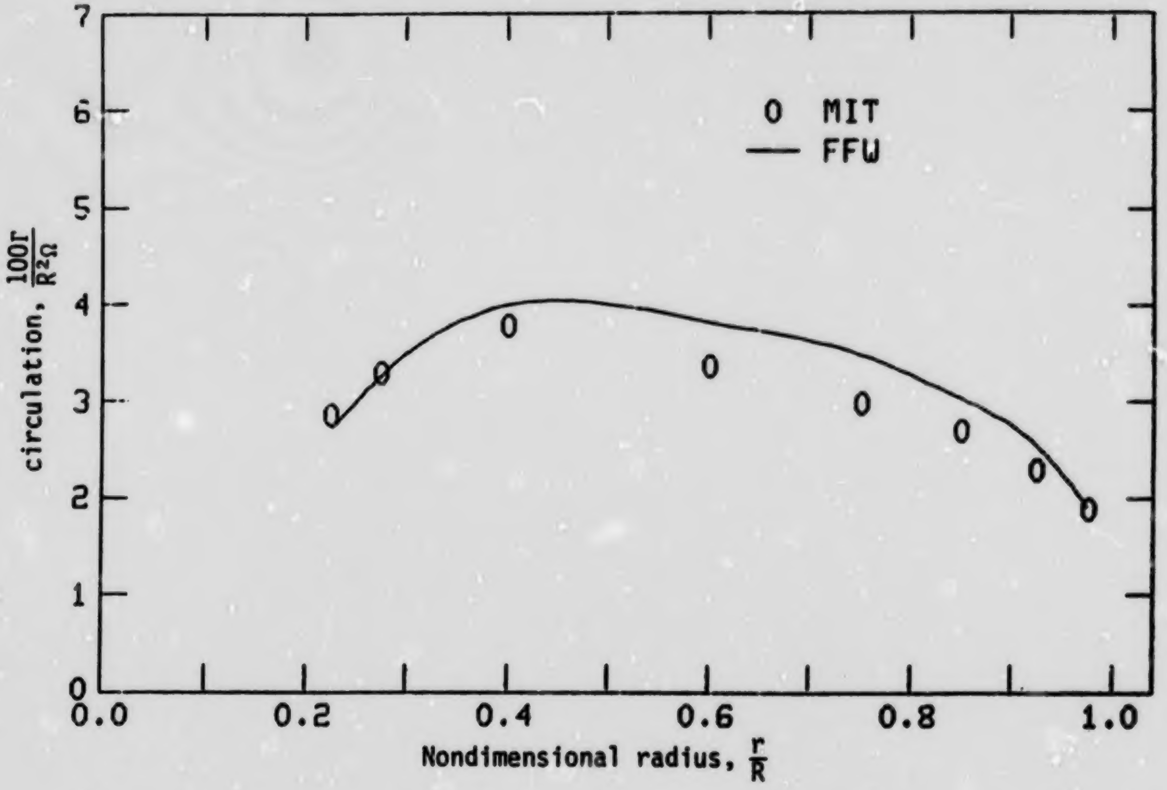

Fig. 6-8 Comparison of fast free wake (FFW) dimensionless circulation along the blade with existing MIT [7] data (case 4).

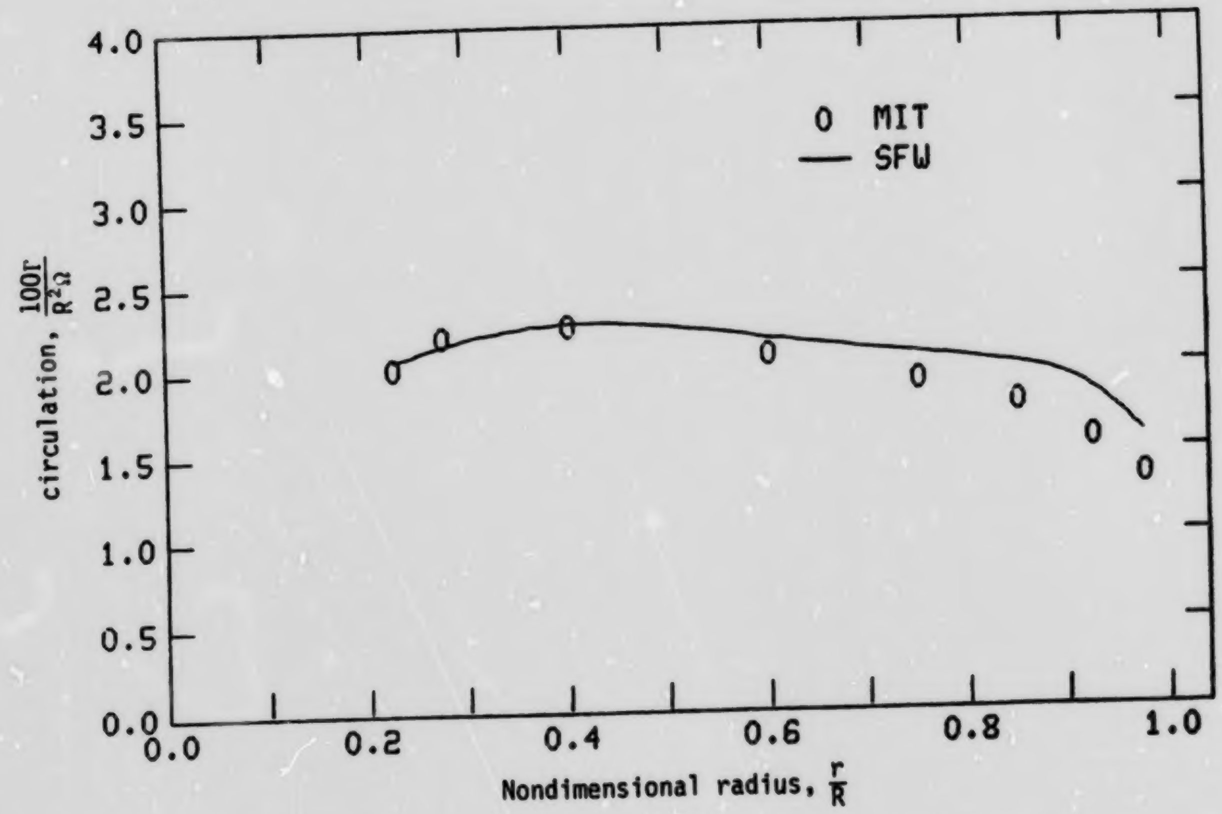

Fig. 6-9 Comparison of simplified free wake (SFW) dimensionless circulation distribution along the blade with existing MIT [7] data (case 1).

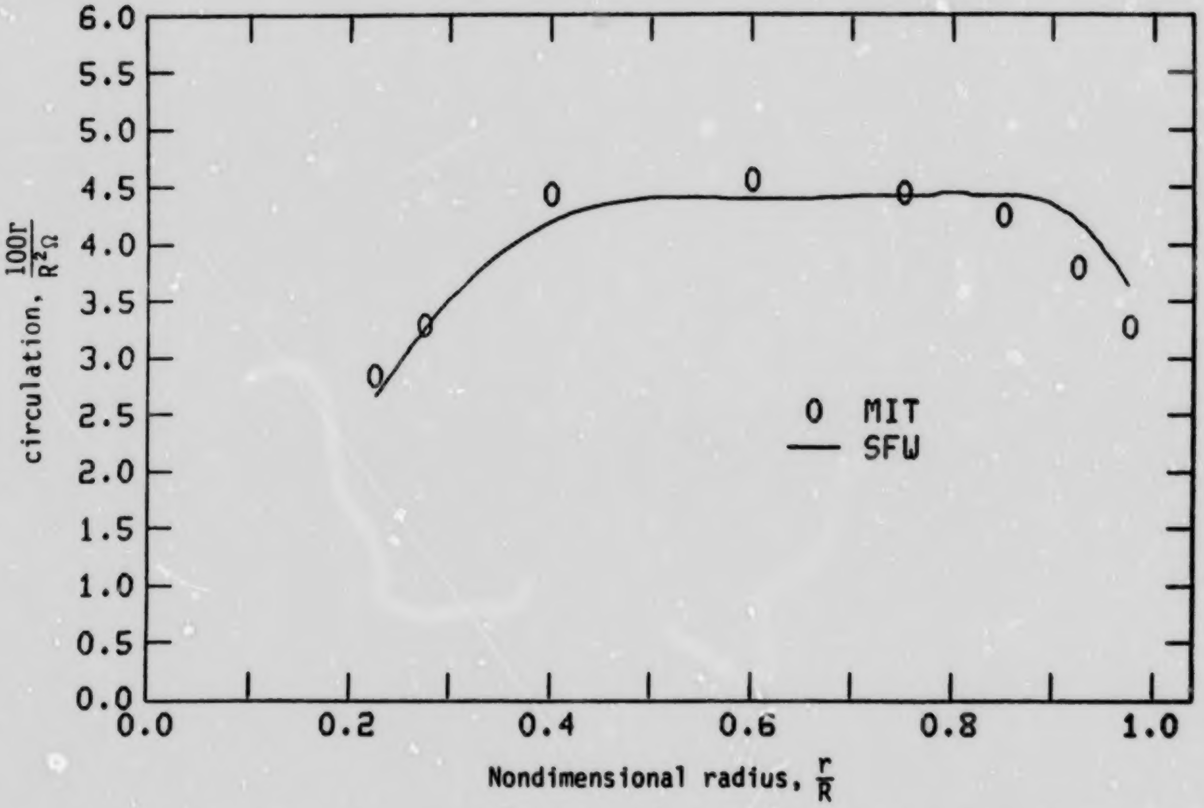

Fig. 6-10 Comparison of simplified free wake (SFW) dimensionless circulation distribution along the blade with existing MIT [7] data (case 2).

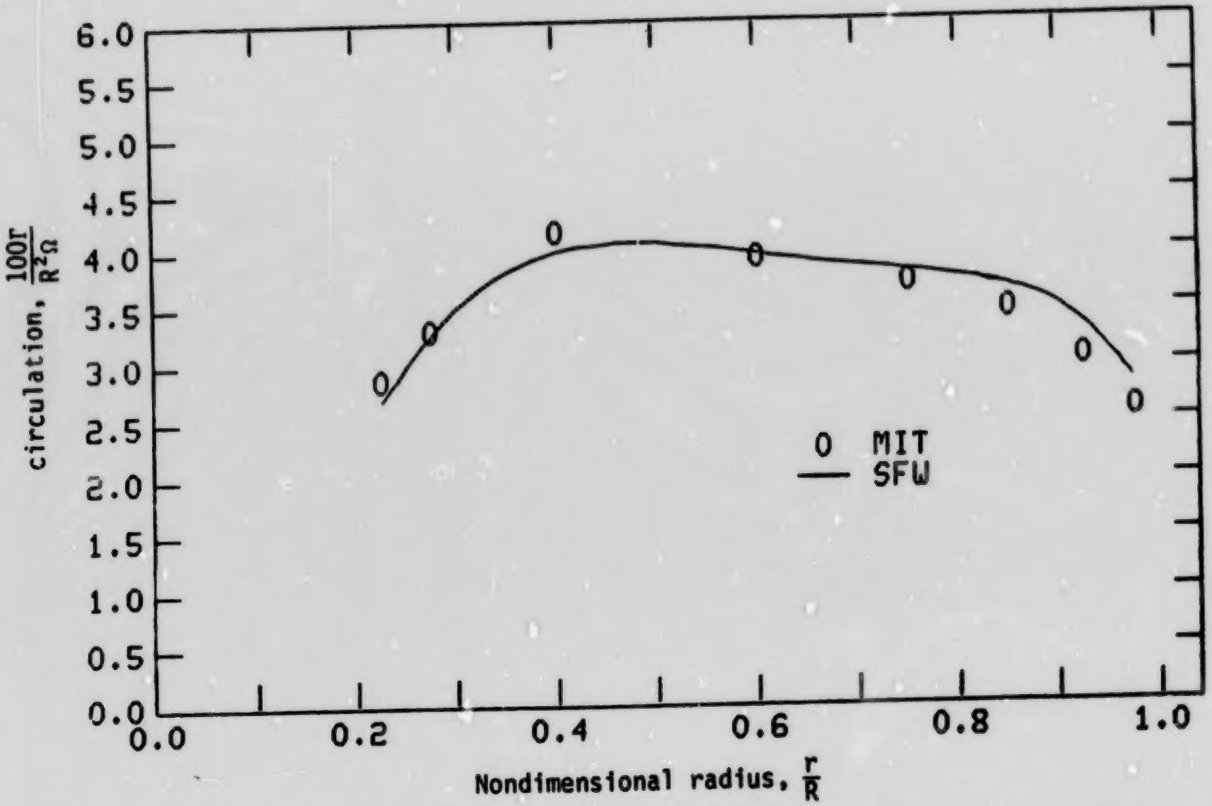

Fig. 6-11 Comparison of simplified free wake (SFW) dimensionless circulation distribution along the blade with existing MIT [7] data (case 3).

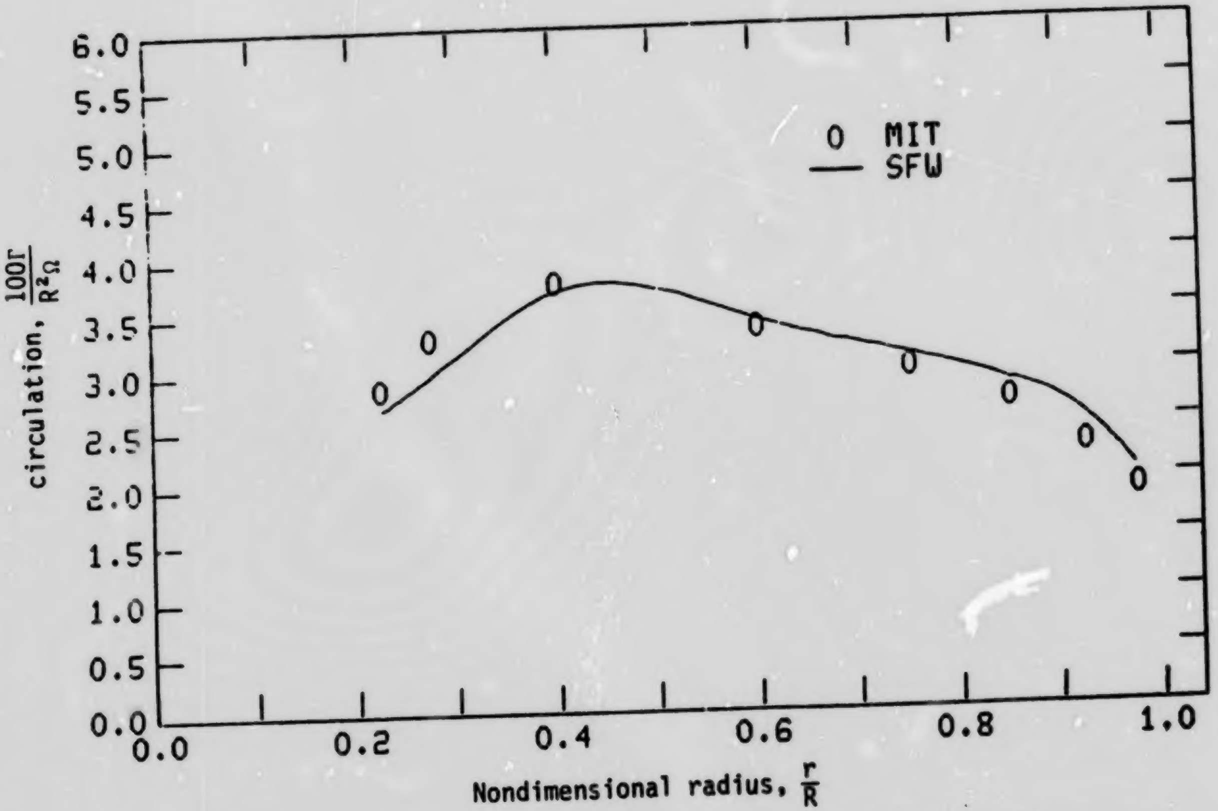

Fig. 6-12 Comparison of simplified free wake (SFW) dimensionless circulation distribution along the blade with existing MIT [7] data (case 4).

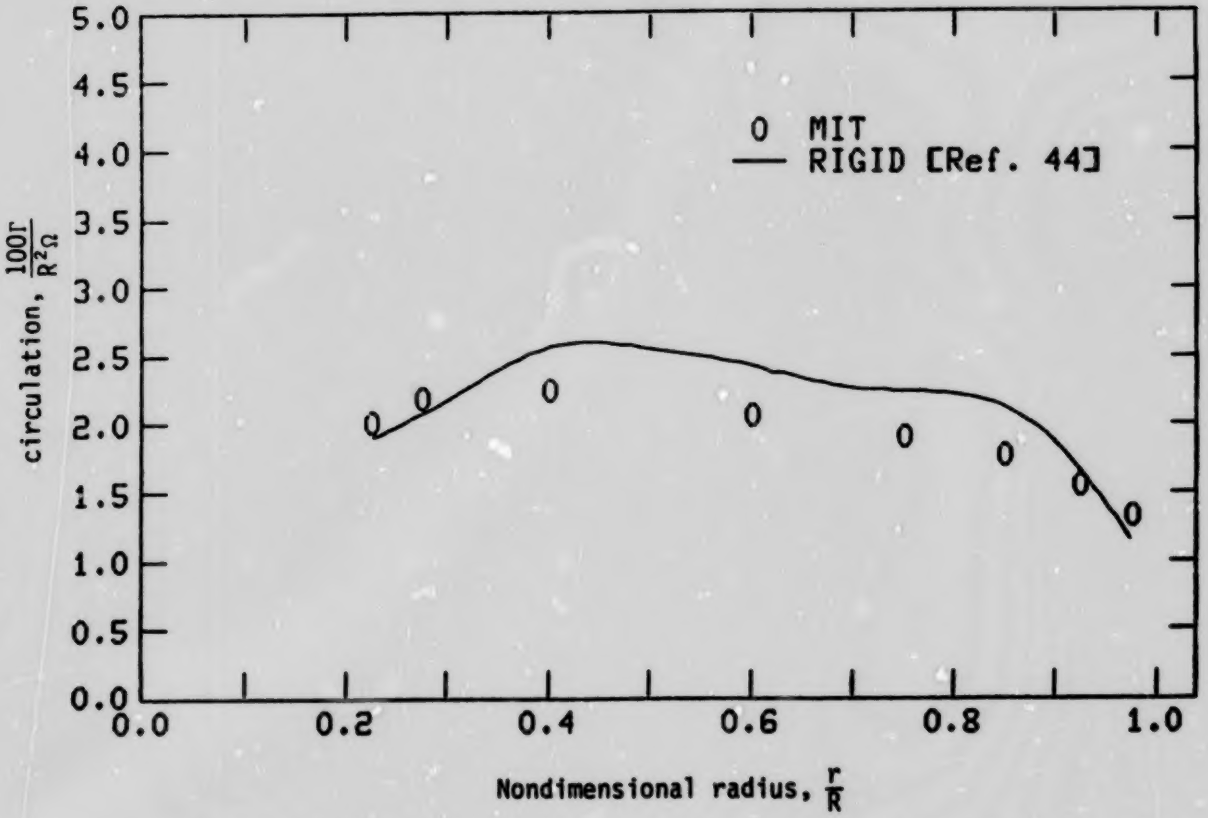

Fig. 6-13 Comparison of rigid wake dimensionless circulation distribution along the blade with existing MIT [7] date (case 1).

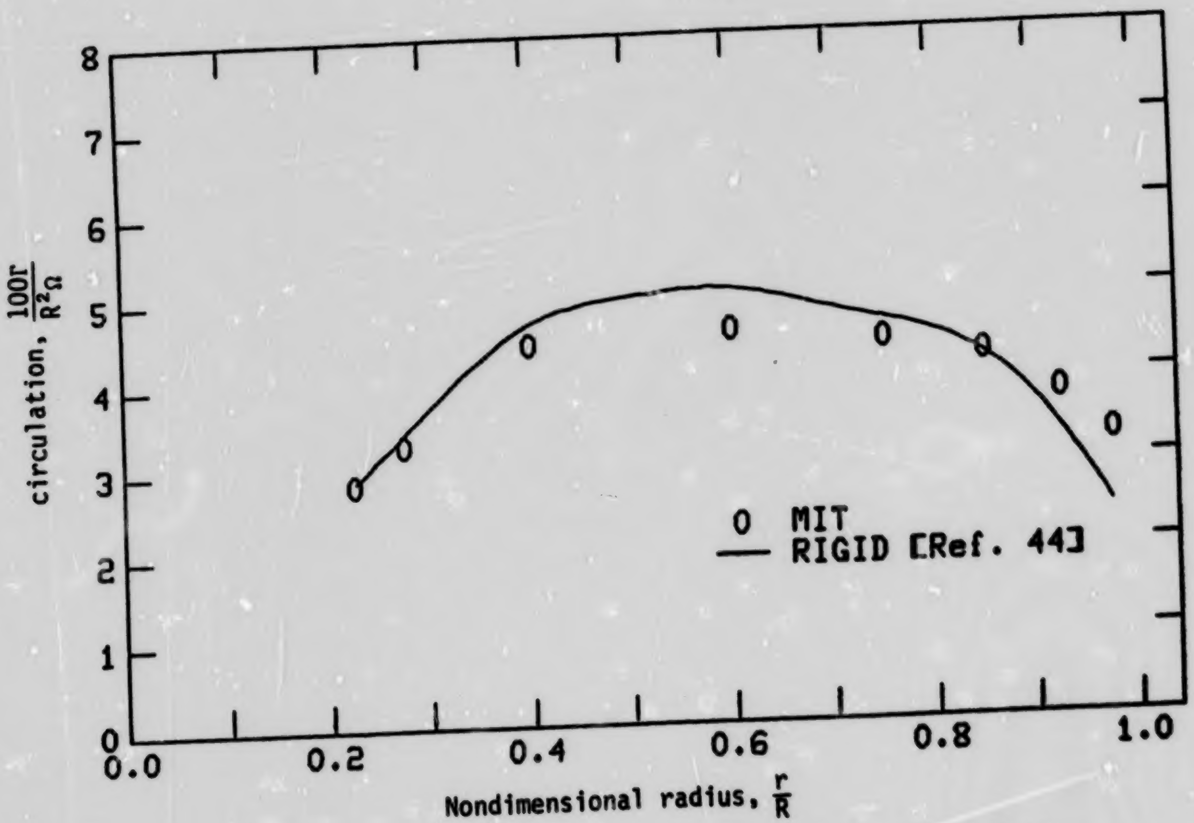

Fig. 6-14 Comparison of rigid wake dimensionless circulation distribution along the blade with existing MIT [7] data (case 2).

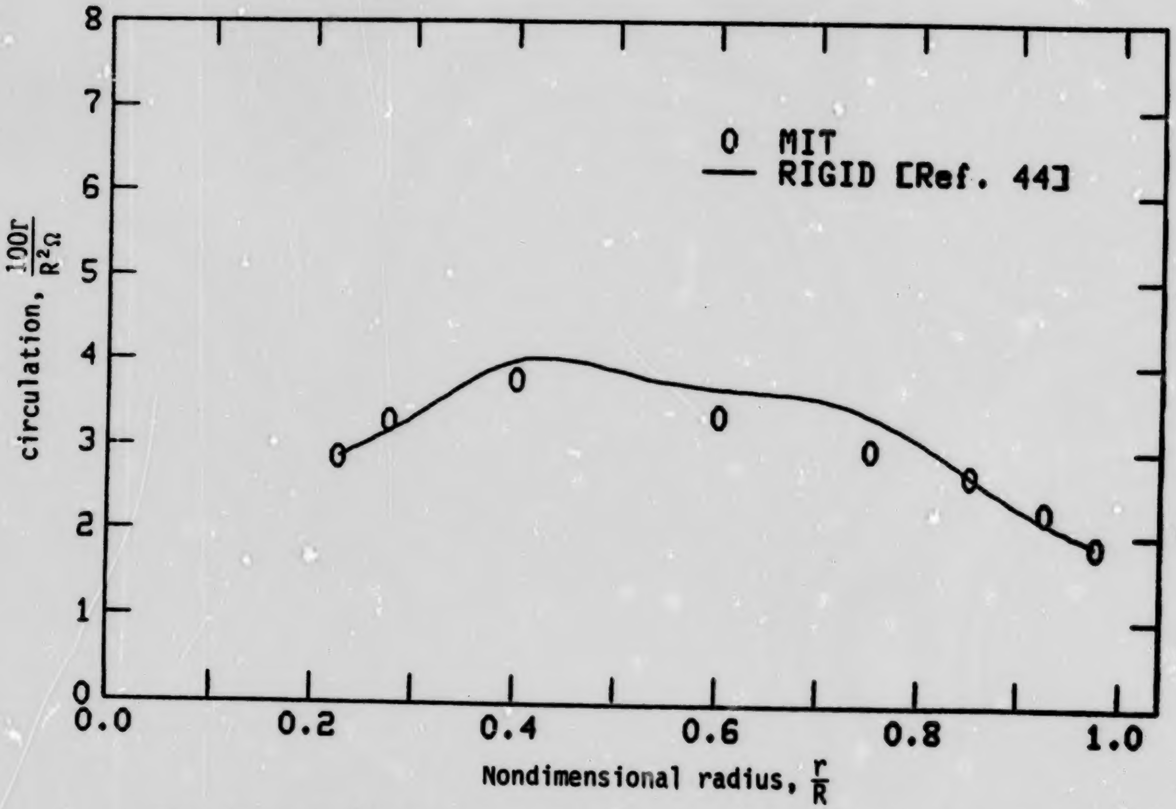

Fig. 6-15 Comparison of rigid wake dimensionless circulation distribution along the blade with existing MIT [7] data (case 3).

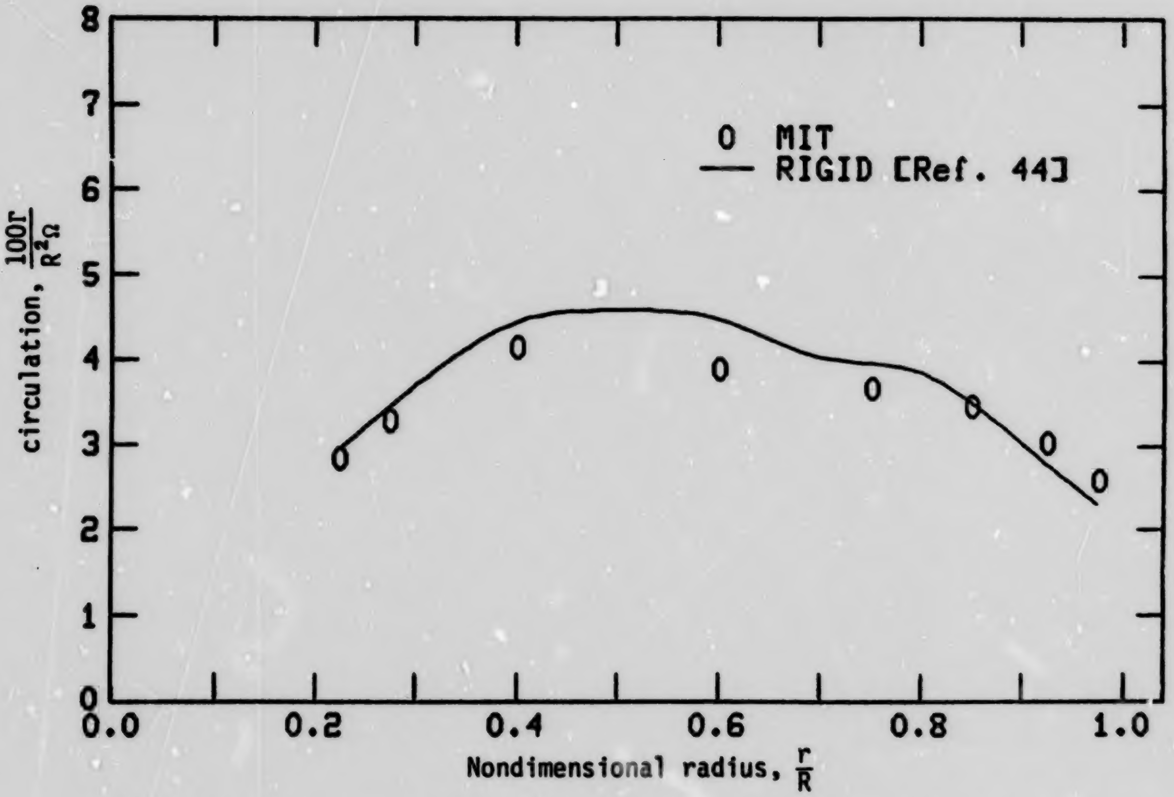

Fig. 6-16 Comparison of rigid wake dimensionless circulation distribution along the blade with existing MIT [7] data (case 4).

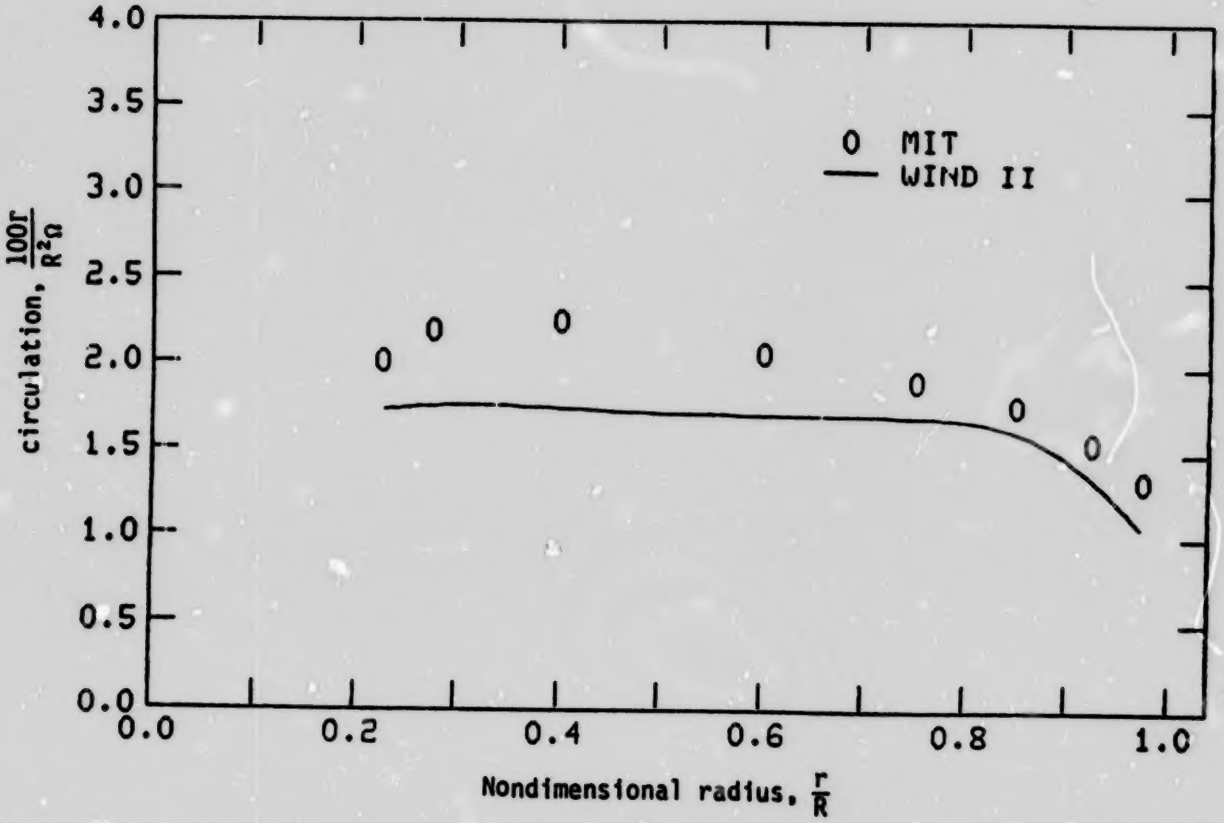

Fig. 6-17 Comparison of WIND II [54] dimensionless circulation distribution with existing MIT [7] data (case 1).

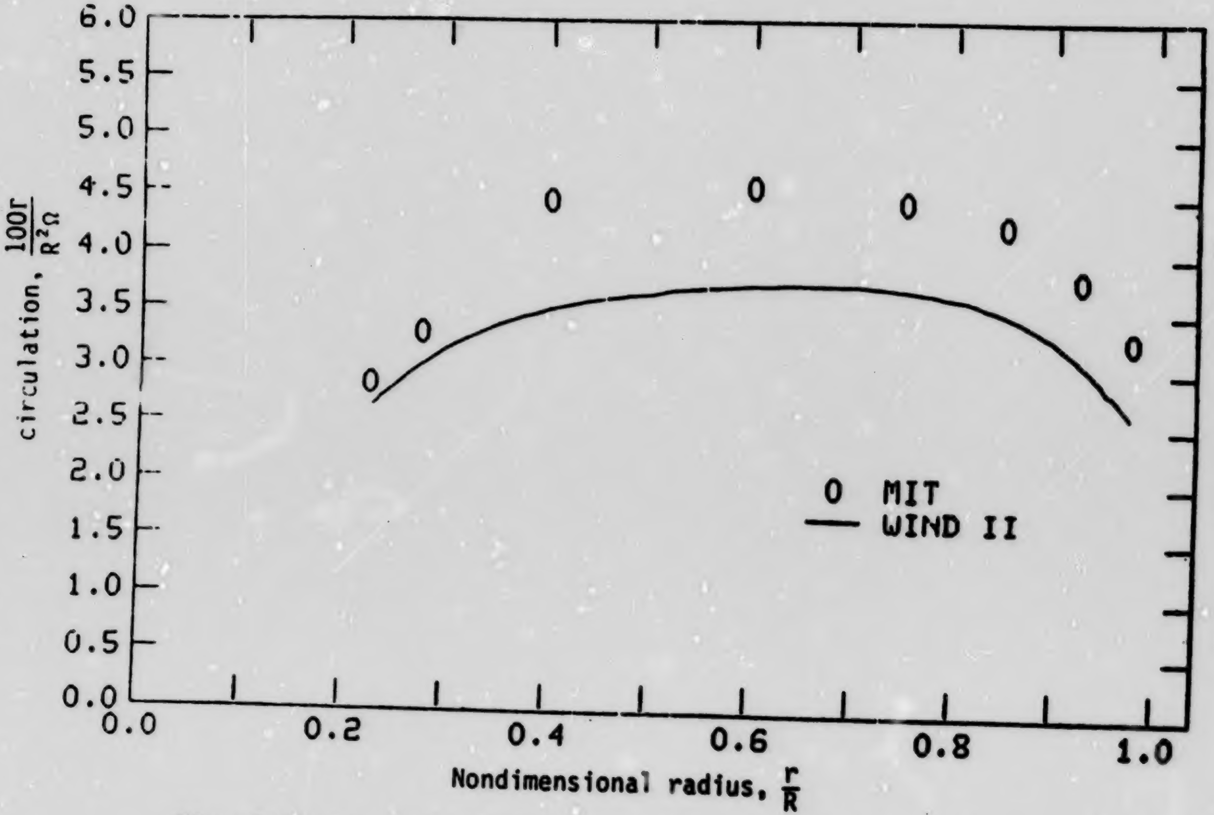

Fig. 6-18 Comparison of WIND II [54] dimensionless circulation distribution with existing MIT [7] data (case 2).

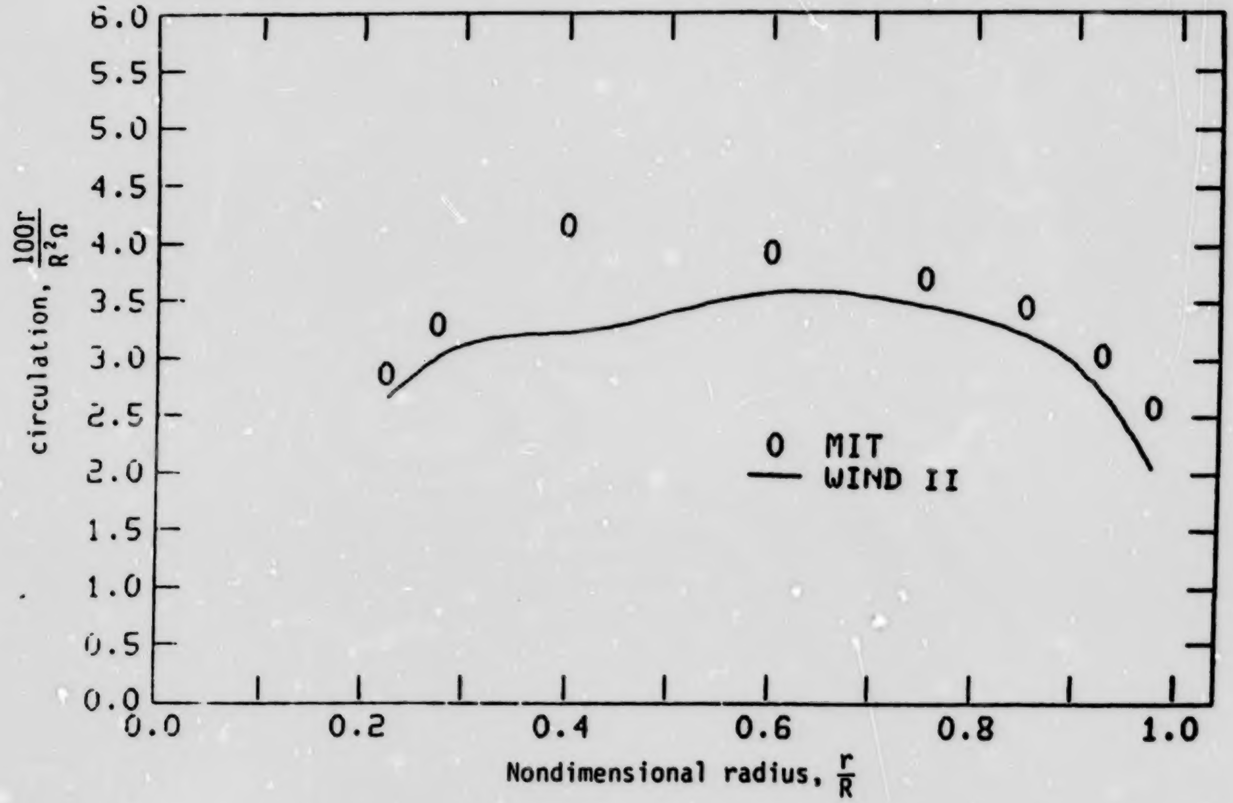

Fig. 6-19 Comparison of WIND II [54] dimensionless circulation distribution with existing MIT [7] data (case 3).

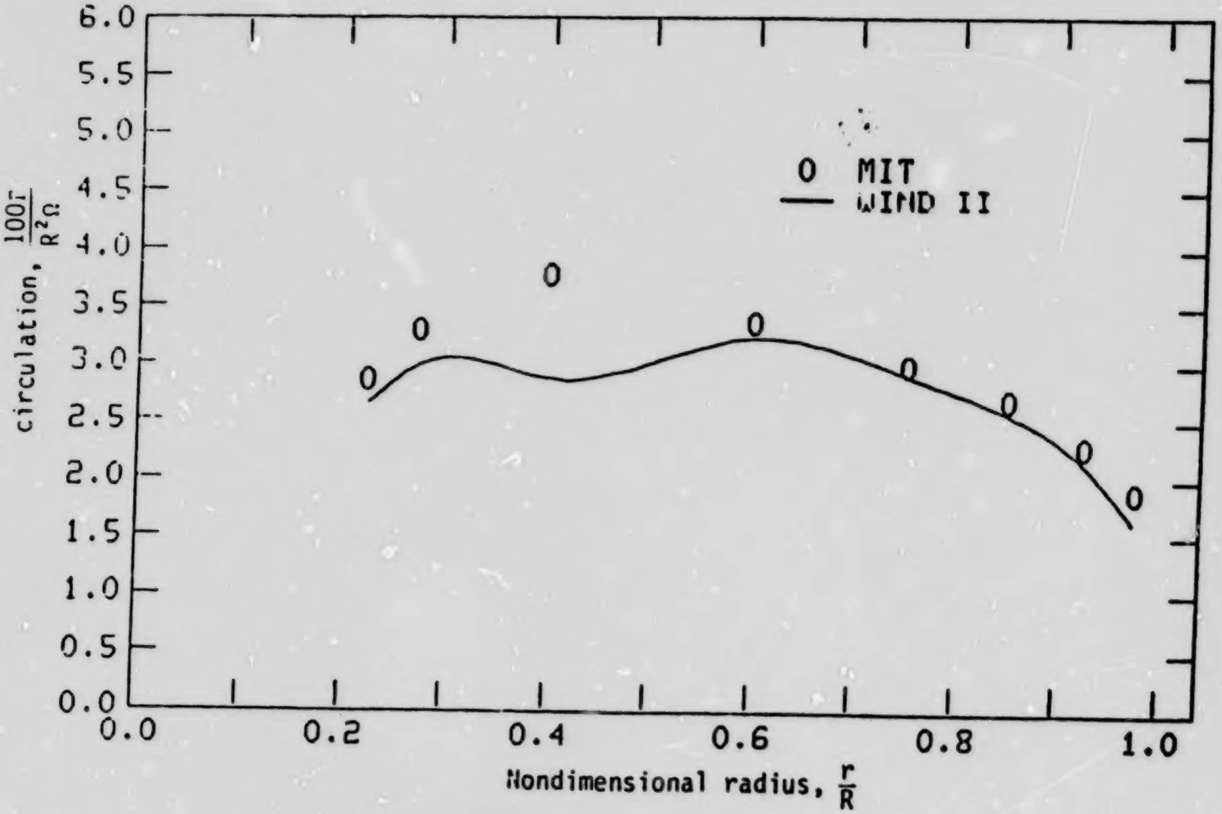

Fig. 6-20 Comparison of WIND II [54] dimensionless circulation distribution with existing MIT [7] data (case 4).

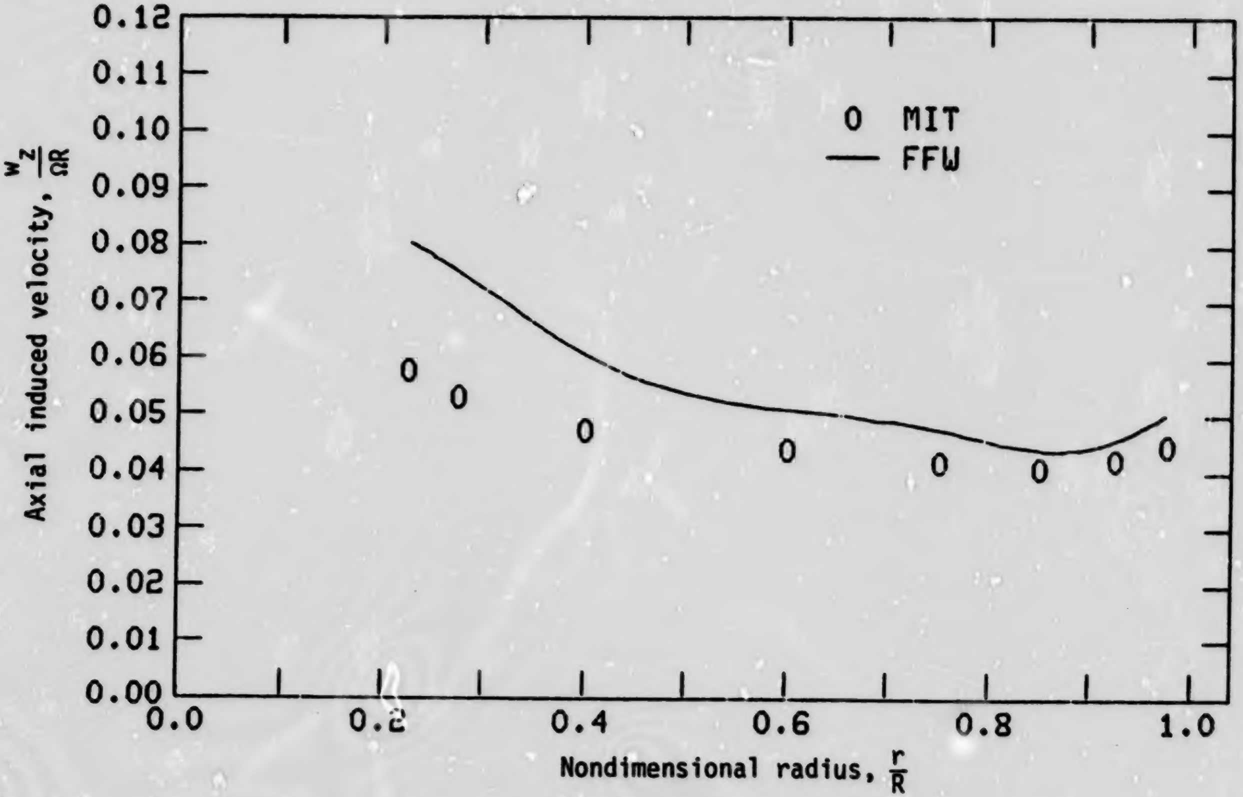

Fig. 6-21 Comparison of fast free wake dimensionless axial induced velocity distribution along the blade with existing MIT [7] data (case 1).

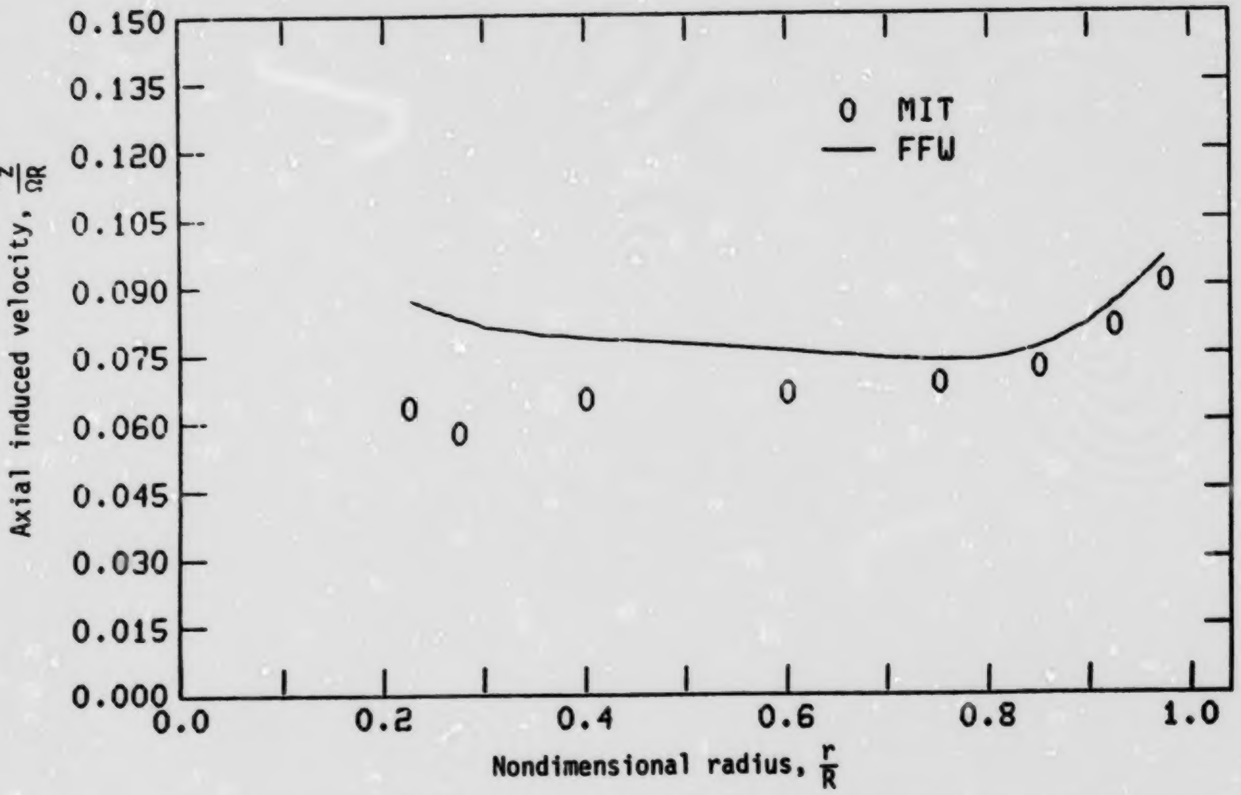

Fig. 6-22 Comparison of fast free wake dimensionless axial induced velocity distribution along the blade with existing MIT [7] data (case 2).

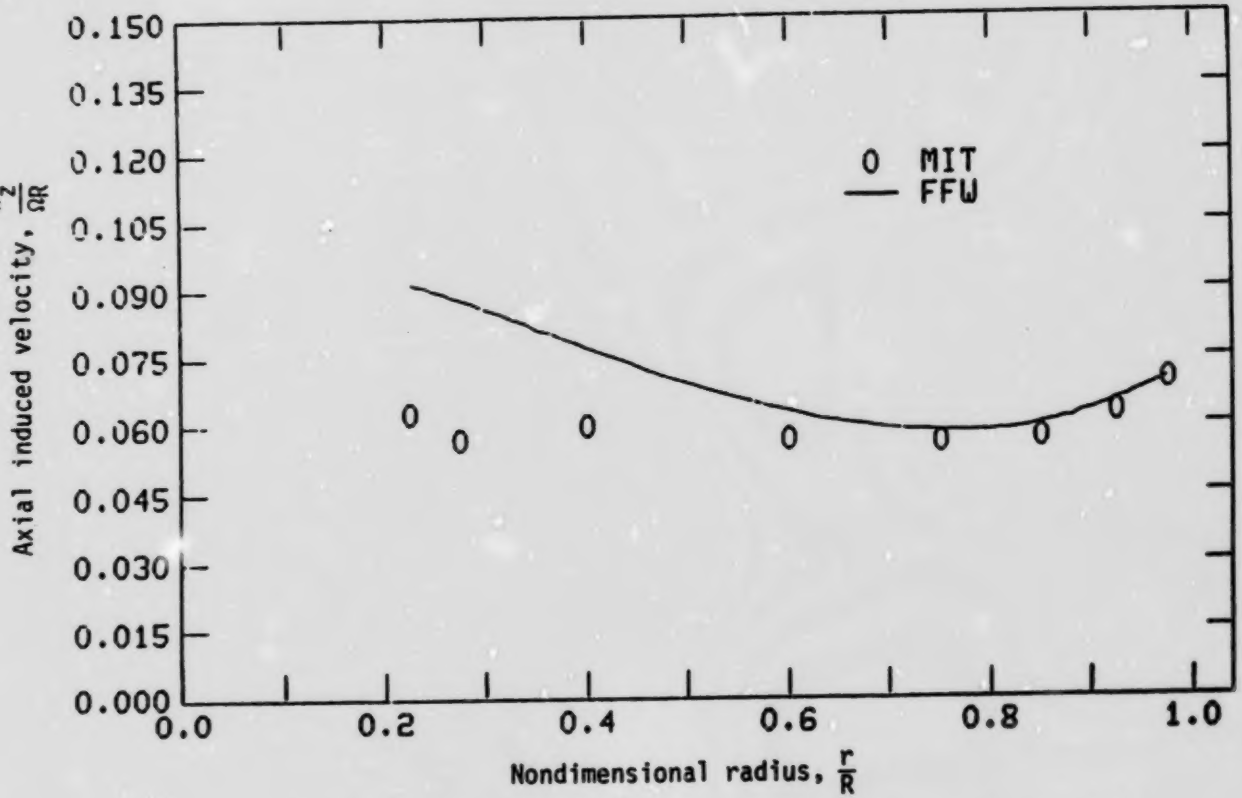

Fig. 6-23 Comparison of fast free wake dimensionless axial induced velocity distribution along the blade with existing MIT [7] data (case 3).

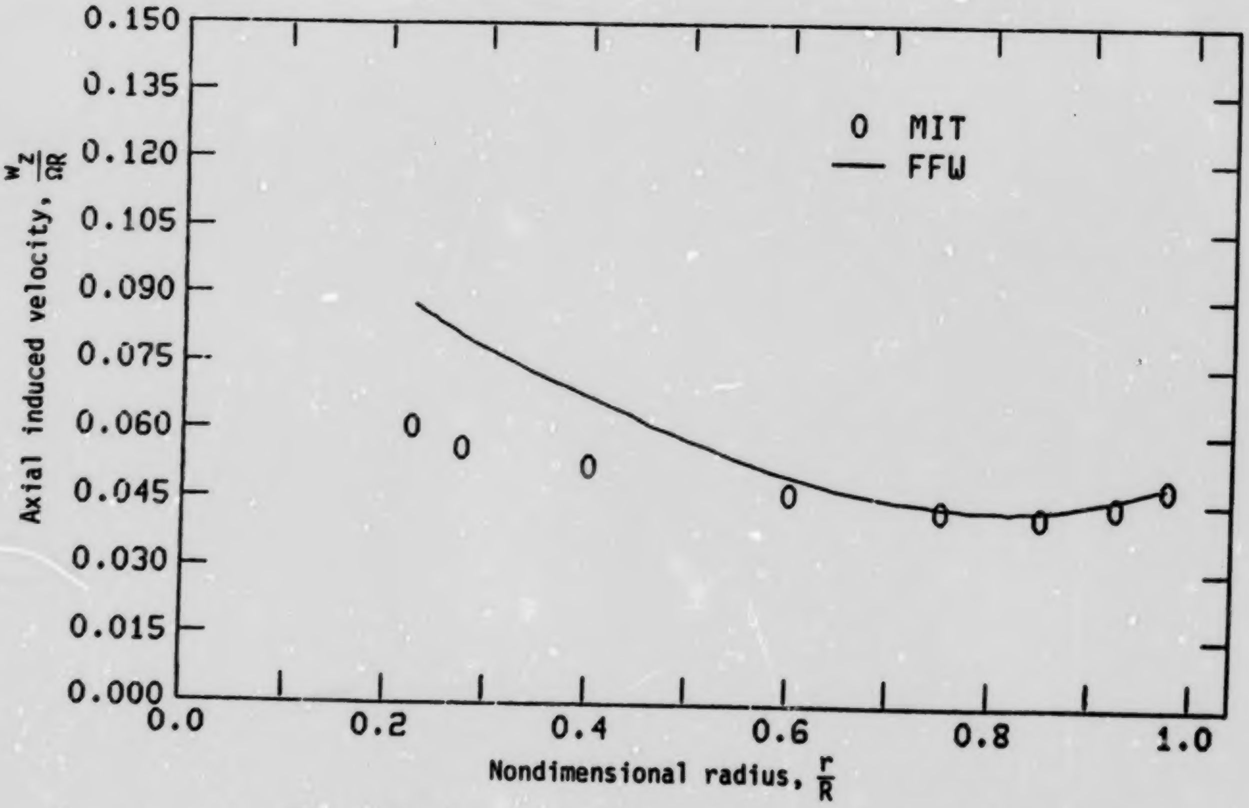

Fig. 6-24 Comparison of fast free wake dimensionless axial induced velocity distribution along the blade with existing MIT [7] data (case 4).

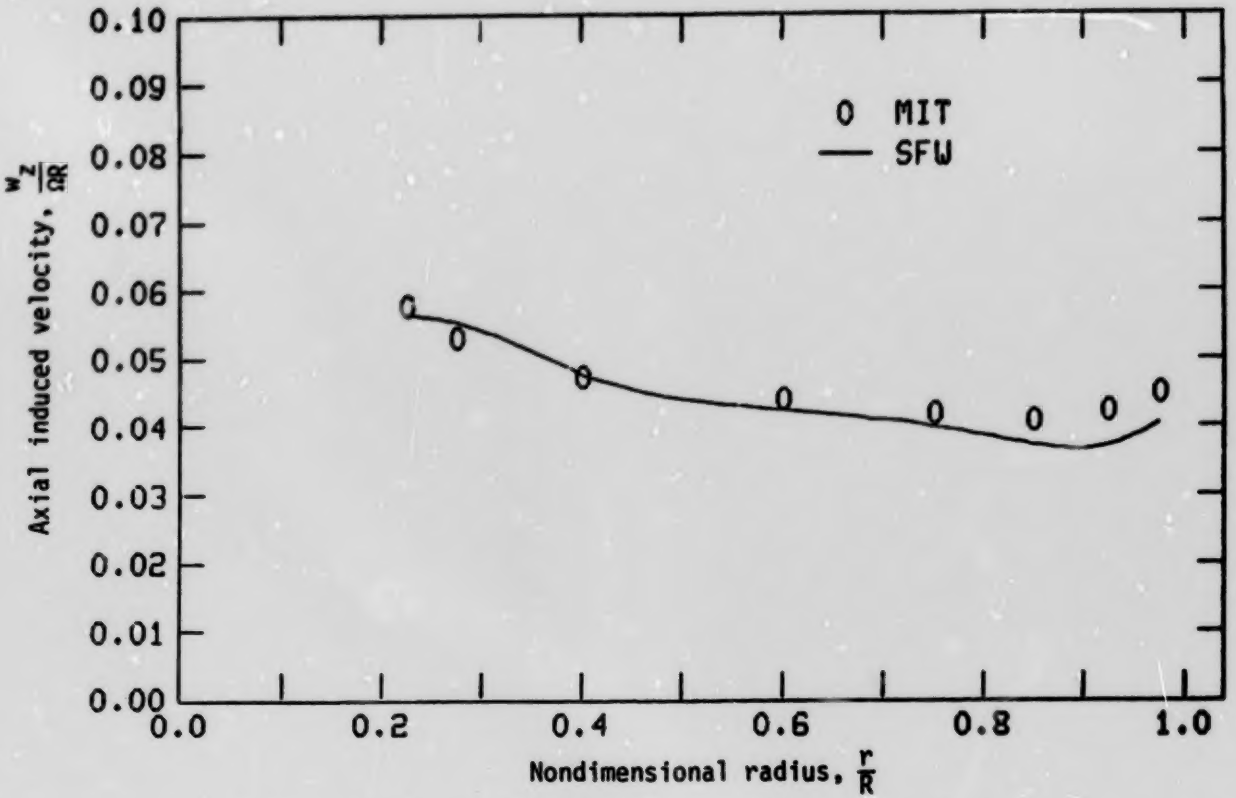

Fig. 6-25 Comparison of simplified free wake dimensionless axial induced velocity distribution along the blade with existing MIT [7] data (case 1).

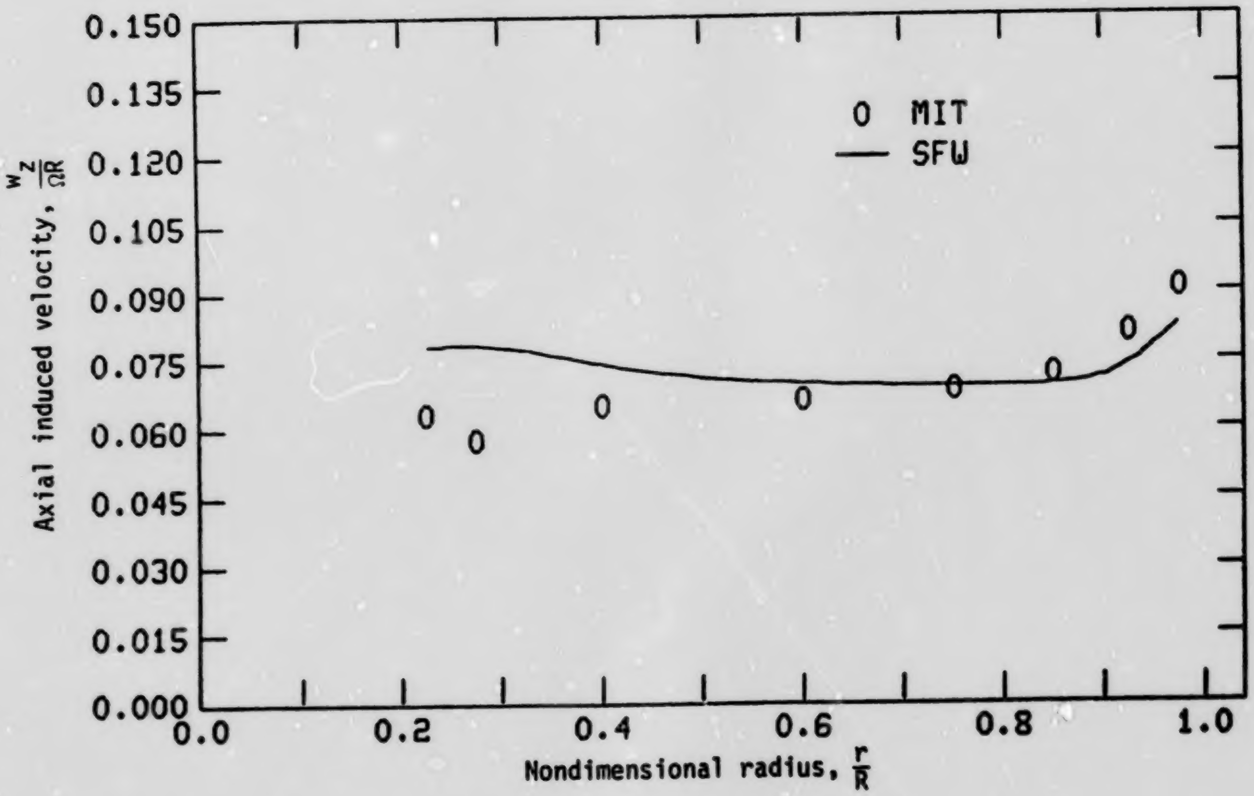

Fig. 6-26 Comparison of simplified free wake dimensionless axial induced velocity distribution along the blade with existing MIT [7] data (case 2).

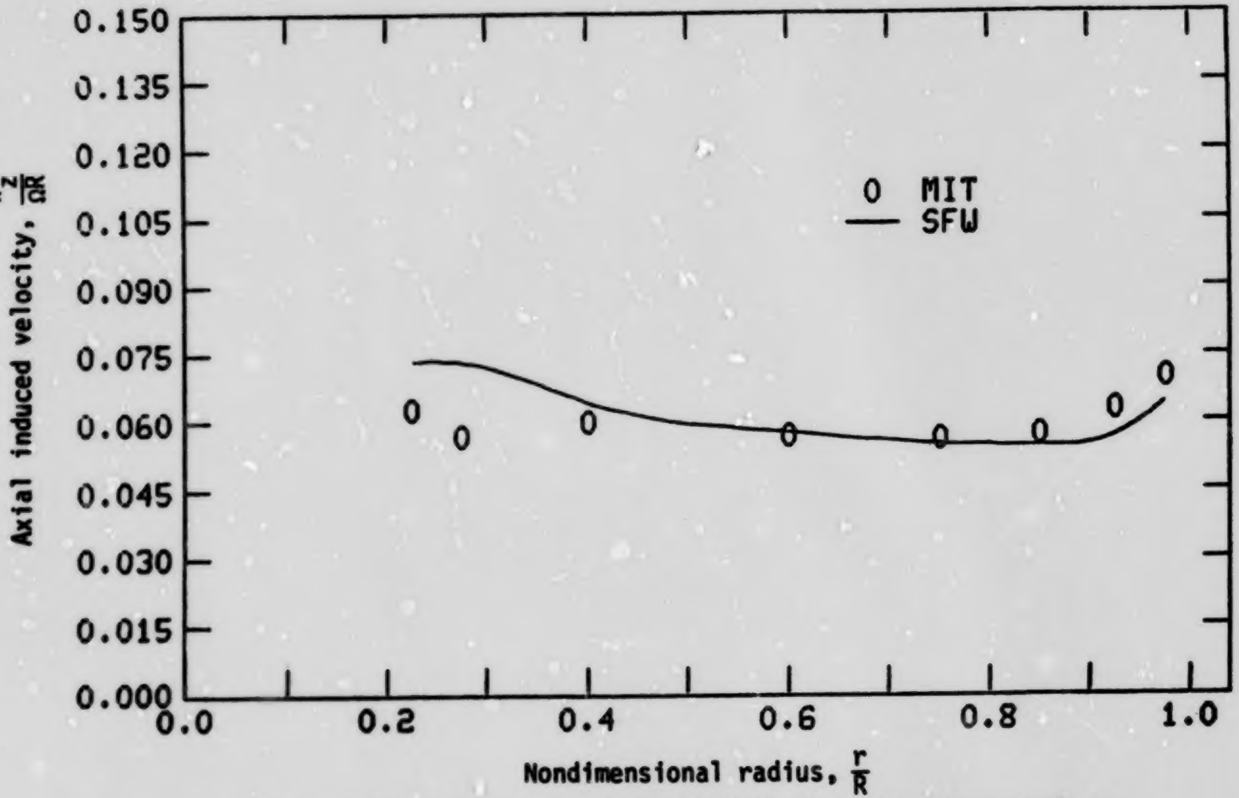

Fig. 6-27 Comparison of simplified free wake dimensionless axial induced velocity distribution along the blade with existing MIT [7] data (case 3).

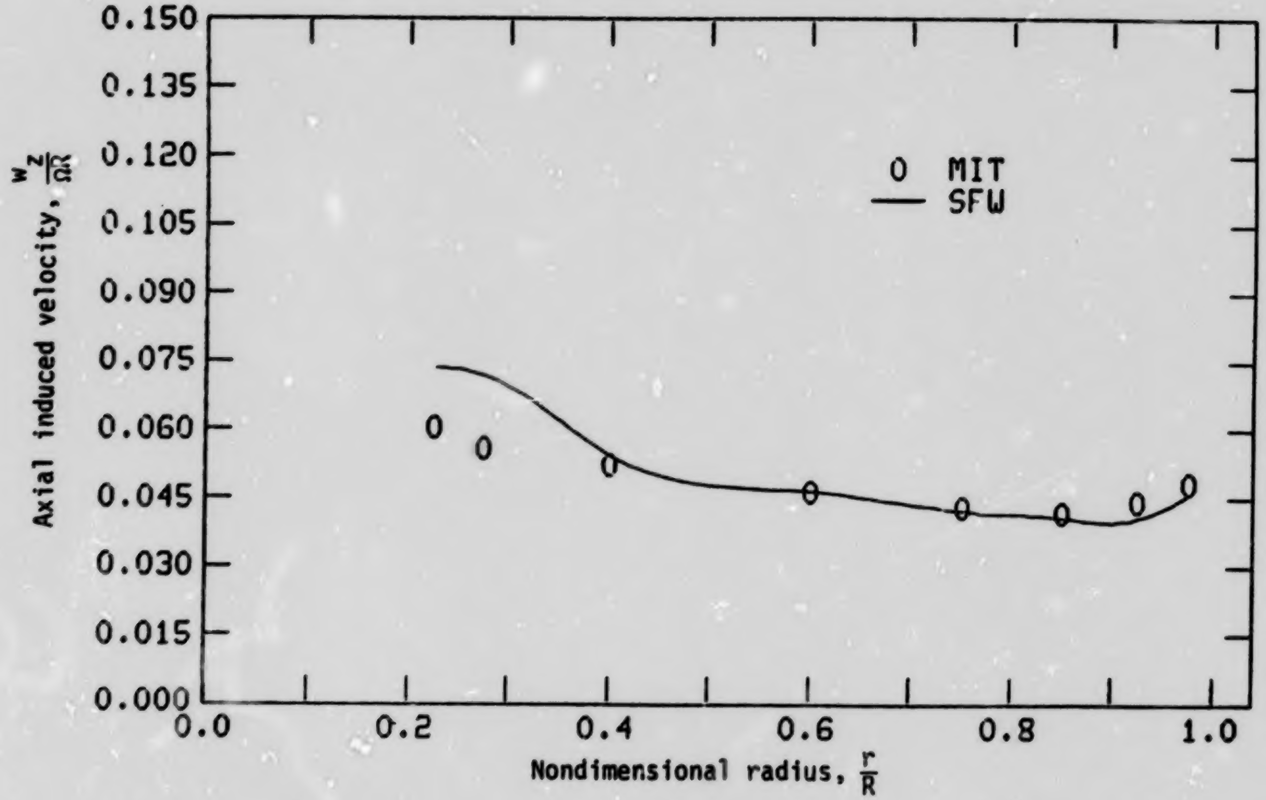

Fig. 6-28 Comparison of simplified free wake dimensionless axial induced velocity distribution along the blade with existing MIT [7] data (case 4).

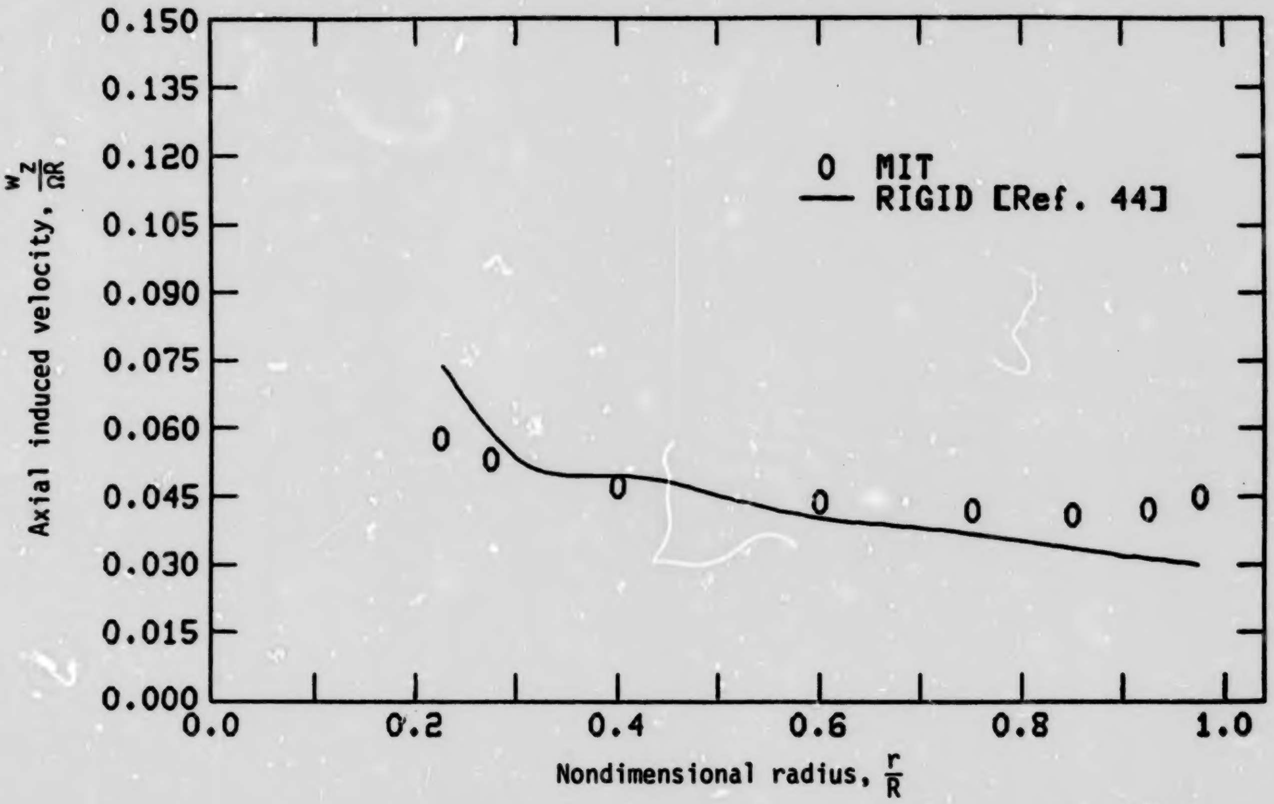

Fig. 6-29 Comparison of rigid wake dimensionless axial induced velocity distribution along the blade with existing MIT [7] data (case 1).

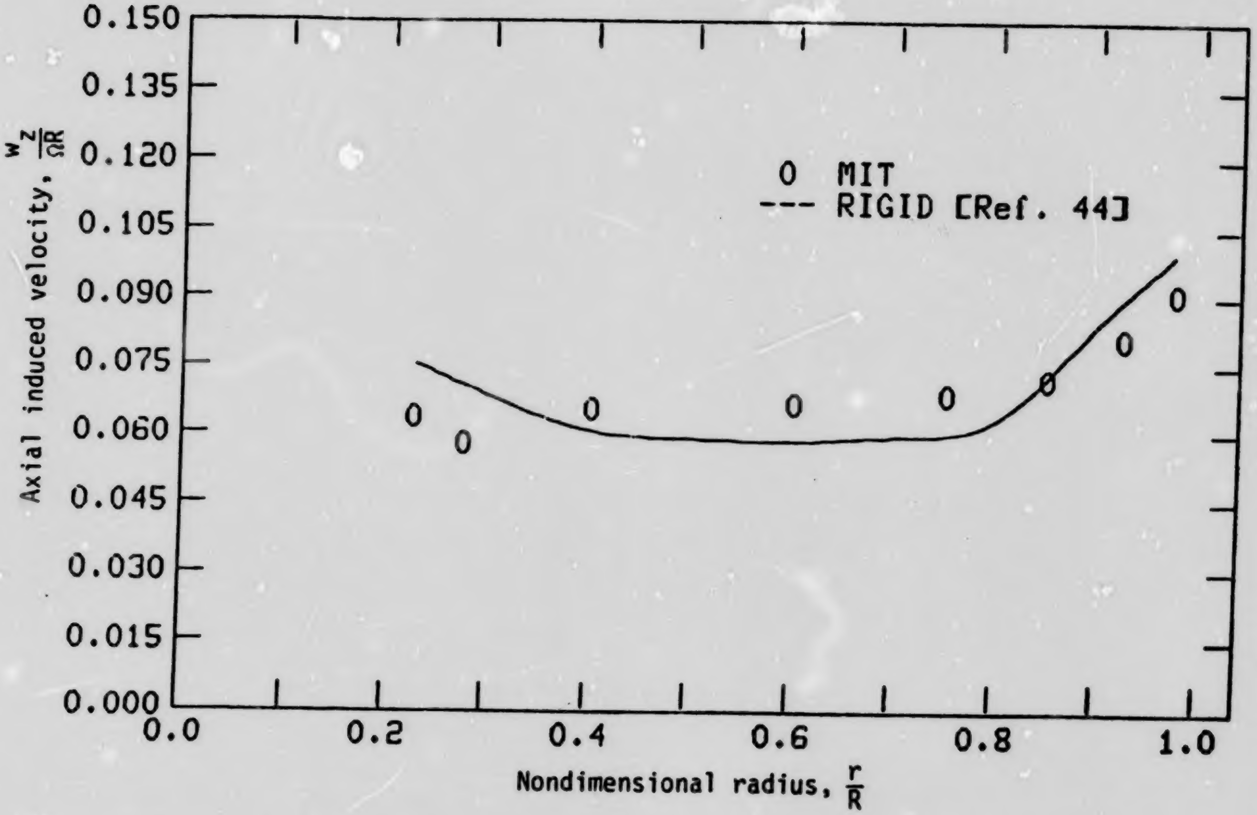

Fig. 6-30 Comparison of rigid wake dimensionless axial induced velocity distribution along the blade with existing MIT [7] data (case 2).

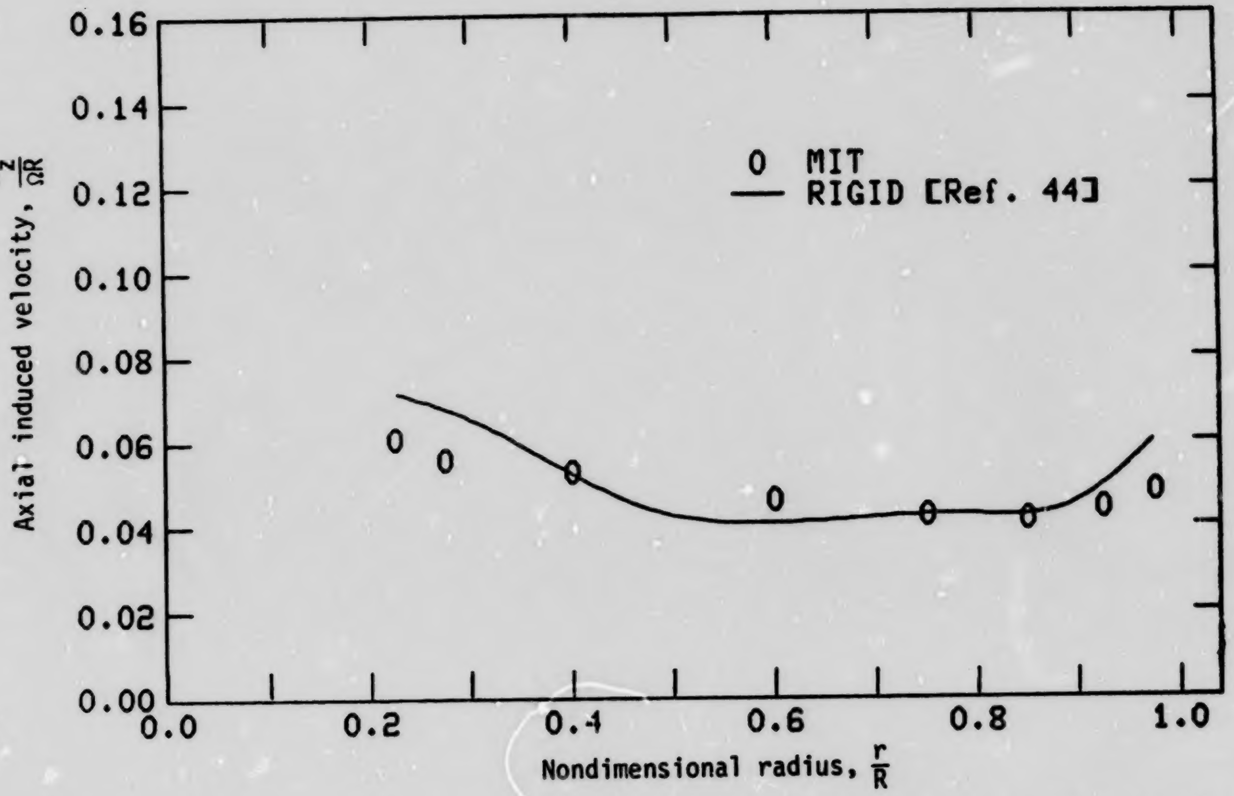

Fig. 6-31 Comparison of rigid wake dimensionless axial induced velocity distribution along the blade with existing MIT [7] data (case 3).

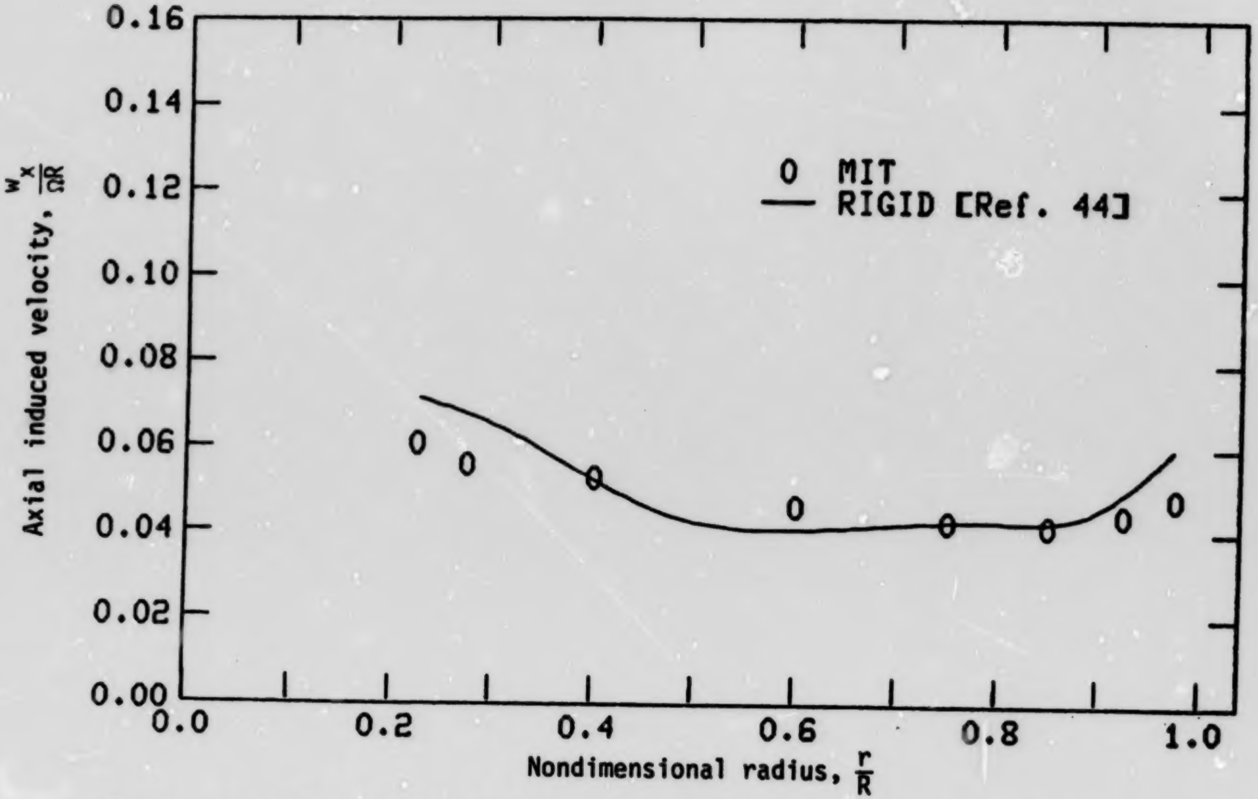

Fig. 6-32 Comparison of rigid wake dimensionless axial induced velocity distribution along the blade with existing MIT [7] data (case 4).

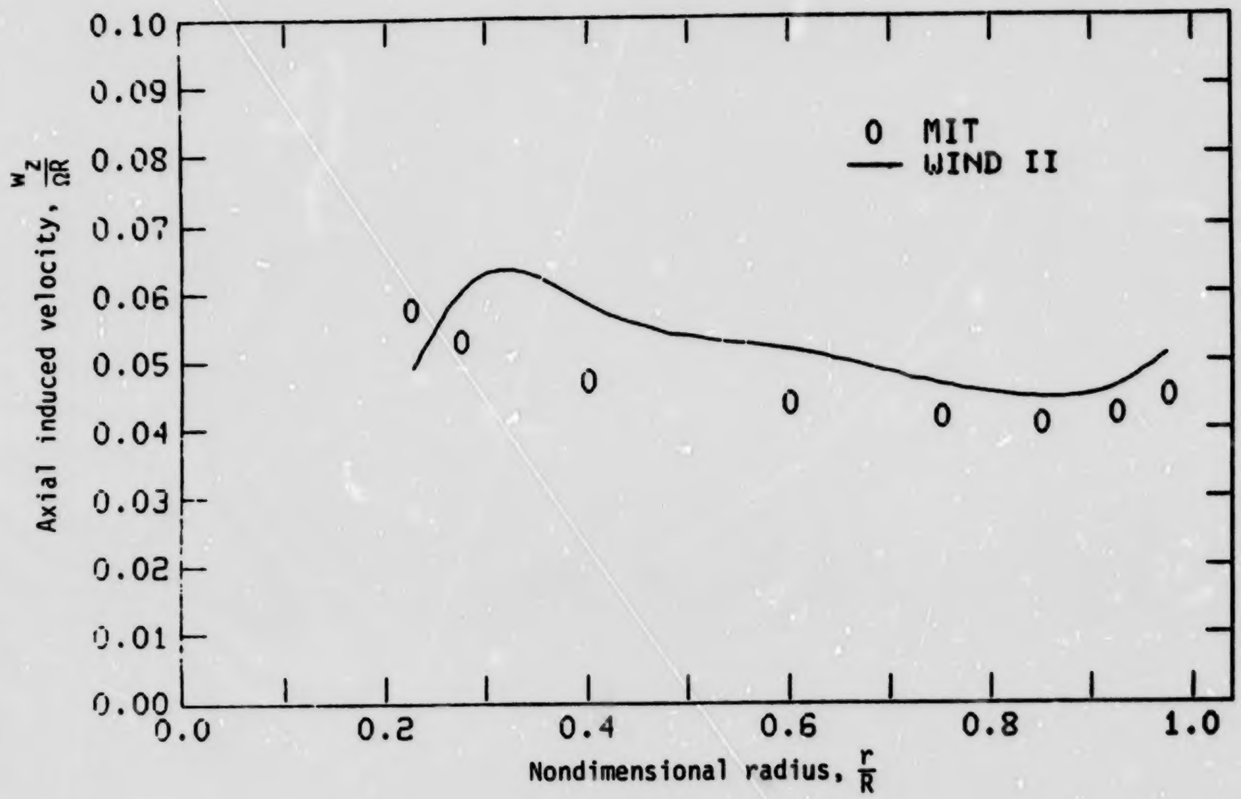

Fig. 6-33 Comparison of WIND II [54] dimensionless induced velocity distribution along the blade with existing MIT [7] data (case 1).

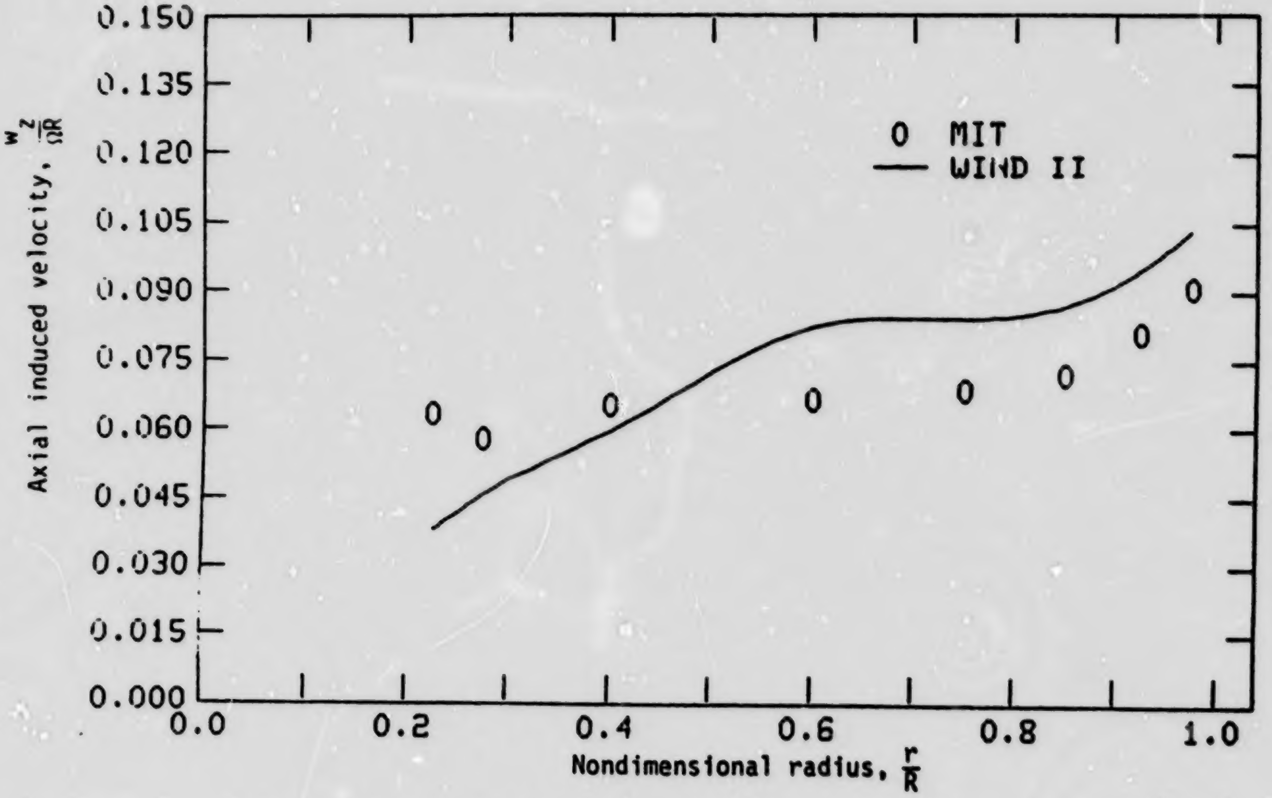

Fig. 6-34 Comparison of WIND II [54] dimensionless induced velocity distribution along the blade with existing MIT [7] data (case 2).

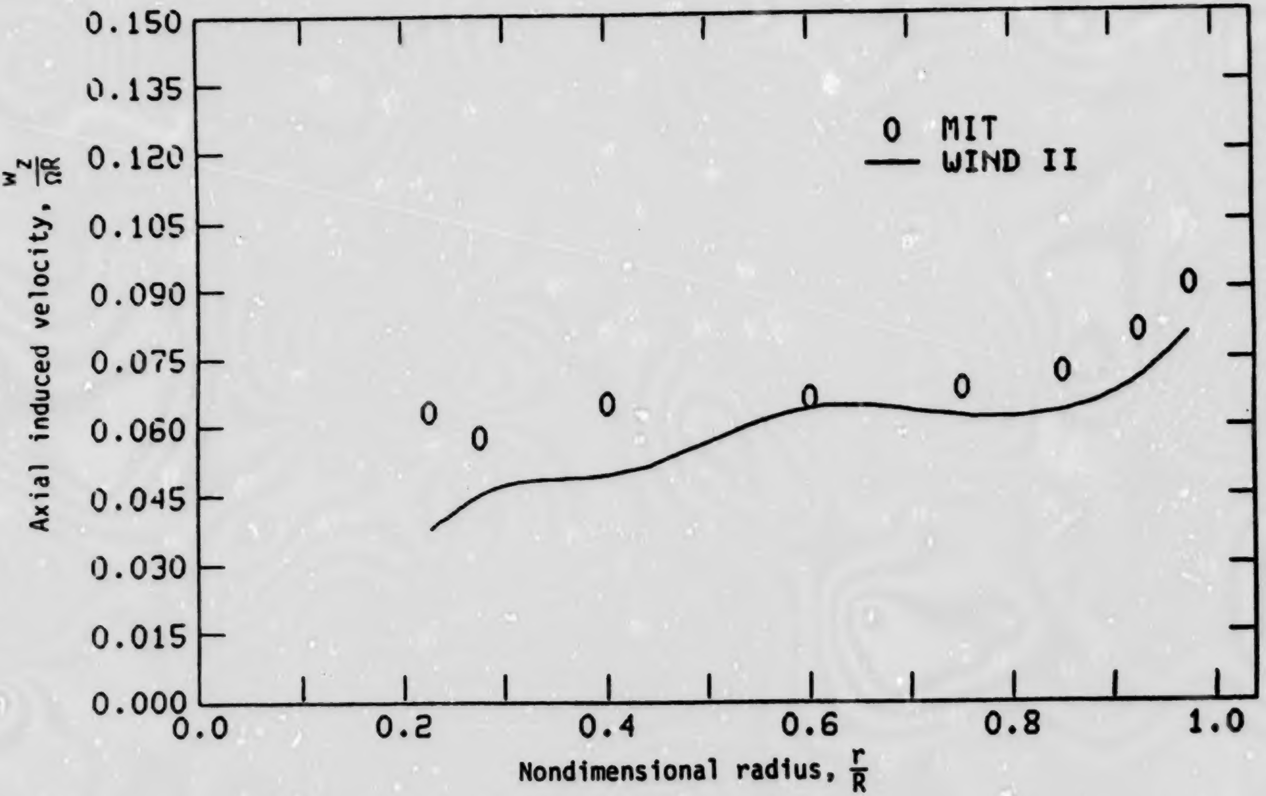

Fig. 6-35 Comparison of WIND II [54] dimensionless induced velocity distribution along the blade with existing MIT [7] data (case 3).

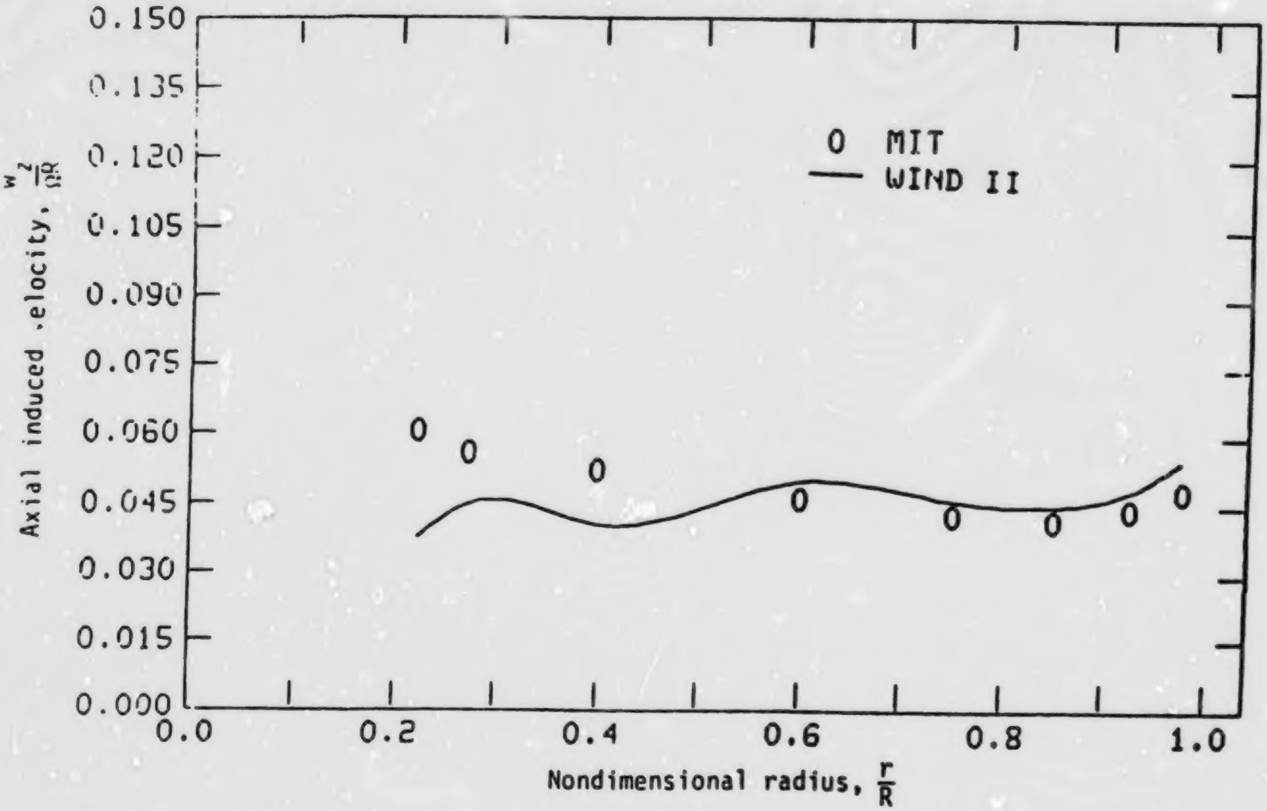

Fig. 6-36 Comparison of WIND II [54] dimensionless induced velocity distribution along the blade with existing MIT [7] data (case 4).

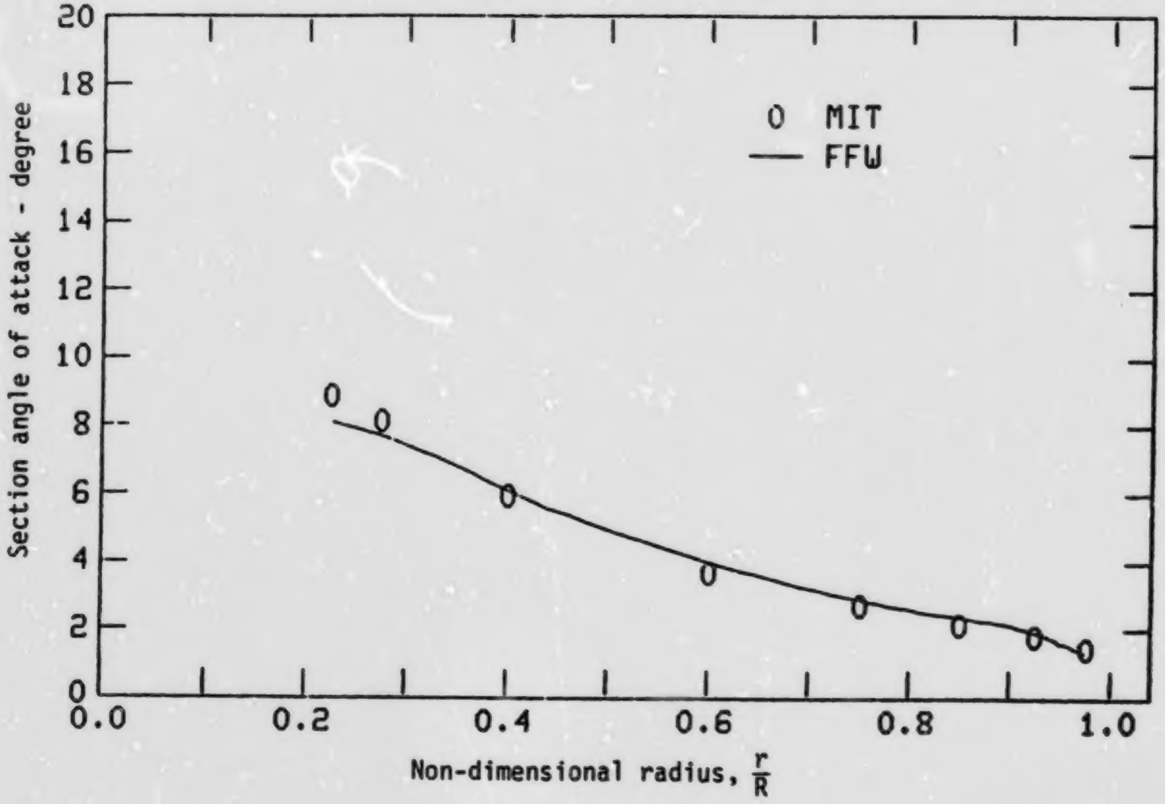

Fig. 6-37 Comparison of fast free wake (FFW) effective angle of attack distribution along the blade with existing MIT [7] data (case 1).

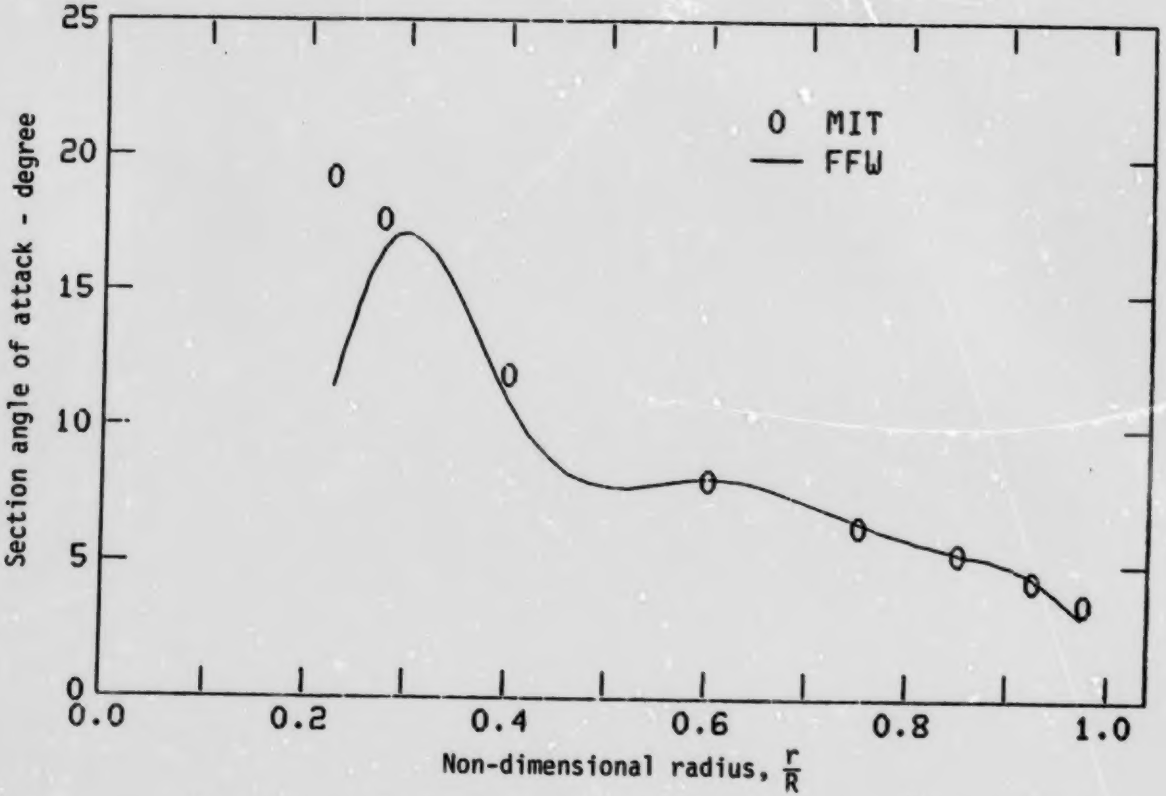

Fig. 6-38 Comparison of fast free wake (FFW) effective angle of attack distribution along the blade with existing MIT [7] data (case 2).

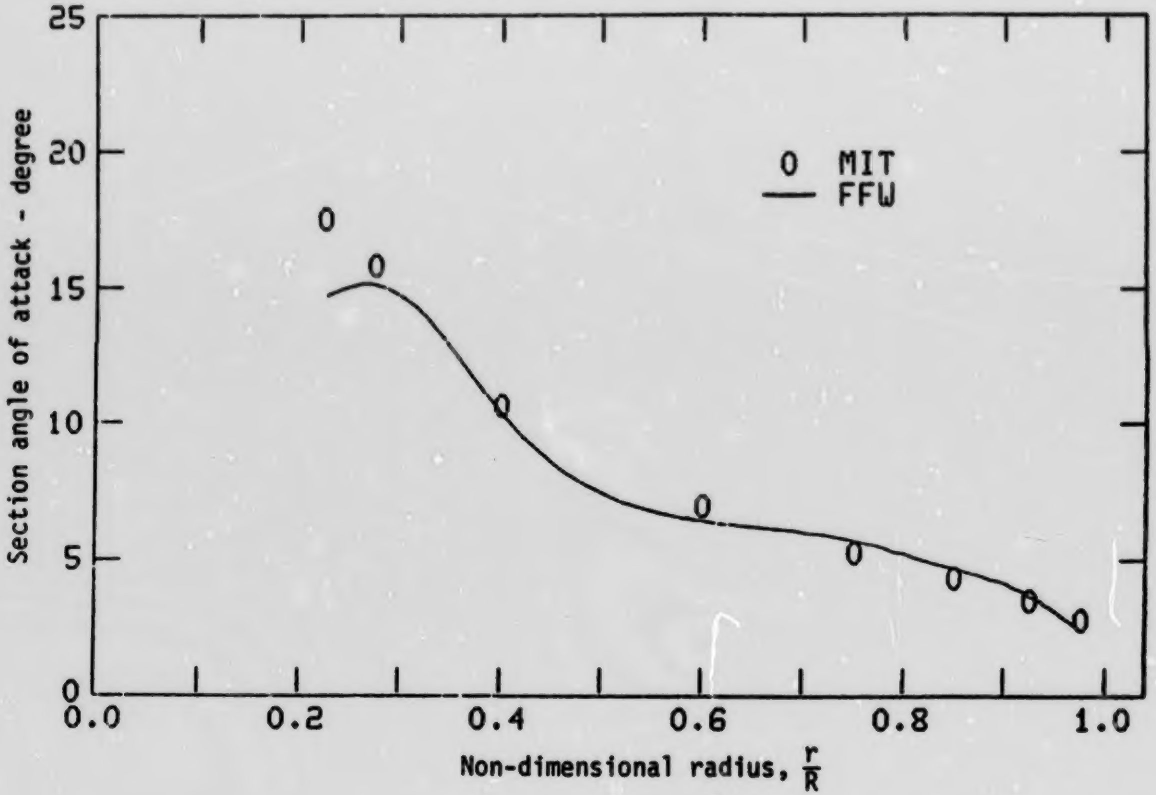

Fig. 6-39 Comparison of fast free wake (FFW) effective angle of attack distribution along the blade with existing MIT [7] data (case 3).

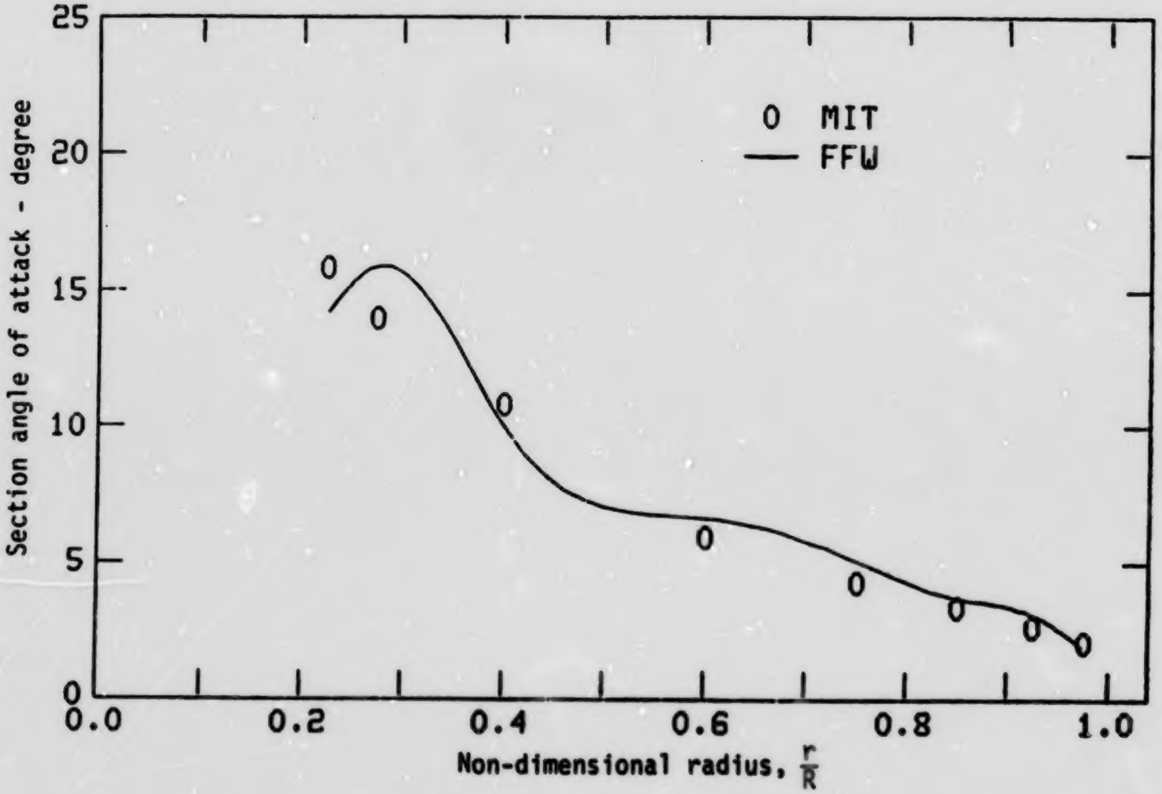

Fig. 6-40 Comparison of fast free wake (FFW) effective angle of attack distribution along the blade with existing MIT [7] data (case 4).

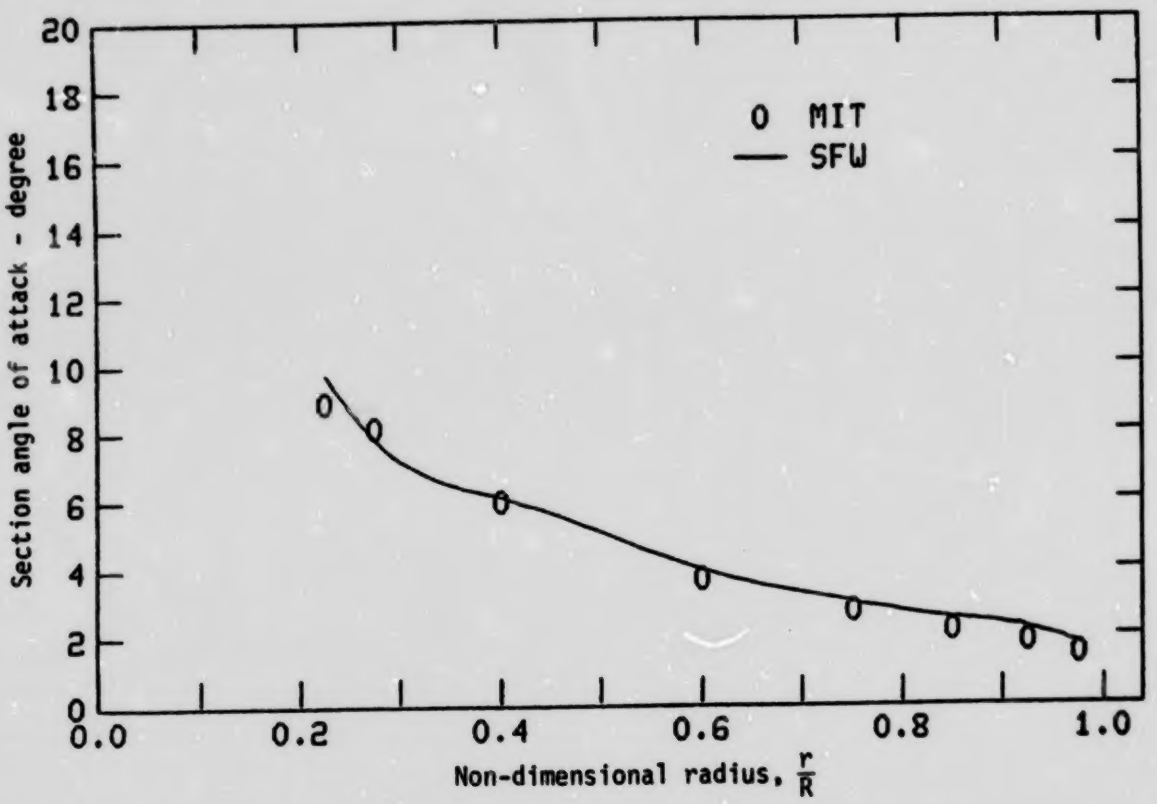

Fig. 6-41 Comparison of simplified free wake (SFW) effective angle of attack distribution along the blade with existing MIT [7] data (case 1).

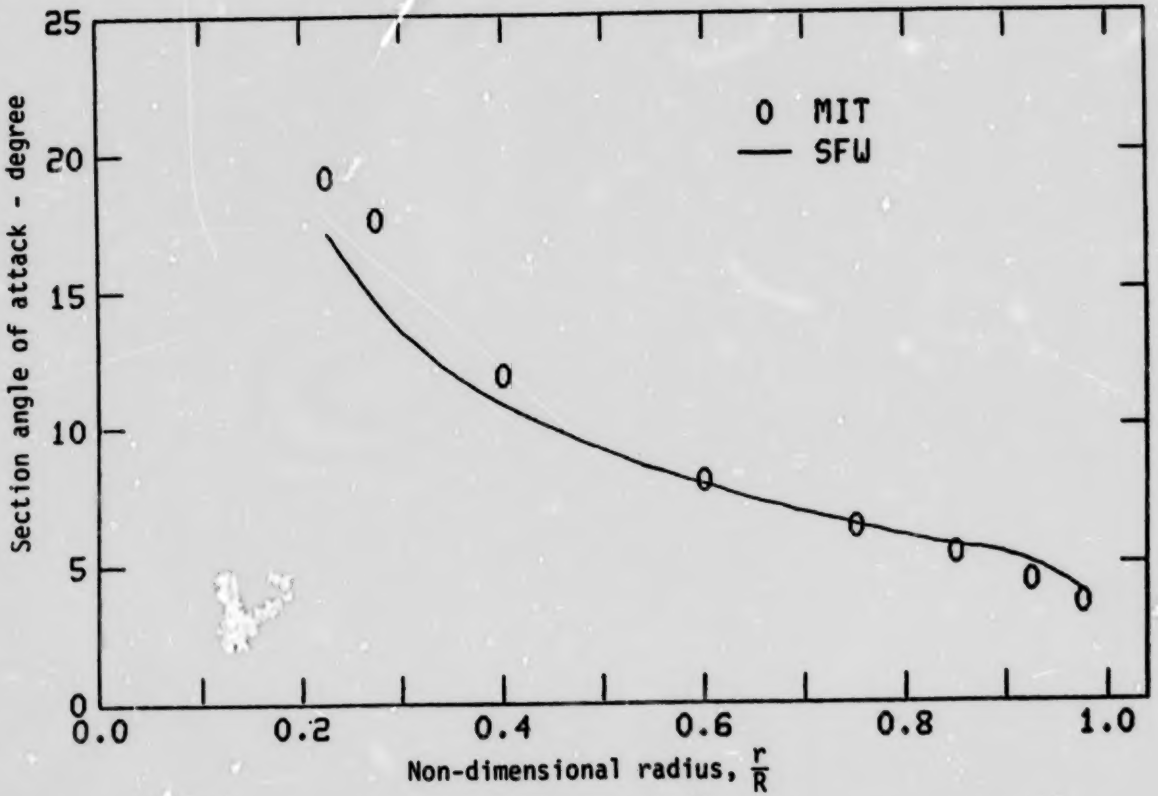

Fig. 6-42 Comparison of simplified free wake (SFW) effective angle of attack distribution along the blade with existing MIT [7] data (case 2).

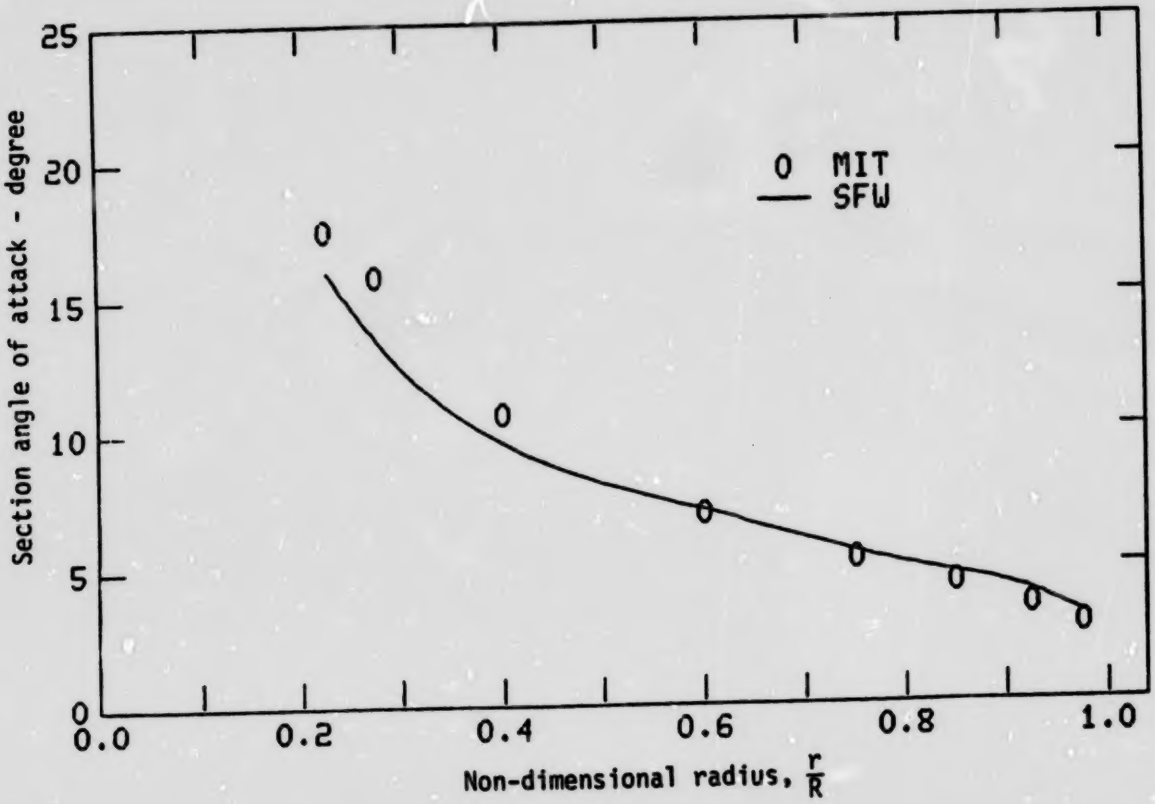

Fig. 6-43 Comparison of simplified free wake (SFW) effective angle of attack distribution along the blade with existing MIT [7] data (case 3).

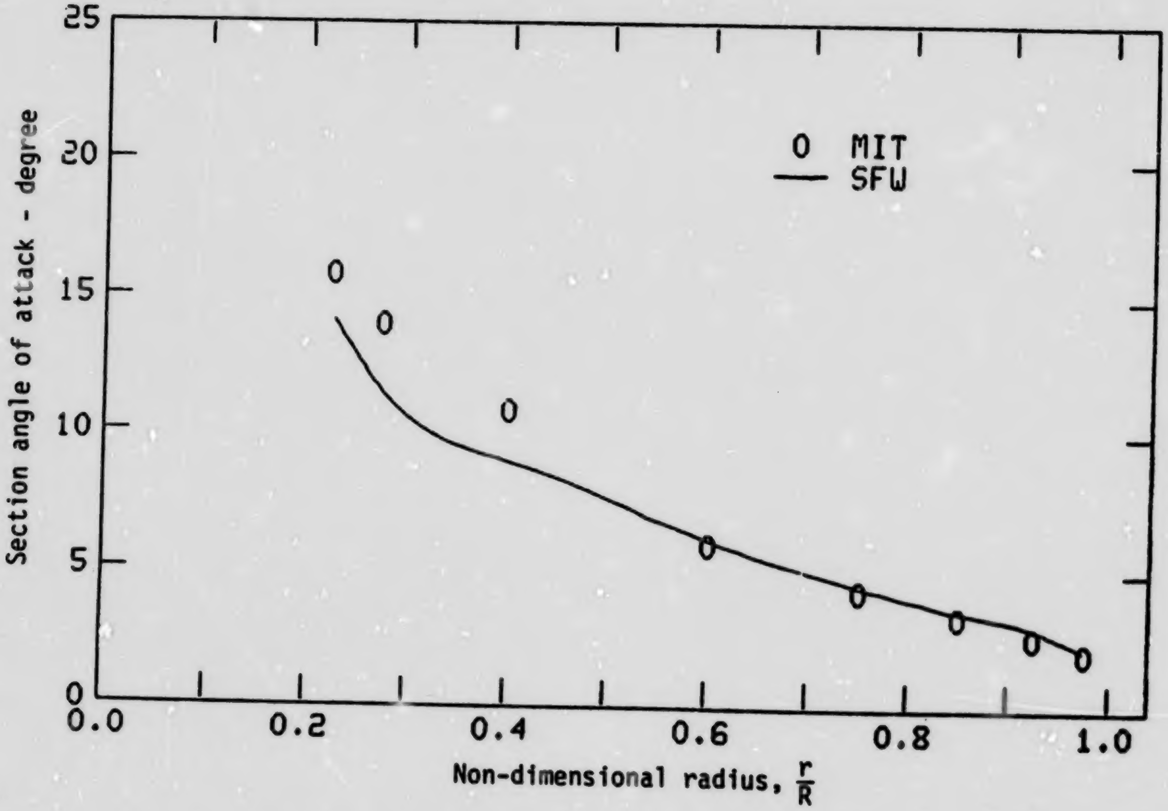

Fig. 6-44 Comparison of simplified free wake (SFW) effective angle of attack distribution along the blade with existing MIT [7] data (case 4).

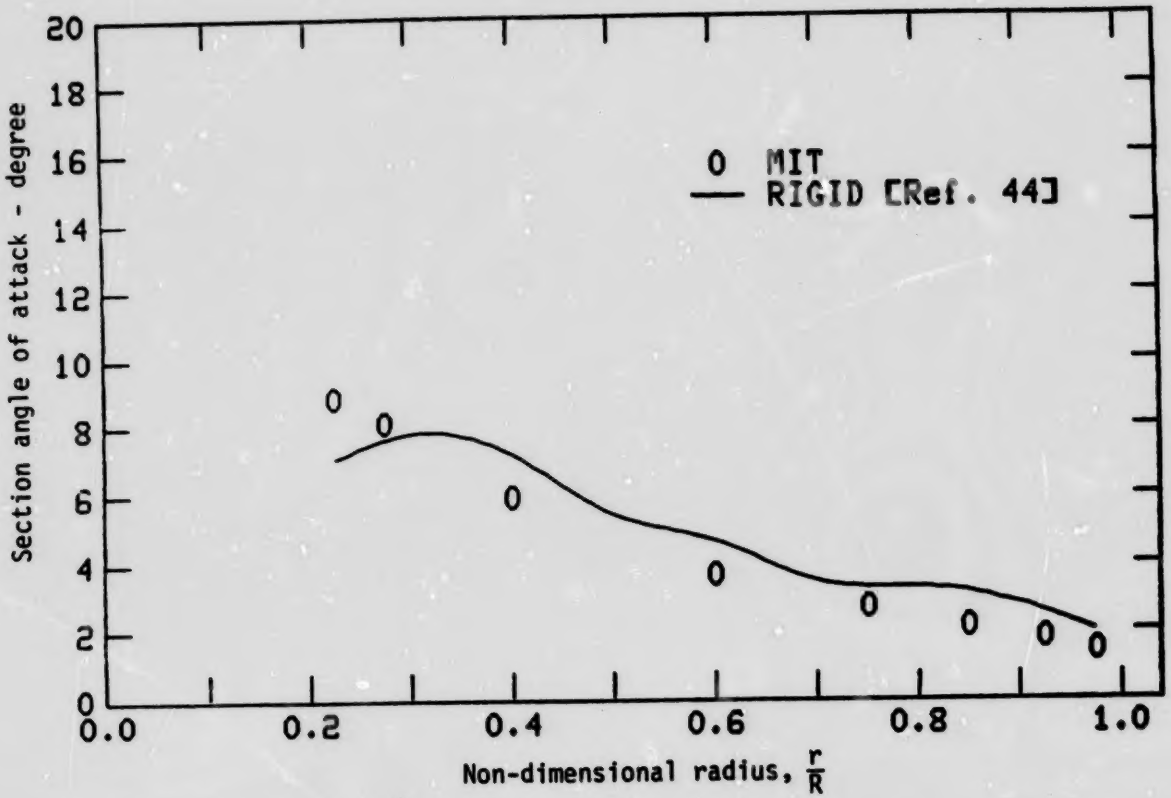

Fig. 6-45 Comparison of rigid wake effective angle of attack distribution along the blade with existing MIT [7] data (case 1).

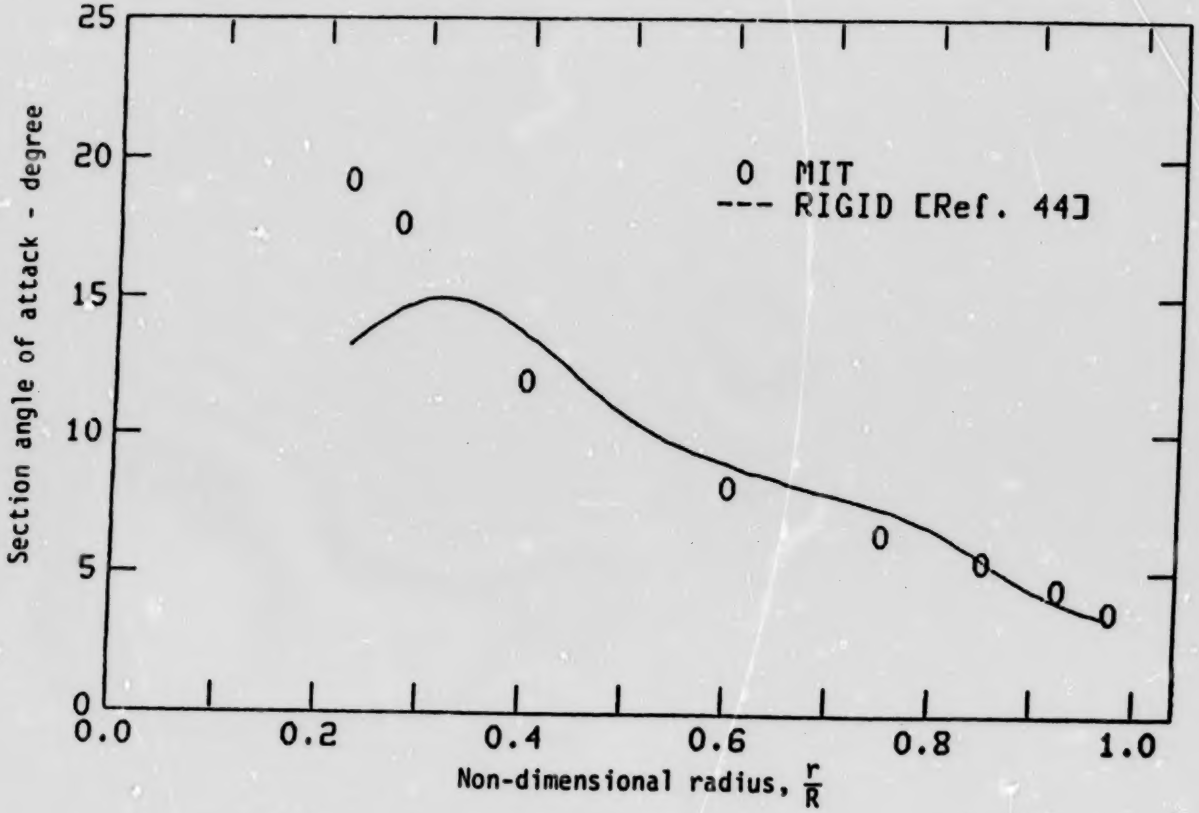

Fig. 6-46 Comparison of rigid wake effective angle of attack distribution along the blade with existing MIT [7] data (case 2).

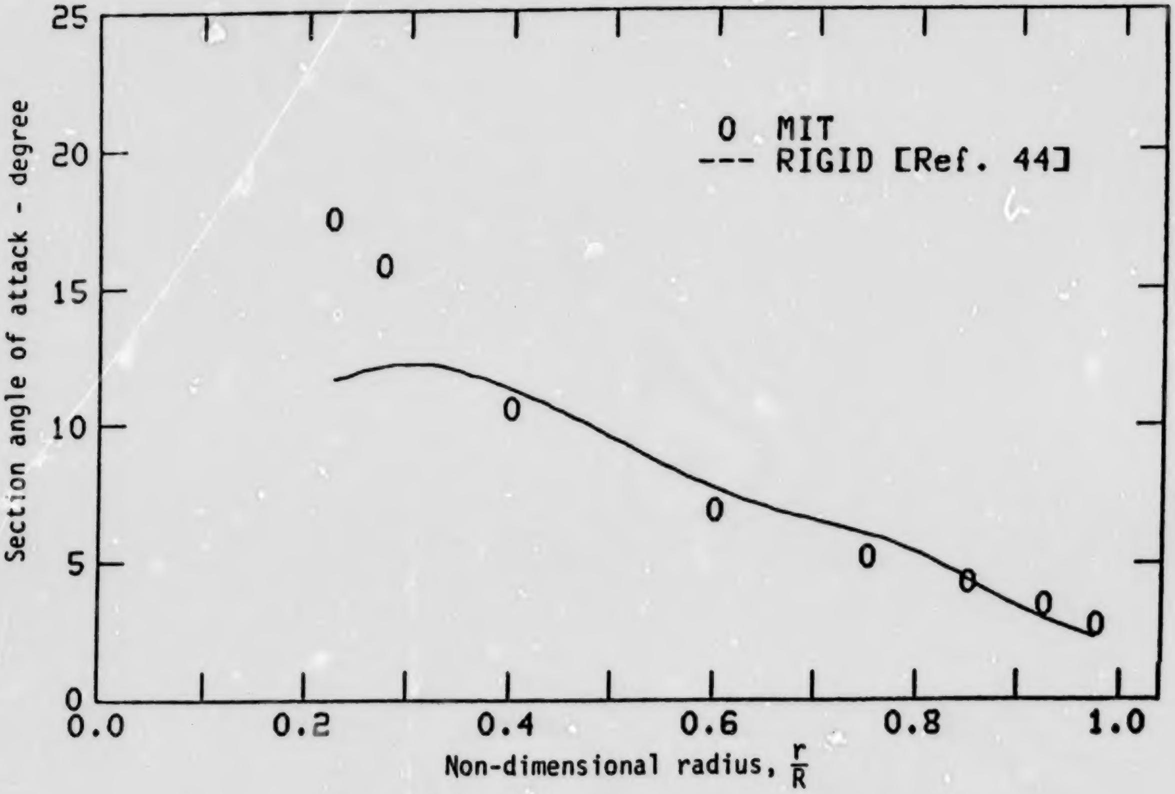

Fig. 6-47 Comparison of rigid wake effective angle of attack distribution along the blade with existing MIT [7] data (case 3).

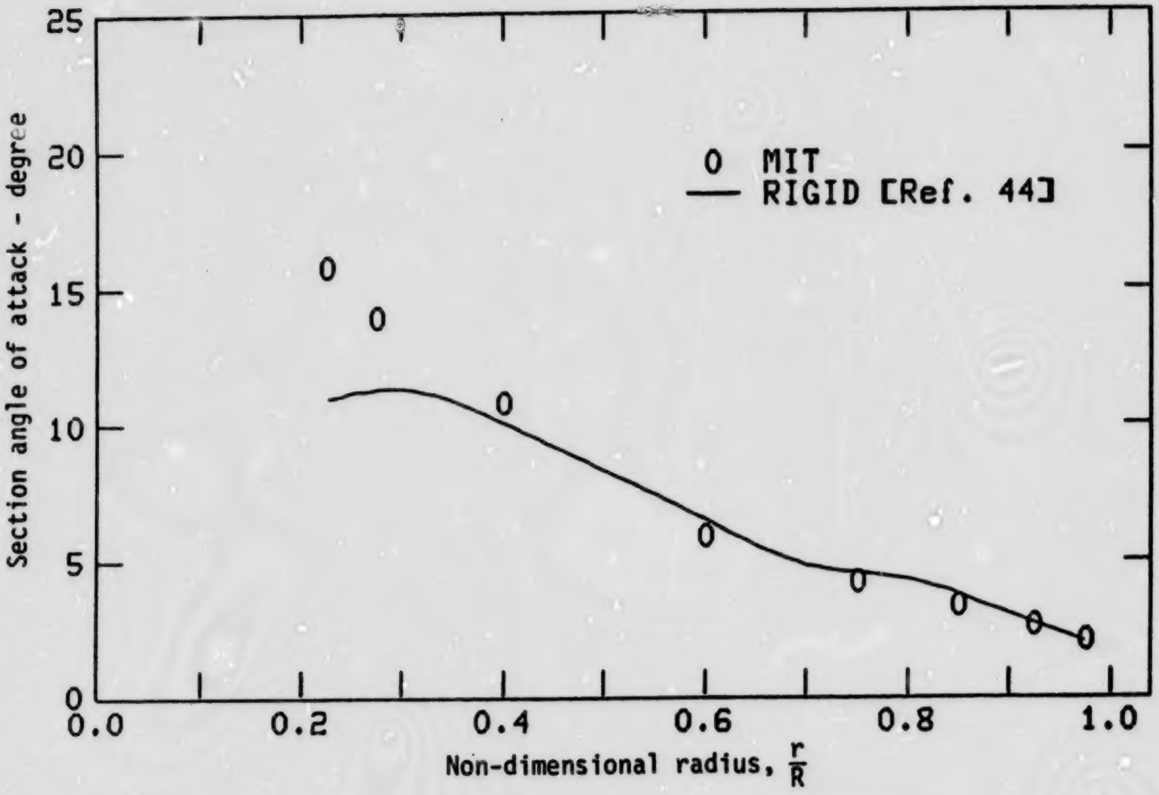

Fig. 6-48 Comparison of rigid wake effective angle of attack distribution along the blade with existing MIT [7] data (case 4).

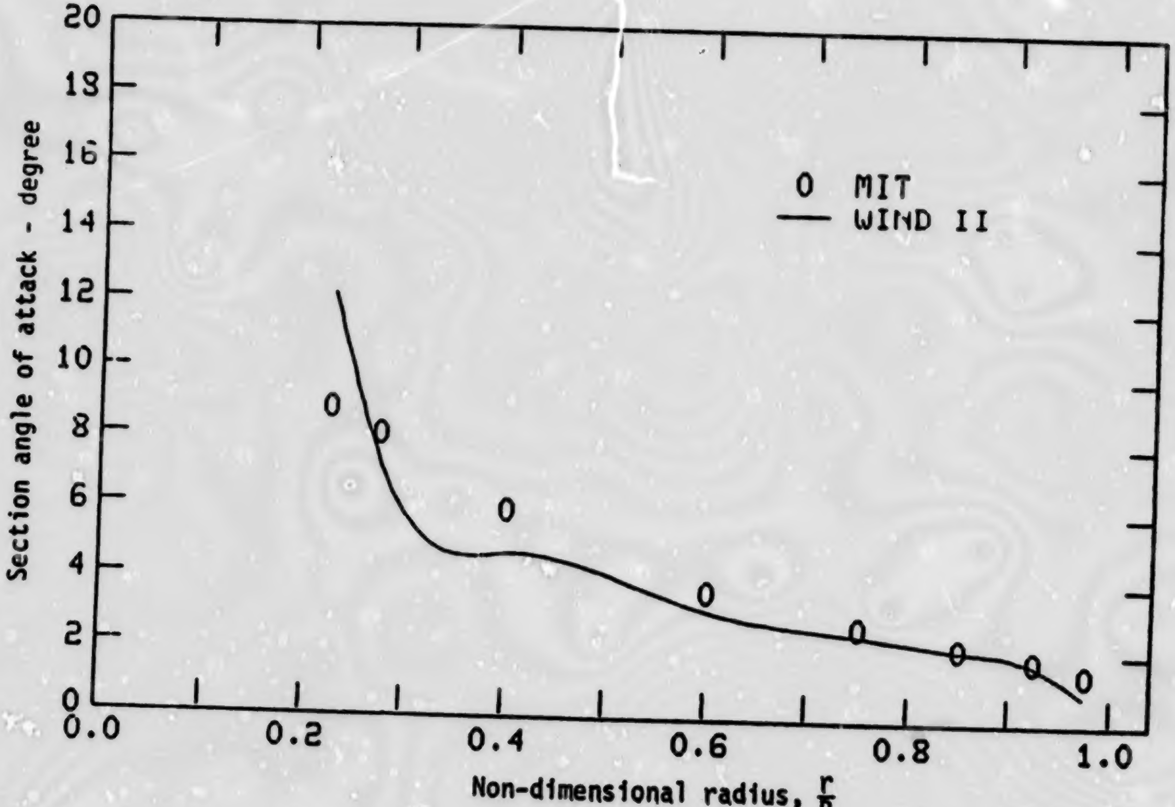

Fig. 6-49 Comparison of WIND II [54] effectice angle of attack distribution along the blade with existing MIT [7] data (case 1).

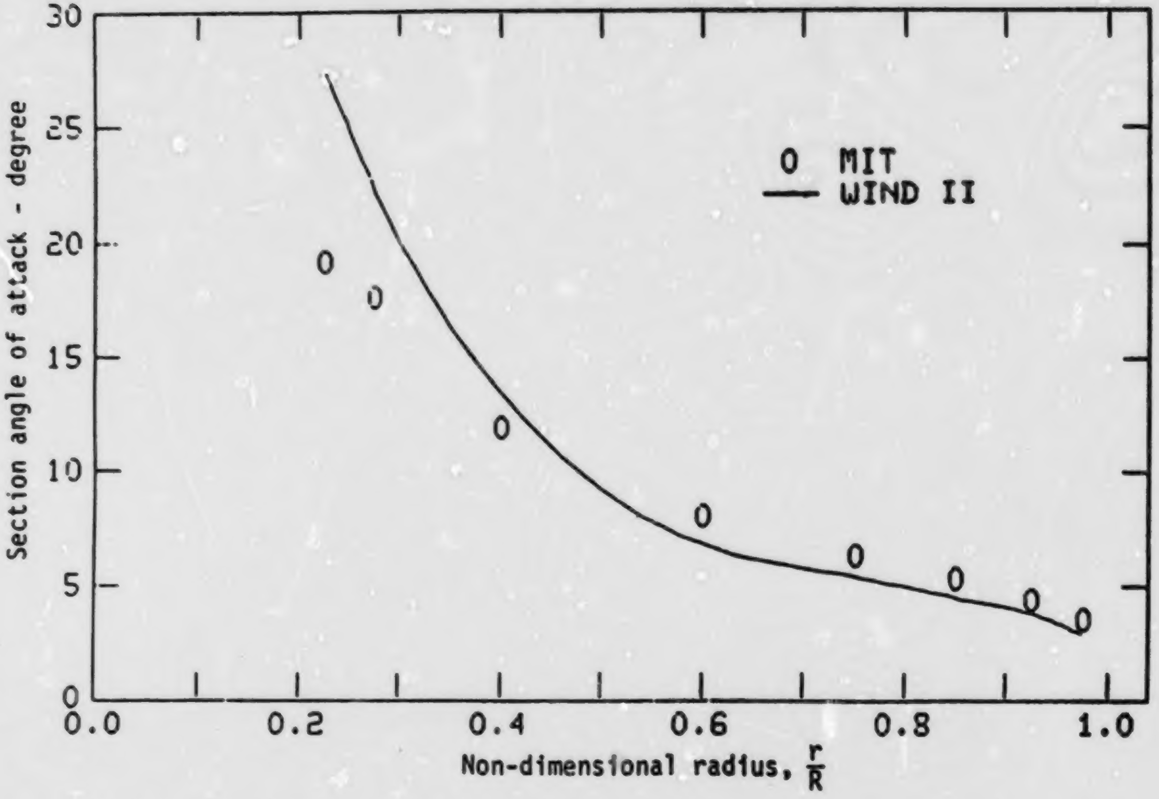

Fig. 6-50 Comparison of WIND II [54] effective angle of attack distribution along the blade with existing MIT [7] data (case 2).

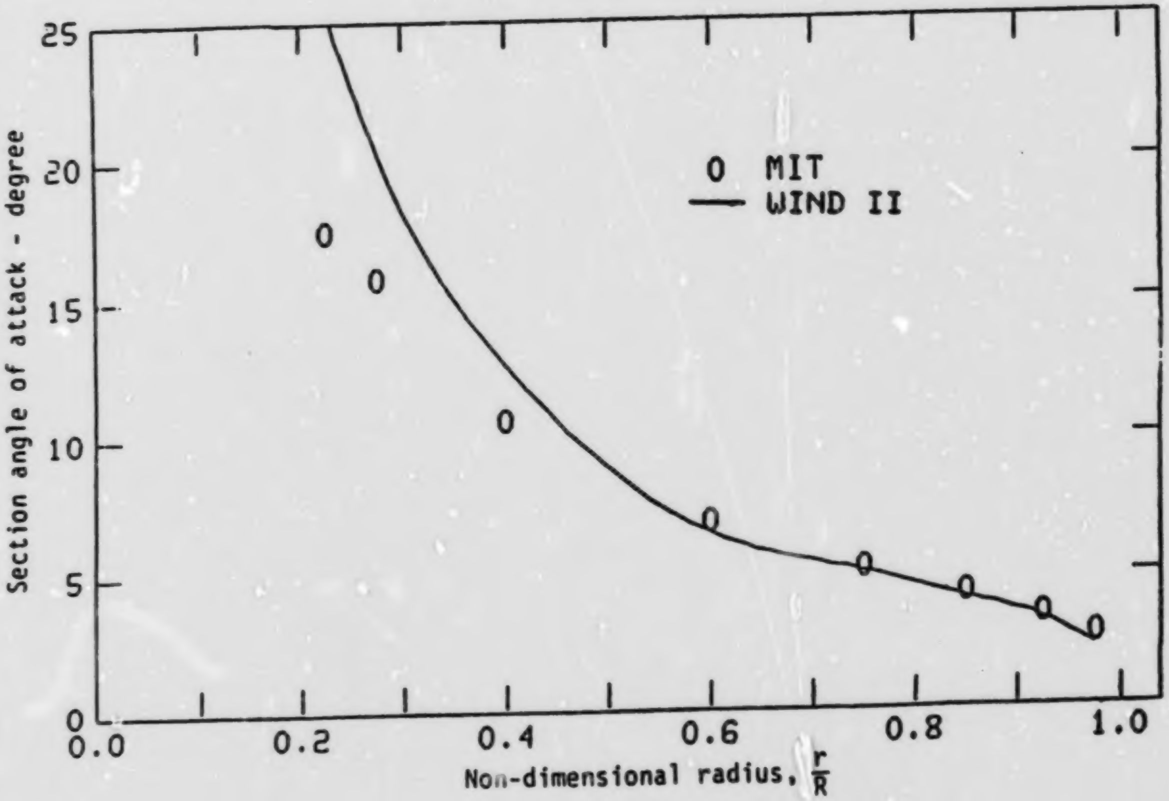

Fig. 6-51 Comparison of WIND II [54] effective angle of attack distribution along the blade with existing MIT [7] data (case 3).

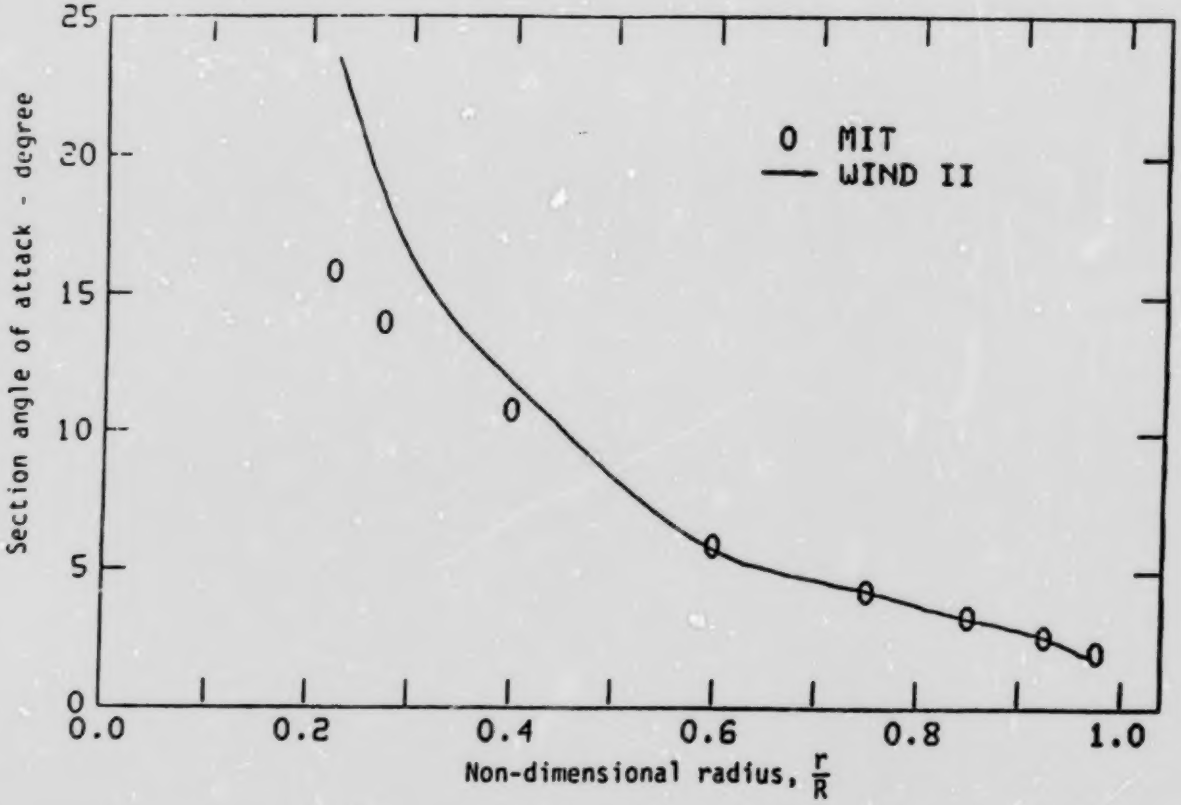

Fig. 6-52 Comparison of WIND II [54] effective angle of attack distribution along the blade with existing MIT [7] data (case 4).

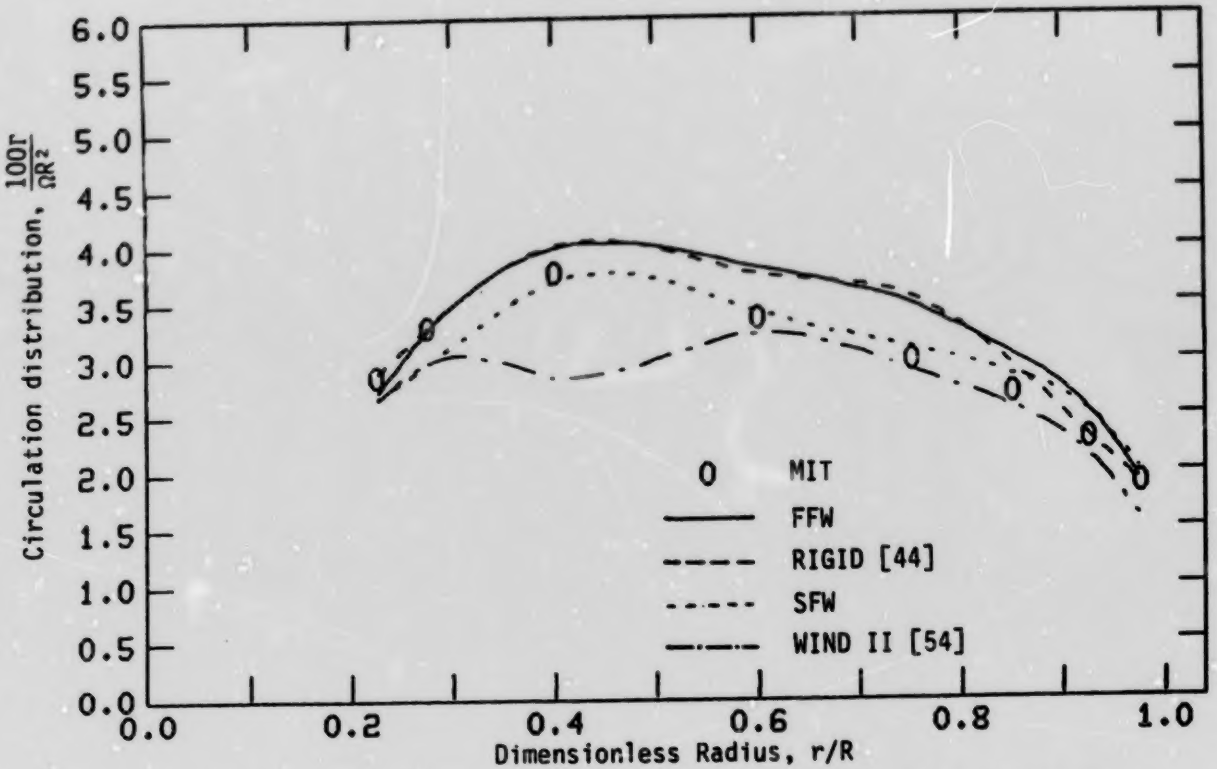

Fig. 6-53 Comparison of dimensionless circulation distribution along the blade for different flow models (case 4).

Table 6-6 Comparison of Power Coefficients and Axial Force (thrust) Coefficients

CASE	MIT	FFW	SFW	Rigid	PROP
	$C_P = \frac{P}{1/2\ \rho\pi R^2 V_o{}^3}$				
1	0.3392	0.398	0.417	0.584	0.230
2	0.4575	0.4614	0.454	0.486	0.315
3	0.4609	0.502	0.473	0.472	0.381
4	0.4379	0.529	0.451	0.440	0.393
	$C_F = \frac{F}{1/2\ \rho\pi R^2 Vo^2}$				
1	1.062	1.121	1.144	1.235	0.8795
2	1.1145	1.115	1.103	1.054	0.8733
3	0.9527	0.993	0.959	0.909	0.8079
4	0.7964	0.881	0.803	0.766	0.7078

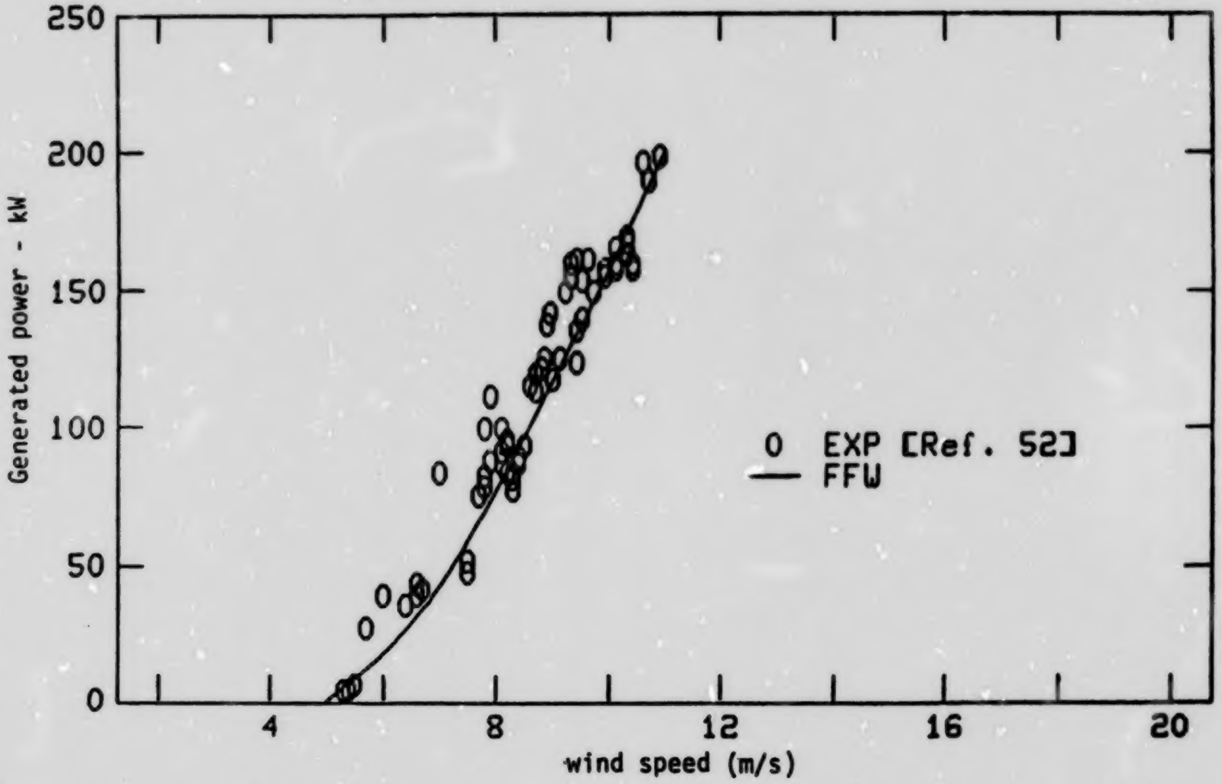

Fig. 6-54 Comparison of experimental generated-power vs. wind speed with fast free wake method (case 5).

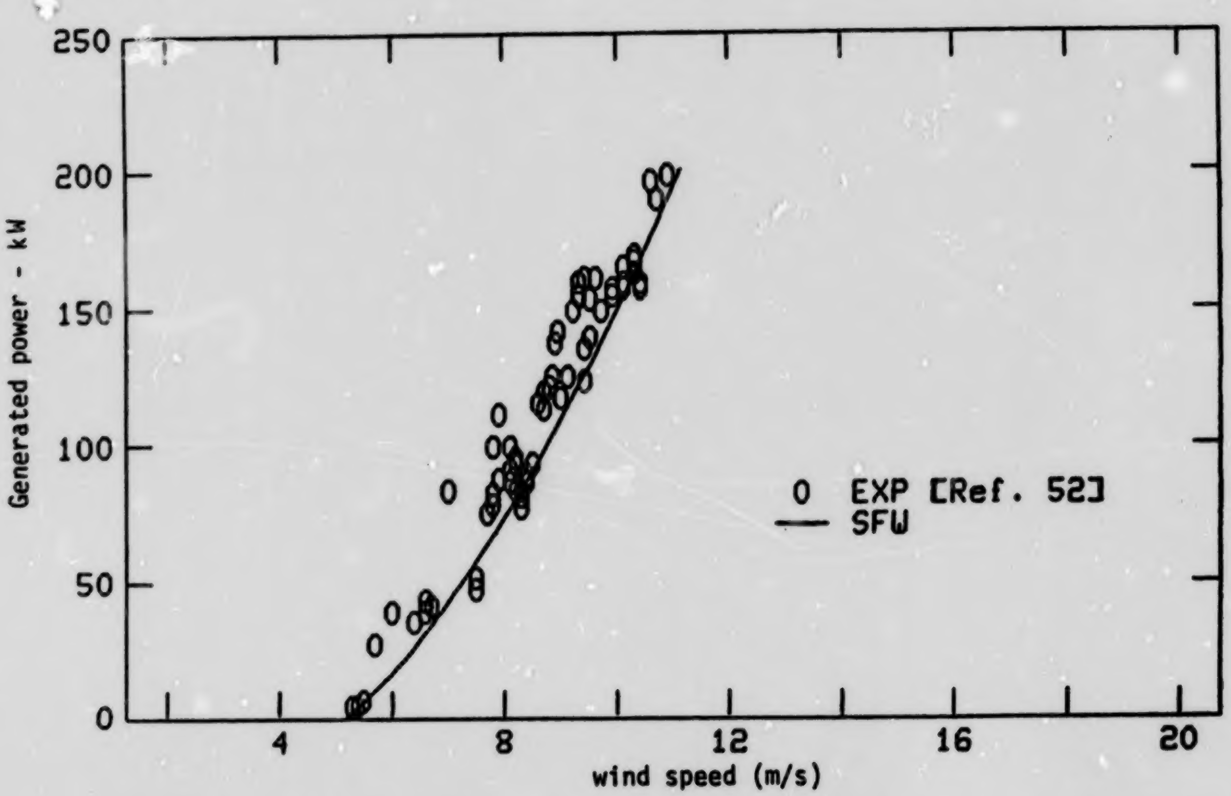

Fig. 6-55 Comparison of experimental generated-power vs. wind speed with simplified free wake method (case 5).

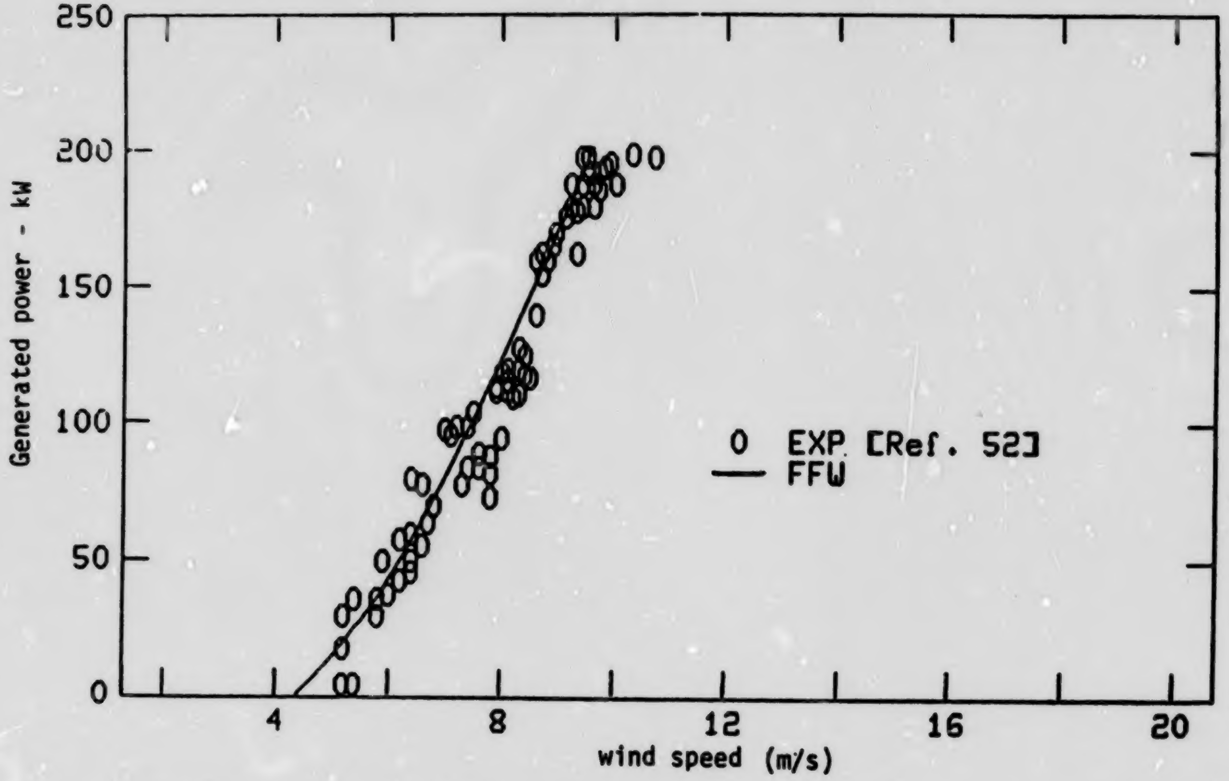

Fig. 6-56 Comparison of experimental generated-power vs. wind speed with fast free wake method (case 6).

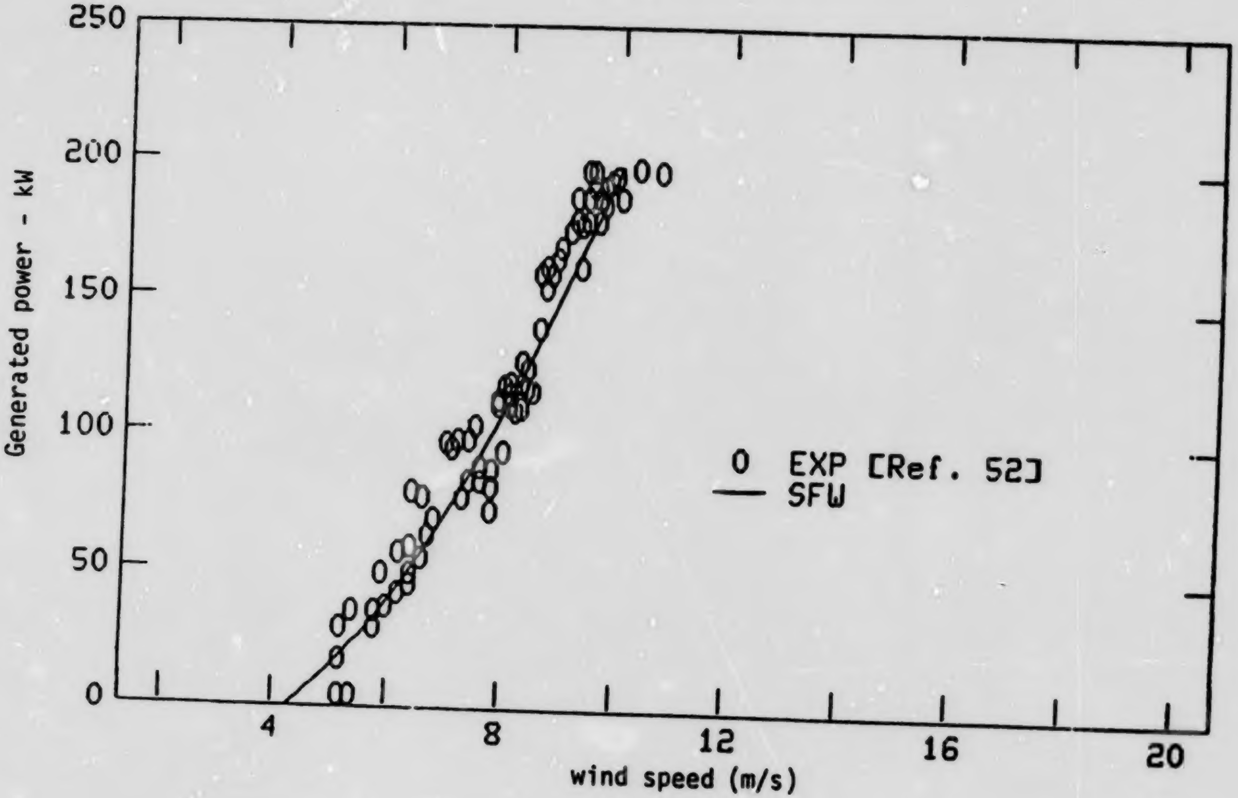

Fig. 6-57 Comparison of experimental generated-power vs. wind speed with simplified free wake method (case 6).

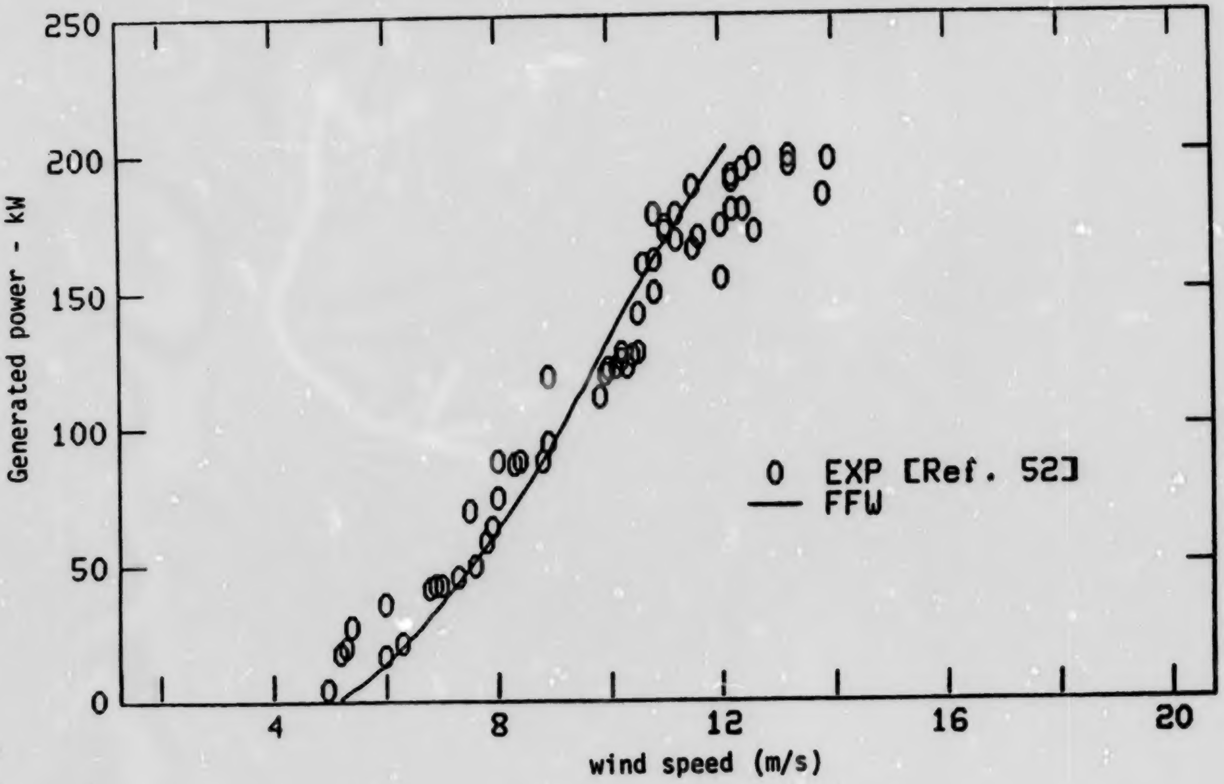

Fig. 6-58 Comparison of experimental generated-power vs. wind speed with fast free wake method (case 7).

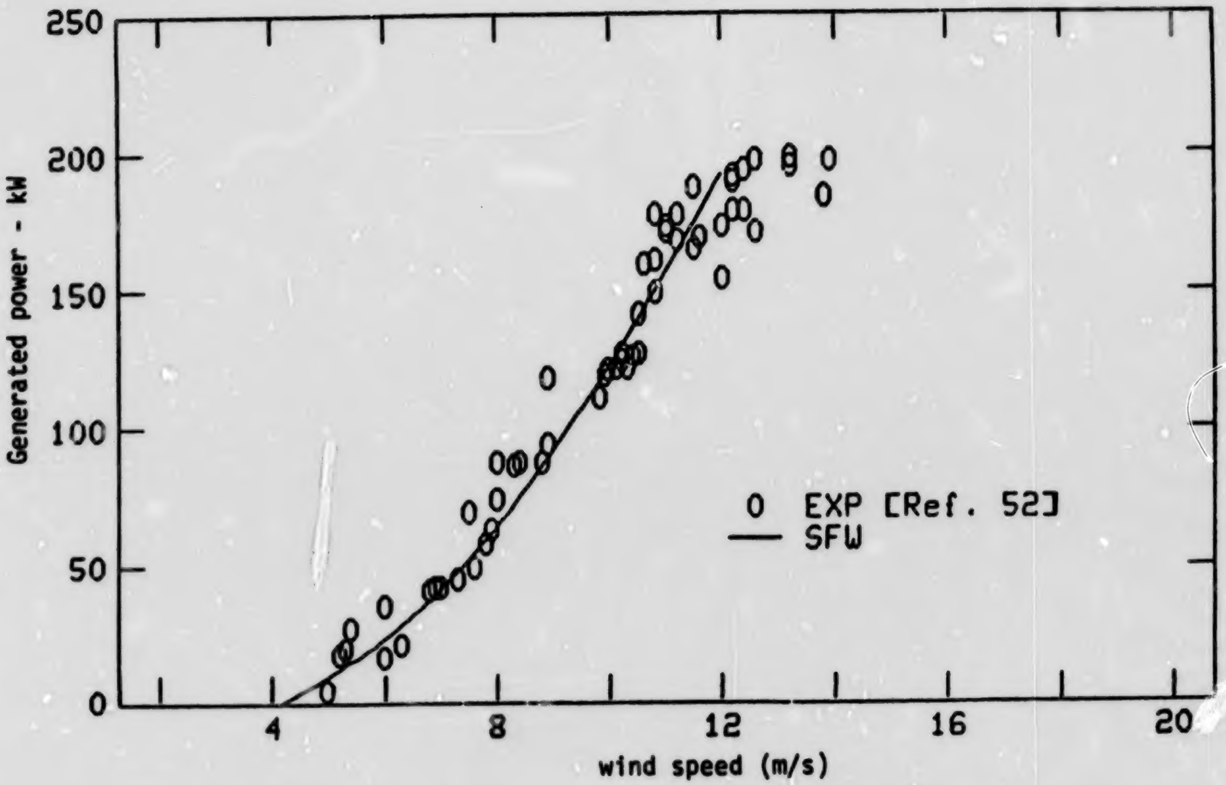

Fig. 6-59 Comparison of experimental generated-power vs. wind speed with simplified free wake method (case 7).

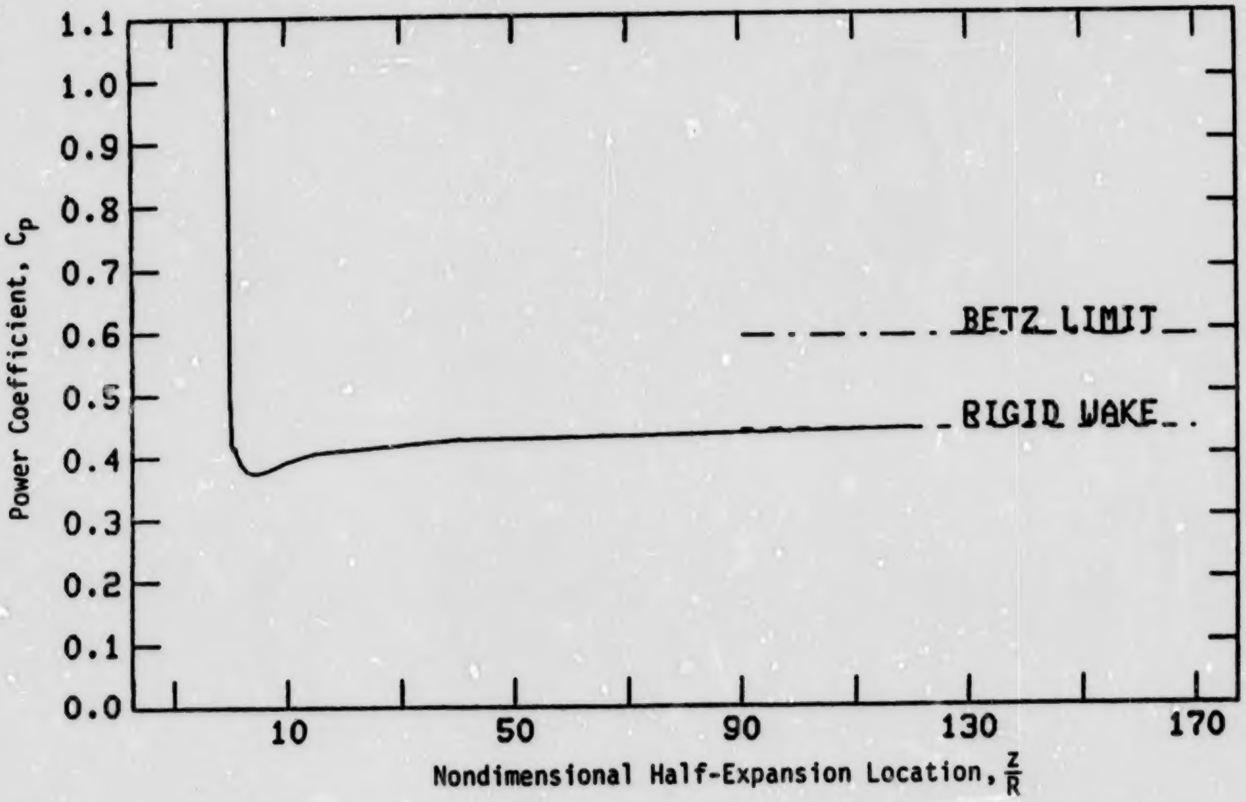

Fig. 6-60 Plot of power coefficient vs. half-expansion location

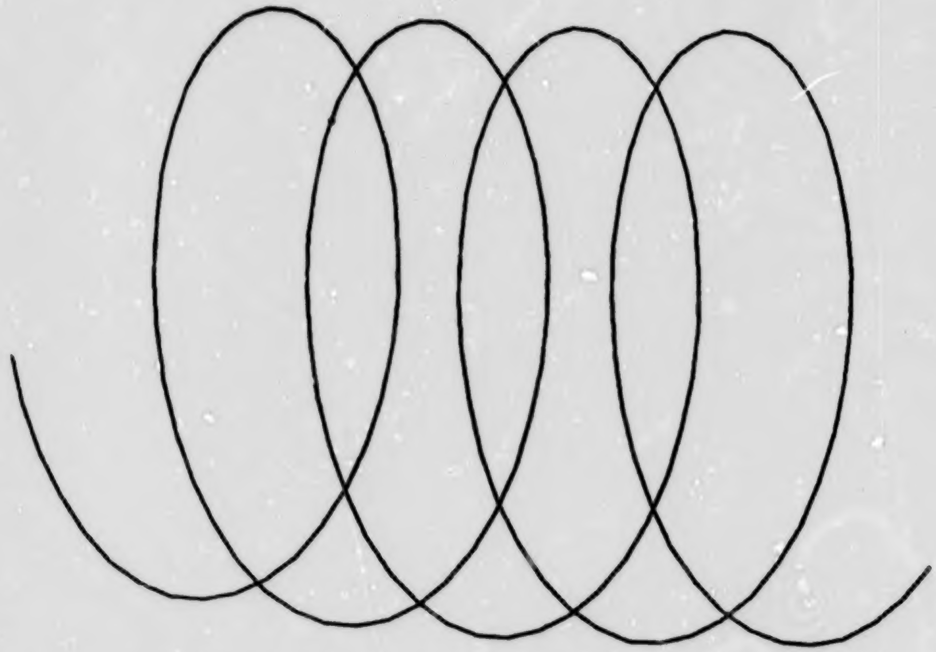

Fig. 6-61 Plot of computed tip vortex geometry (case 4).

Chapter VII

CONCLUSIONS AND RECOMMENDATIONS

In this thesis, two numerical methods of performance prediction of a horizontal axis wind turbine have been developed and successfully applied. In addition, a computer code based on the prescribed wake theory of rotary wings has been developed. Due to the lack of experimental data on the wake of wind turbines, however, the results of this method have only a qualitative value at the present time. The computational codes developed and results presented are for two-bladed rotors. Slight modifications to the existing codes would be required to model wind turbines of more than two blades. The principal limitations on the precision of the methods presented is the restriction on accurate airfoil data and the specified wake geometry model. The assumptions made in the theoretical models are that the fluid is ideal (incompressible and inviscid) and that no separation takes place. Some approximate techniques are required for numerical, computer solution of such complicated problems; however, in principle these approximations can be progressively refined to obtain any degree of accuracy desired.

The basic solutions consist of the definition of wake geometry that can be used to obtain the velocity at any point in the field of a wind turbine using potential flow theory. Application of the Kutta-Joukowski theorem, the Prandtl hypothesis and airfoil data yields a set of coupled nonlinear equations. Algorithms were constructed for the specific application of the methods of analysis to a two-bladed horizontal axis wind turbine. Blade configurations ranged from a simple constant chord, no twist planform to a tapered blade with a variable twist distribution. The wake geometry was approximated by filaments having concentrated vorticity. Each filament consists of a series of segmented straight vortex lines. The wake elements were unconstrained, that is, they are allowed to move with the local velocity field.

Concerning the application of the FFW (fast free wake) method to wind turbines the following conclusions are offered:

1. Successful prediction of wind turbine performance and loading is possible with relatively few vortex rings in the intermediate wake.
2. Accurate prediction of induced velocity at the blade root section requires more vortex rings in the intermediate wake. However, the overall distributions of induced velocity and effective angle of attack along the blade appears reasonably satisfactory.

On the basis of the induced velocity and circulation distribution computations made using SFW (simplified free wake) model for a number of rotor configurations, the following conclusions are presented:

3. A rapidly converging iterative scheme using a lifting line theory can be used to predict the velocity field and loading

parameters of a horizontal axis wind turbine with confidence.

4. For a two-bladed turbine the lifting line representation for the blade appears to be adequate as shown by the present method results. However, detailed experimental data on blade loads and the velocity field should further be utilized for verification purposes.
5. Modeling of the distorted rotor wake was partially successful. While the overall blade performance parameters were properly predicted, the circulation distribution outboard of the maximum circulation station was slightly overpredicted.
6. For overall performance, the presence of the inboard far wake had very little effect on the airloads and a negligible effect on the computed wake geometry.

In addition to conclusions 1 to 6 concerning the airloads and induced velocity distributions, the following conclusions for the power prediction problem are stated:

7. Comparison with experimental data indicated very good agreement at low and rated power. The differences were within the range of experimental error.
8. Airfoil data critically influences the results of this analysis.

Based on the comparisons of the results of the blade element-momentum theory with those of methods developed herein, the following conclusion is made:

9. The momentum-blade element theory can be used to calculate integrated quantities such as power coefficient and torque but

it is essential to use more refined theories to predict quantities such as velocity and circulation distributions on the blade surface.

Regarding the parametric study performed using the prescribed wake code, the following conclusion is drawn:

10. The wake expansion has a positive effect on the performance of a horizontal axis wind turbine. Hence, when expansion effects are not negligible (cases of low wind speed condition), an analysis based on a rigid wake model could underpredict the performance.

It is recommended that a computer code be developed to predict the circulation and velocity distributions on wind turbine rotors with the following modifications made to the method presented here:

1. Use a number of different mathematical models of the tip vortex formation configurations in order to obtain a better understanding of the actual tip vortex formation.
2. Corrections for Reynolds number effect be made not by modifying the airfoil data, but rather by use of an average boundary layer displacement thickness. It is anticipated that this would improve the results of the analysis.

Further, it is recommended that an experimental investigation be carried out with the following objectives:

3. To define the geometry of the wake very close to the blade, for various blade configurations and pitch angles.
4. To measure the pressure distribution along the blade for various operating conditions and blade geometries.
5. To measure the strength of the tip vortex as it forms and as it moves downstream of the rotor in the very near wake.

REFERENCES

1. Devries, O., "On the Theory of Horizontal-Axis Wind Turbines", Annual Review of Fluid Mechanics, Vol. 15, 1983, pp. 77-96.

2. Gray, R. B., "On the Motion of the Helical Vortex Shed from a Single-Bladed Hovering Model Helicopter Rotor and its Application to the Calculation of Spanwise Aerodynamic Loading", Princeton University, Aero. Engr. Dept., Report No. 313, 1955.

3. Gray, R. B., "An Aerodynamic Analysis of a Single-Bladed Rotor in Hover and in Low-Speed Forward Flight as Determined from Smoke Studies of the Vorticity Distribution in the Wake", Princeton University, Aero. Engr. Dept., Report No. 356, 1956.

4. Landgrebe, A. J., "An Analytical and Experimental Investigation of Helicopter Rotor Hover Performance and Wake Geometry Characteristics", USAAMRDL Tech. Report 71-24, US Army Air Mobility Research and Development Lab., Fort Eustis, June 1971.

5. Landgrebe, A. J., "An Analytical Method of Predicting Rotor Wake Geometry", J. of American Helicopter Society, Vol. 14, No. 4, 1969.

6. Gray, R. B., and Brown, G. W., "A Vortex Wake Analysis of a Single-Bladed Hovering Rotor and a Comparison with Experimental Data:, AGARD Conference Pre-print 111 on Aerodynamics of Rotary Wings, Marseilles, France, September 1972.

7. Gohard, J. C., "Free Wake Analysis of Wing Turbine Aerodynamics", ASRL TR-184-14, Aero. and Struc. Research Lab., Dept. of Aeronautics and Astronautics, MIT, September 1978.

8. Cheney, M. C., and Landgrebe, A. J., "Rotor Wakes: Key to Performance Prediction", AGARD Conference Pre-print 111 on Aerodynamics of Rotoray Wings, Marseilles, France, September 1972.

9. Savino, J. M. and Nyland, T. W., "Wind Turbine Flow Visualization Studies: Tip and Root Vortices and Wind Stream Pattern at Low Power", PIR No. 241, Wind Energy Project Office NASA Lewis Research Center, November 30, 1983.

10. Cermak, J. E. "Applications of Fluid Mechanics to Wind Engineering-A Freeman Scholar Lecture", Journal of Fluids Engineering, March 1975.

11. Miller, R. H., "Rotor Blade Harmonic Air Loading", Journal of Royal Aeronautical Society, Vol. 68, No. 640, April 1964, pp. 217-229.

12. Miller, R. H., "Rotor Hovering Performance Using the Method of Fast Free Wake Analysis", Journal of Aircraft, Vol. 20, No. 3, March 1982, pp. 257-261. Also MIT Aeroelastic and Structure Research Laboratory, Cambridge, Massachusetts, TR 194-3, Aug. 1981.

13. Rankine, W. J. M., "On the Mechanical Principle of the Action of Propellers", Transactions of the Institute of Naval Architects, Vol. 6, 1865.

14. Froude, W., "On the Elementary Relation Between Pitch, Slip and Propulsive Efficiency", Transactions of the Institute of Naval Architects, Vol. 19, 1978.

15. Durand, W. F., Editor-in-chief, "Aerodynamic Theory", Vol. IV, Dover Press Inc., 1963.

16. Wilson, R. E. and Walker, S. N. "A Fortran Program for the Determination of Performance, Load and Stability Derivatives of Windmills," Dept. of Mechanical Engineering, Oregon State University. (RANN), Under Grant No. GI-41840, October 25, 1974.

17. Wentz, W. H., and Calhoun, J. T., "Analytical Studies of New Airfoils for Wind Turbines", NASA CP-2185, February 1981.

18. Milne-Thomson, W., "Theoretical Hydrodynamics", McMillan Publishing Company, 1956.

19. Batchelor, G. K., "An Introduction to Fluid Dynamics", Cambridge University Press, 1967.

20. Glauert, H., "The Elements of Airfoil and Airscrew Theory", University Press, Cambridge, 1948.

21. Prandtl, L., "Application of Modern Hydrodynamics to Aeronautics", NACA Report 116, 1921.

22. Goldstein, S., "On the Vortex Theory of Screw Propellers", Proceedings of the Royal Society of London, Series A, Vol. 123, 1923.

23. Betz, A., "Screw Propellers with Minimum Loss of Energy", Nachrichten der K. Gesellschaft der Wissenschaften Zu Gottingen, 1919.

24. McCormick, B. W., Eisenhuth, J. J., Lynn, J. E., "A Study of Torpedo Propellers - Part I", Ordinance Research Laboratory, Serial No. NORD 16597-5, March 1956.

25. Lock, C. N., "Application of Goldstein Theory to the Practical Design of Airscrews", Aeronautical Research Council, R & M No. 1377, November 1930.

26. Jenny, D. S., Olson, J. R., and Landgrebe, A. J., "A Reassessment of Rotor Hovering Performance Prediction Methods", Journal of American Helicopter Society, Vol. 13, No. 2, April 1968.

27. Tanner, W. A., and Wohlfeld, R. M., "Vortex Field, Tip Vortex, and Shock Formation of a Model Propeller", Proceedings Third CAL/AVLABS Symposium, Aerodynamics of Rotary Wing and V/STOL Aircracft, Vol. 1, Rotor/Propeller Aerodynamics Rotor Noise, June 18-20, 1969.

28. Crimi, P., "Prediction of Rotor Wake Flows", CAL/USAAVLABS Symposium Proceedings, Vol. 1, June 1966.

29. Brady, W. G., and Crimi, P., "Representation of Propeller Wakes by Systems of Finite Core Vortices", Cornell-Aeronautical Lab. Report No. BB-1655-5-2, February 1965.

30. Trenka, A. R., "Development of a Method for Predicting the Performance and Stresses of VTOL-Type Propellers", USAAVLABS TR66-26, June 1966.

31. Theodorson, T., "Theory of Propellers", McGraw Hill, 1948.

32. Sadler, S. G., "A Method for Predicting Helicopter Wake Geometry, Wake-Induced Flow and Wake Effects on Blade Airloads", Presented at the 27th Annual National V/STOL Forum of the American Helicopter Society, May 1972.

33. Spreiter, J. R. and Sacks, A. H., "The Rolling Up of the Trailing Vortex Sheet and Its Effect on the Downwash Behind Wings", Journal of Aeronautical Sciences, Vol. 18, No. 1, January 1951.

34. Betz, A., "Behavior of Vortex Systems", Zeit fur angewandte Math. and Mech., Vol. 12, No. 3, June 1932. Also NACA Tech. Memo. 713, June 1933.

35. Brown, C. E., "Aerodynamic of Wake Vortices", AIAA Journal, Vol. 11, No. 4, April 1973, pp. 531-536.

36. Donaldson, C., Snedeker, R. S. and Sullivan, R. D, "A Method of Calculating Aircraft Wake Velocity Profiles and Comparison with Full-Schale Experimental Measurements", AIAA Paper No. 74-39, 1974.

37. Kaden, H., "Aufwicklung einer Unstabilen Unstetig Keitsflache," Ing. Arch. 2, 1931.

38. Westwater, F. L., "The Rolling-Up of the Surface of Discontinuity Behind an Aerofoil of Finite Span", ARC R & M No. 1962, August 1933.

39. Rosenhead, L., "The Formation of Vortices from a Surface of Discontinuity", Proceedings of Royal Society of London, Series A, Vol. 134, 1931.

40. Takami, H., "A Numerical Experiment with Discrete Vortex Approximation with Reference to the Rolling-Up of a Vortex Sheet", SUDAAR No. 202, Stanford University, 1864.

41. Jordan, P. F., "Span Loading and Formation of the Wake", AFOSR TR 70-2873, Presented at AFSOR-Boeing Symposium on Aircraft Wake Turbulence, September 1970.

42. El-Ramly, Z., "Aircraft Trailing Vortices: A Survey of the Problem", Report No. ME/A72-1, Carlton University, Ottawa, Canada, November 1972.

43. Moriya, T. "Selected Scientific and Technical Papers", University of Tokyo, 1959.

44. Jeng, D. R., Keith, T. G., Aliakbarkhanafjeh, A., "Aerodynamic Analysis of a Horizontal-Axis Wind Turbine by Use of Helical Vortex Theory, Volume I: Theory", NASA CR-168054, December 1982.

45. McCormick, B. W., "Aerodynamics of V/STOL Flight", Academic Press New York, 1967.

46. Abbott, H. and VonDoenhoff, A. E., Theory of Wing Sections, McGraw-Hill, 1949.

47. Sheldehl, R. E. and Klimas, P. C., "Aerodynamic Characteristics of Seven Symmetrical Airfoil Sections Through 180-degree Angle of Attack for Use in Aerodynamic Analysis of Vertical Axis Wind Turbines", Design Technology Seminar for Industry, Sandia National Laboratories Report SAND 80-0984, August 1980.

48. Donaldson, C., dup. and Bilanin, A. J. "Vortex Wakes of Conventional Aircraft," AGARDograph No. 204, May 1975.

49. Batchelor, G. K., "Axial Flow in Trailing Line Vortices," Journal of Fluid Mechanics, Vol. 20, 1964, pp. 645-655.

50. Hama, F. R. and Nutant, J., "Self-Induced Velocity on a Curved Vortex", Physics of Fluids, Vol. 4, No. 1, January 1961, pp. 28-32.

51. Hama, F. R., "Progressive Deformation of a Curved Vortex by Its Own Induction", Physics of Fluids, Vol. 5, No. 10, October 1962, pp. 1156-1162.

52. Arms, R. J. and Hama, F. R., "Localized Induction Concept on a Curved Vortex and Motion of an Elliptic Vortex Ring", Physics of Fluids, Vol. 8, No. 4, April 1965, pp. 553-559.

52. Spera, D. A. and Janetzke, D. C. "Performance and Load Data from Mod-OA and Mod-1 Wind Turbines", Proceedings of a Workshop on Large Horizontal-Axis Wind Turbines, July 28-30, 1981, pp. 447-468, NASA Conference Publication 2230 or DOE Publication CONF-810752, 1981.

53. Samat, S. S., "An Improved Method of Calculating the Tip Vortex Geometry For Hovering Rotors," Ph.D. Thesis, School of Aerospace Engineering, Georgia Insitute of Technology, 1976.

54. Snyder, M. H. and Staples, D. L., "Wind II Users Manual", Wind Energy Lab, Wichita State University Report, WER-15, July 1982.

*U.S. GOVERNMENT PRINTING OFFICE:1985/559-109/10441

1. Report No.
NASA CR-174920

2. Government Accession No.

3. Recipient's Catalog No.

4. Title and Subtitle
Wake Effects on the Aerodynamic Performance of Horizontal Axis Wind Turbines

5. Report Date
August 1984

6. Performing Organization Code

7. Author(s)
Abdollah Afjeh

8. Performing Organization Report No.
776-33-41

10. Work Unit No.

9. Performing Organization Name and Address
The University of Toledo
Toledo, Ohio

11. Contract or Grant No.
NCC 3-5

13. Type of Report and Period Covered
Contractor Report

12. Sponsoring Agency Name and Address
National Aeronautics and Space Administration
Washington, D.C. 20546

14. Sponsoring Agency ~~Code~~ Report No.
DOE/NASA/0005-1

15. Supplementary Notes
Final report. Prepared under Interagency Agreement DE-AI01-76ET20320. Project Manager, Robert Corrigan, Wind Energy Project Office, NASA Lewis Research Center, Cleveland, Ohio 44135.

16. Abstract
Success of vortex theories in the performance analysis of horizontal axis wind turbines depends greatly upon accurate specification of the geometry of the vortex wake. In this study, two methods of analysis are developed: a new simplified free wake method (SFW) and a prescribed wake method. In addition, an earlier wake model of helicopter rotors is extended for wind turbine applications. This method is referred to as the fast free wake method (FFW). The FFW was accomplished by partitioning the flow field downstream of the rotor into three regions: the near wake, modeled as a series of straight vortex lines; the intermediate wake, modeled as a number of vortex rings; and the far wake, taken to be a semi-infinite cylindrical wake. In the SFW, a new wake model is proposed. The model assumes that the wake is composed of an intense tip vortex and a diffused inboard wake, consistent with the experimentally observed wake of hovering helicopters. However, due to the complexity of the tip vortex formation and due to the lack of such experimental data for wind turbines, it was assumed that the vortex formation was almost immediate as opposed to the actual gradual rolling-up of the tip vortex. For the prescribed wake analysis the expansion of the wake must be known. Unfortunately, detailed wake measurements for wind turbines are sparse in number; hence, the method was demonstrated by assuming the wake expansion could be represented by an analytical expression.

17. Key Words (Suggested by Author(s))
Horizontal axis wind turbine
Wake effects

18. Distribution Statement
Unclassified - unlimited
STAR Category 44
DOE Category UC-60

19. Security Classif. (of this report)	20. Security Classif. (of this page)	21. No. of pages	22. Price*
Unclassified	Unclassified	176	A09

*For sale by the National Technical Information Service, Springfield, Virginia 22161